Searching for Hidden Sector Dark Matter with Fixed Target Neutrino Experiments

by

Patrick deNiverville
B.Sc., Mount Allison University, 2009
M.Sc., University of Victoria, 2011

A Dissertation Submitted in Partial Fulfillment of the
Requirements for the Degree of

DOCTOR OF PHILOSOPHY

in the Department of Physics and Astronomy

Searching for Hidden Sector Dark Matter with Fixed Target Neutrino Experiments

by

Patrick deNiverville
B.Sc., Mount Allison University, 2009
M.Sc., University of Victoria, 2011

Supervisory Committee

Dr. Adam Ritz, Supervisor
(Department of Physics and Astronomy)

Dr. Maxim Pospelov, Departmental Member
(Department of Physics and Astronomy)

Dr. Pavel Kovtun, Departmental Member
(Department of Physics and Astronomy)

Dr. Poman So, Outside Member
(Department of Electrical & Computer Engineering)

ABSTRACT

We study the sensitivity of fixed target neutrino experiments (LSND, T2K, CENNS, and COHERENT) and proton beam dumps (MiniBooNE off-target, and SHiP) to sub-GeV dark matter. In order to reproduce the observed thermal relic abundance, these states are coupled to the Standard Model via new, low mass mediators in the form of a kinetically mixed U(1)$'$ vector mediator or a vector mediator gauging baryon number. We present a model for the production of low mass dark matter from proton-nucleon collisions in fixed targets. Sensitivity projections are made using signals from elastic electron- and nucleon-dark matter scattering, as well as coherent nuclear-dark matter scattering and dark matter induced inelastic π^0 production. A fixed target Monte Carlo code has been developed for this analysis, and documentation is included. We find that analyses using current and future proton fixed target experiments are capable of placing new limits on the hidden sector dark matter parameter space for dark matter masses of up to 500 MeV and mediator masses as large as a few GeV.

Contents

List of Tables

List of Figures

LIST OF ABBREVIATIONS

BBN Big Bang Nucleosynthesis

BMPT Bonesini, Marchionni, Pietropaolo and Tabarelli de Fatis

BSM Beyond the Standard Model

CEvNS Coherent Elastic Neutrino-Nucleus Scattering

CMB Cosmic Microwave Background

DM Dark Matter

eV electron Volt

IR Infrared

LSND Liquid Scintillator Neutrino Detector

MiniBooNE Mini Booster Neutrino Experiment

MOND Modified Newtonian Gravity

NCE Neutral Current Elastic

NP New Physics

PDF Parton Distribution Function

POT Protons On Target

QCD Quantum Chromodynamics

SD Spin-Dependent

SHiP Search for Hidden Particles

SI Spin-Independent

SM Standard Model

SNS Spallation Neutrino Source

T2K Tokai to Kamioka

UV Ultraviolet

WIMP Weakly Interacting Massive Particle

ACKNOWLEDGEMENTS

I would like to thank:

My Parents, Bill and Germaine deNiverville, for their constant support.

My supervisor, Adam Ritz, for his encouragement, direction and advice.

The MiniBooNE collaboration, for inviting me to join their experimental collaboration to assist with the off-target run. It has made for a unique graduate experience.

Chapter 1

Introduction

There exists overwhelming astrophysical and cosmological evidence for the presence of some abundant yet unseen source of mass in the universe. Observations have made it clear that this is not simply non-luminous baryonic matter[1] or a sea of the known neutrinos, but is instead an entirely different and undiscovered species of matter. We call these elusive particles **dark matter**, a catch-all term for a range of hypotheses that attempt to explain the nature of this unseen matter. While it may seem outrageous to postulate that the majority of the matter in the universe is made up of some invisible substance, the dark matter hypothesis provides an elegant explanation for numerous phenomena observed across a wide variety of length scales and different time periods in the evolution of the universe.

Thus far, all attempts to observe dark matter non-gravitationally, barring a number of intriguing but mostly contradictory anomalies, have failed to capture any sign of its particle nature. These searches embrace a plethora of different approaches, including direct searches using detectors buried deep beneath the Earth's surface, indirect searches with ground and satellite based telescopes hoping to catch a hint of dark matter decay or annihilation somewhere in the galaxy, and collider searches using the collision of high energy beams of particles at experimental facilities in hopes of creating dark matter in a controlled environment. The null results from particle searches have led to impressive limits on the dark matter parameter space that must be taken into account when formulating a dark matter theory.

[1] In this context baryonic matter refers to protons and neutrons, the particles which make up most of the Standard Model mass density of the universe. The electron, a non-baryonic Standard Model particle, is also extremely common, but its mass is approximately 2000 times smaller than that of the proton, significantly reducing its effect on the mass density of matter.

The Weakly Interacting Massive Particle (WIMP) provides a simple and effective scaffolding for the formulation of dark matter scenarios. While the WIMP framework allows for many scenarios, conventional WIMP masses range from several GeV to several TeV. We will focus on light dark matter with a sub-GeV mass. Our interest in this mass regime was originally motivated by the INTEGRAL 511 keV line, a narrow high-intensity signal of monochromatic photons from the center of the galaxy [23, 24]. The intensity of the signal pointed to the creation of enormous numbers of positrons in the center of the galaxy, which could have been produced by the annihilations of dark matter particles with masses of a few MeV. The presence of numerous recently discovered binary stars is a more likely explanation for the signal at present [25], but this has not diminished interest in sub-GeV dark matter, in part because their small mass provides a natural explanation for the null results of direct detection experiments.

Low mass dark matter introduces some complications in model building. This particle, were it to be produced as a thermal relic with annihilations proceeding through Standard Model states, would possess an annihilation cross section too small to generate a dark matter energy density compatible with that which is presently observed in the universe [26]. In order to bring the relic abundance of a weakly-interacting low mass dark matter scenario into agreement with empirical observations, new annihilation channels must be introduced. A convenient method of accomplishing this is to have the dark matter particles self-annihilate to Standard Model particles via new, low mass states belonging to a hidden sector, uncharged under the Standard Model gauge group [27, 28, 29, 30, 31, 32].

We will primarily be concerned with a scalar hidden sector dark matter candidate whose interactions with the Standard Model are mediated by a sub-GeV vector boson. Two versions of the scenario are considered, one in which the vector mediator kinetically mixes with the photon, and a second in which it couples to baryon number. The p-wave velocity-suppression of the annihilation cross section greatly weakens constraints on the candidate's mass from cosmological and astrophysical observations. As a member of a hidden sector, its coupling to Standard Model states can be extremely weak, which spares the scenario from many, though not all, of the constraints placed by collider experiments on new particles and by precision tests of the Standard Model.

With so many of the conventional means of searching for this dark matter scenario ruled out or greatly weakened in their sensitivity, the question naturally arises of

whether there are any unconventional means by which it could be found. Direct dark matter detection experiments attempt to discover dark matter by recording the recoils of nucleons from nucleon-dark matter scattering events. The low sensitivity of direct detection experiments to low mass dark matter is not due to the weak interaction strength of the dark matter with the Standard Model (though this does play a part), but rather because non-relativistic, low mass dark matter induces nuclear recoils too small to be detected by current generation experiments. However, the scattering interactions between dark matter and nucleons suggest the possibility of its production through proton-nucleon collisions in collider experiments, where the dark matter would then be boosted to relativistic speeds, rendering it detectable through its scattering in the experiment's detector.

As was previously suggested by Batell, Ritz and Pospelov [33] the proton beams at fixed target neutrino facilities have the ability to both deliver enormous luminosities, and are built to filter out most Standard Model particles so that the weakly interacting neutrinos can be detected, a combination of qualities that make them natural testing grounds for low mass hidden sector scenarios. There has been significant interest over the last several years in low mass hidden sector dark matter, resulting in a number of noteworthy papers proposing possible experimental searches (see e.g. [34, 35, 36, 37, 38, 39, 40, 33, 41, 42, 41, 43, 44, 16, 45, 46, 47, 48, 49, 50, 51, 52, 53, 54, 55, 56, 57, 58, 59, 60, 61, 62, 63, 64]).

This dissertation describes our efforts to calculate the sensitivity to hidden sector dark matter of a number of fixed target experiments that are conducting or have completed their experimental program: LSND, MiniBooNE, and T2K [65, 66, 15]. In addition, we have also made projections for experiments that are still in the planning stages, partly in hopes of providing additional motivation for their approval and subsequent funding. These include: SHiP [67], COHERENT and CENNS [22]. Finally, we assisted in the motivation of a year-long light dark matter focused beam dump run at MiniBooNE, and joined the collaboration in order to aid in the analysis of their data [14]. Towards this end, a Monte Carlo code was written to simulate the production of dark matter and its interactions with a neutrino detector. While this code was originally written with MiniBooNE in mind, it has been used in projections for a number of other fixed target experiments.

The work in this thesis is based upon four primary publications:

1. "Observing a light dark matter beam with neutrino experiments" [65] in which we consider the sensitivity of the LSND and MiniBooNE fixed target neutrino

experiments to kinetically mixed U(1)′ dark matter scenarios. This paper focused on dark matter masses of a few MeV, which could in theory explain the 511 keV INTEGRAL signal [13]. Dark matter production from π^0 and η decay to an on-shell mediator boson was considered, and we wrote a very basic Monte Carlo code to simulate the dark matter production distribution. Both elastic electron- and nucleon-dark matter scattering were considered as signal channels. It was determined that this scenario was strongly constrained for the parameter space that could explain the 511 keV line, and was later updated to use null results from the LSND experiment to place strong limits on dark matter with masses less than the pion mass.

2. "Signatures of sub-GeV dark matter beams at neutrino experiments" [66] expanded on the previous paper by introducing direct parton level production, extending the mediator masses for which dark matter production could be simulated to several GeV. The focus was shifted from low mass dark matter to a broader attempt to cover the kinetic mixing parameter space. This involved a reanalysis of the sensitivity of MiniBooNE, as well as new analyses employing T2K's ND280 detector and the MINOS near detector.

3. "Leptophobic Dark Matter at Neutrino Factories" [15] examined a variant of the kinetic mixing scenario, in which the mediator coupled to baryon number rather than mixing with hypercharge. This paper introduced new vector mixing production channels that bridged the gap in mass coverage between the η mass and the GeV scale required for parton level production. A new version of the simulation was written to handle the now significantly larger number of production channels. This work focused on the sensitivity of the MiniBooNE experiment in beam-dump configuration to the leptophobic scenario, which was determined to possess a reach in terms of the baryonic fine structure constant of $\alpha_B \sim 10^{-6}$.

4. "Light new physics in coherent neutrino-nucleus scattering experiments" [22] examined the reach of two prospective coherent neutrino-nucleus scattering fixed target experiments, COHERENT and CENNS. This was the first publication to make use of the most recent version of the simulation code, now written in C++. These experiments were determined to possess sensitivity for low mass mediators well beyond current limits in both the kinetic mixing and leptophobic

scenarios.

This work is divided into seven chapters, including this short introduction. We now provide a brief overview of the contents of each chapter:

Chapter 2 makes the case for the existence of dark matter, covering the many pieces of gravitational evidence that support its existence, and provides an overview of current experimental and observational efforts attempting to discover details of its particle nature. We also touch on the Weakly Interacting Massive Particle paradigm and review a possible production mechanism for the presently observed dark matter energy density: it is a thermal relic from the early universe.

Chapter 3 establishes our motivation for studying low mass hidden sector dark matter, and lays out how such a scenario can be constructed. We will review the phenomenology of a hidden sector dark matter scenario gauged under a $U(1)'$ symmetry and coupled to the Standard Model through kinetic mixing between the $U(1)'$ gauge boson and the photon. The existing constraints on this scenario will be reviewed, along with the conditions for reproducing the observed relic density. We will also consider, in less detail, a leptophobic scenario in which we gauge baryon number, allowing the mediator to couple to any particle possessing baryon number with the option of not directly interacting with leptons or photons.

Chapter 4 suggests a relatively new search avenue for light dark matter, Fixed Target Neutrino Facilities. We will cover a number of channels through which dark matter might be produced at such a facility, and calculate both the amount and the distribution of the dark matter that would be produced under both the kinetic mixing and leptophobic scenarios. We will also discuss the signal channels through which the presence of hidden sector dark matter could be detected by these experiments.

Chapter 5 tackles the numerical challenges of calculating the expected dark matter signal at a fixed target neutrino facility. A dark matter production and scattering code was written for this purpose, originally to support the MiniBooNE beam dump analysis and later adapted for use in predicting potential dark matter signals at other fixed target experiments. This section documents the operation of the simulation, and provides a guide on how the code is run and customized for any fixed target facility of interest.

Chapter 6 summarizes all of the results found by implementing the results of chapter 4 with the code described in chapter 5. We provide a brief description of a number of fixed target experiments, some of which are still in the proposal stages, and describe expected dark matter signals for each. We propose cuts which could allow the experiment to discriminate between dark matter and neutrino events when necessary, and make estimates of constraints that could be imposed by each experiment where possible. Plots of the hidden sector parameter space with sensitivity curves for each fixed target experiment are also included.

Chapter 7 brings this work to an end with a summary of what was accomplished, and some words on future possibilities.

Chronological List of Contributions and Publications

1. P. deNiverville, M. Pospelov and A. Ritz, "Observing a light dark matter beam with neutrino experiments," Phys. Rev. D **84**, 075020 (2011) doi:10.1103/PhysRevD.84.075020 [arXiv:1107.4580 [hep-ph]] [65].

2. P. deNiverville, D. McKeen and A. Ritz, "Signatures of sub-GeV dark matter beams at neutrino experiments," Phys. Rev. D **86**, 035022 (2012) doi:10.1103/PhysRevD.86.035022 [arXiv:1205.3499 [hep-ph]] [66].

3. R. Dharmapalan *et al.* [MiniBooNE Collaboration], "Low Mass WIMP Searches with a Neutrino Experiment: A Proposal for Further MiniBooNE Running," arXiv:1211.2258 [hep-ex] [14].

4. R. Essig *et al.*, "Working Group Report: New Light Weakly Coupled Particles,"arXiv:1311.0029 [hep-ph] [16].

5. B. Batell, P. deNiverville, D. McKeen, M. Pospelov and A. Ritz, "Leptophobic Dark Matter at Neutrino Factories," Phys. Rev. D **90**, no. 11, 115014 (2014) doi:10.1103/PhysRevD.90.115014 [arXiv:1405.7049 [hep-ph]] [15].

6. S. Alekhin *et al.*, "A facility to Search for Hidden Particles at the CERN SPS: the SHiP physics case," arXiv:1504.04855 [hep-ph] [67].

7. P. deNiverville, M. Pospelov and A. Ritz, "Light new physics in coherent neutrino-nucleus scattering experiments," Phys. Rev. D **92**, no. 9, 095005 (2015) doi:10.1103/PhysRevD.92.095005 [arXiv:1505.07805 [hep-ph]] [22].

Chapter 2

Dark Matter Background

2.1 Introduction

There is an overwhelming case for the existence of Dark Matter, some hidden mass which dominates the matter density of the universe. Many observational and experimental efforts are under way to observe it by non-gravitational means, none of which have detected an unambiguous signal. We know nothing of its particle nature, and have placed only the weakest of limits on its mass. The nature of its interactions with the Standard Model are unknown beyond their incredible weakness. All evidence of its existence comes to us indirectly from its gravitational effects on the visible baryonic matter.

Despite the many dark matter unknowns, it is not a complete mystery. It is clear that while some of the dark matter is composed of baryonic matter, either tied up in dim, low mass stars and black holes or large clouds of gas surrounding galaxies, the majority is non-baryonic. Cosmological and astrophysical estimates show that 27% of the energy density of the universe is made of dark matter, more than five times the baryonic matter's 5% [68]. The remainder of the energy density is largely composed of the even less well understand dark energy, with a small contribution from radiation in the form of photons. In addition, dark matter does not appear to be hot, or relativistic, and is instead cold, non-relativistic, or warm, some intermediate state between the two extremes.

We will discuss the astrophysical and cosmological evidence for the existence of dark matter in section 2.2, how experimental efforts search for it by means other than its gravitational interactions in section 2.4, and review one of the most straightforward

production mechanisms in section 2.3. We draw heavily from lecture notes and review papers for the material in this section [69, 70, 25, 71, 72].

2.2 The Case for Dark Matter

The influence of dark matter is felt on a wide array of distance scales, from the smallest dwarf galaxies to cosmological measurements of the universe as a whole. Its effects are visible throughout the universe's history, beginning with the Cosmic Microwave Background and extending to present day. In this section, we will discuss the various means by which dark matter's influence on the universe are measured, and have drawn heavily from Bertone, Hooper and Silk's excellent dark matter review [69], as well a more recent review of astrophysical signatures of dark matter [71].

The first indication that an invisible source of mass was present in the universe came from the work of Fritz Zwicky in the 1930's[1] [73, 74]. Zwicky applied the Virial theorem to the Coma Cluster, comparing the amount of visible mass in the cluster to the rotational speed of its component galaxies. The Virial theorem is a simple statement that relates the kinetic energy of a stable system to its potential energy,

$$\langle T \rangle = -\frac{\langle U \rangle}{2}, \tag{2.1}$$

where T is the kinetic energy, U the potential energy, and the brackets indicate time averaging. Zwicky found that this relation was not satisfied by the Coma Cluster. The observable galaxies were moving far too rapidly to be bound in stable orbits by their gravitational potentials, to the extent that the mass of the Coma Cluster would have had to be on the order of a hundred times larger than was suggested by its observable luminous matter. Zwicky did not know at the time that galaxies were surrounded by several times their mass in hot gases, but even with this added contribution the cluster would have required six times the baryonic mass in order to be stable. This observation was unfortunately ignored for the next forty years [69, 25].

[1] This statement is not entirely accurate. The existence of Neptune, an until then unseen source of mass in the solar system, was predicted by French astronomer Verrier and English astronomer Adams due to its gravitational effects on the orbit of Uranus. Anomalies in the orbit of Mercury were also posited to be due to the presence of an undiscovered planet called Vulcan, though they were later explained by corrections from General Relativity[69].

2.2.1 Galactic Scale

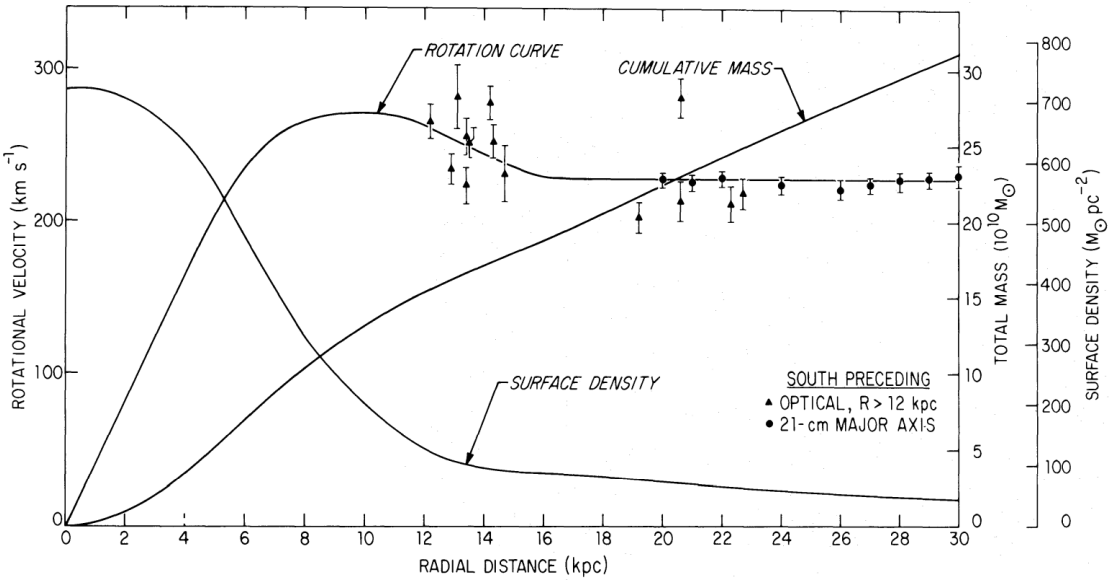

Figure 2.1: Rotation curves of M31, frequently called the Andromeda Galaxy. The rotation curve strongly suggests that the mass contained within the radial distance continues to increase at a roughly constant rate out far past the optical disk of the galaxy. The majority of the luminous matter is concentrated in the optical disk, and were it the primary source of gravitational potential, the rotational speed would be expected to drop as $r^{-1/2}$ for $r > r_{\text{disk}}$ [1]. Copyright AAS. Reproduced with Permission.

Galactic rotation curves clearly demonstrate the influence of dark matter on observable luminous matter. These curves plot the average rotational velocity at a given distance from the center of a galaxy. Using the equation for uniform circular motion, we can calculate the expected speed of an object orbiting the center of a galaxy,

$$v = \sqrt{\frac{GM(r)}{r}}, \tag{2.2}$$

where G is the gravitational constant, $M(r)$ is the the mass contained inside an orbit of radius r, $M(r) = 4\pi \int_0^r dr' r' \rho(r')$, and $\rho(r)$ is the mass density at some radius r. If we assumed that the majority of the mass in a galaxy is concentrated in the disk ($\rho(r > r_{\text{disk}}) = 0$), then M should be almost constant for radii greater than that of the luminous disk, and we expect $v \propto \sqrt{\frac{1}{r}}$. Observations of 21 cm atomic hydrogen lines tell a very different story, as the rotational speed is observed to become constant at large radii (see Fig. 2.1) [75, 1, 70]. This suggests that the mass increases as

$M(r) \propto r$ beyond the galactic disk, and that the luminous matter of the galaxy is actually embedded in a much larger dark matter sphere or halo.

There are a number of other anomalies that provide evidence of the existence of dark matter at the galactic scale [69]. The virial theorem and velocity distributions return as evidence of dark matter when looking at satellite galaxies around spiral galaxies [76, 77, 78]. One can also look at the velocity dispersion of the baryonic components of dwarf galaxies, small galaxies that appear to be massively dominated by dark matter [79] to the extent that a mere 5% of the galaxy's mass may be baryonic. The weak gravitational lensing of distant objects by unseen foreground structures [80, 81], and the modulation of strong lensing around massive elliptical galaxies [82, 83] provide additional clues.

As an interesting side note, models of Modified Newtonian Dynamics (MOND), theories which posit that Newton's laws of gravity are altered at large distances, can also be used to explain the behavior of galactic rotation curves. However, they have more difficulty explaining other anomalies, such as the weak gravitational lensing phenomena mentioned previously, for which the dark matter hypothesis provides a natural explanation [71, 84, 85].

2.2.2 Galaxy Cluster Scale

Galaxy clusters, large conglomerations of hundreds or thousands of gravitationally bound galaxies[2], provide the next mass scale of interest. Evidence of hidden mass can be found by estimating the mass of the cluster (e.g. through the use of the Virial theorem on the observable objects) and comparing this to the mass of the luminous galaxies and slightly less visible hot gas present in the cluster.

One can use hydrostatic equilibrium in a spherically symmetric system to derive an estimate of the temperature of an ideal gas in galaxy cluster[69],

$$kT \approx (1.3 - 1.8)\,\mathrm{keV} \left(\frac{M(r)}{10^{14}\,M_\odot}\right)\left(\frac{1\,\mathrm{Mpc}}{r}\right), \tag{2.3}$$

where $M_\odot \approx 2 \times 10^{30}\,\mathrm{kg}$ is a solar mass, $10^{14}\,M_\odot$ is the expected baryonic mass for the cluster. The observed temperature of $10\,\mathrm{keV}$ is considerably higher, suggesting a dark matter component of the cluster that is far larger than the baryonic component.

[2]Our galaxy, the Milky Way, is part of the Virgo Cluster. The Coma Cluster, mentioned in the introduction, provides another example.

Two other techniques for measuring the mass involve the use of X-ray emissions from the aforementioned hot gas of the cluster to trace its distribution and movement, and the use of weak gravitational lensing of distant objects to measure the mass in the foreground. These two techniques have been combined when analyzing the collisions between galaxy clusters, with perhaps the most famous example coming from the Bullet Cluster[3]. By combining X-ray observations of the cluster's hot gas [86] from the Chandra X-Ray Observatory with weak gravitational lensing data [87] from the Hubble Space Telescope, the Wide Field Imager and the Magellan Telescopes, astronomers can map the distribution of both the baryonic matter and the gravitational potential in the cluster. The x-ray observations show that the baryonic gas has slowed due to collisions, while most of the gravitational potential of the two clusters, as mapped by gravitational lensing, has continued moving along a ballistic trajectory, leaving much of the observable gas behind. This provides a clear example of two dark matter halos passing through one another with minimal disruption due to their very weak self-interactions.

2.2.3 Cosmological Scales

While reasonable estimates of both baryonic and dark matter densities in the universe can be made by observing galaxies and galaxy clusters in the night sky, the best measurements come from cosmological observations of the early universe. Before we can discuss these signals, it is best to cover some history as it is currently understood. Temperatures will be expressed in terms of electron volts with the conversion

$$\mathrm{eV} = k_B \times 11604.505\,\mathrm{K}, \tag{2.4}$$

where k_B is the Boltzmann constant. The universe began in an incredibly energetic state called the Big Bang, and has been expanding and cooling ever since. The early universe was sufficiently high temperature ($T \gtrsim$ few GeV) that heavy, exotic particles could be produced efficiently, but they largely decayed or annihilated to lighter Standard Model particles as the temperature of the universe dropped below their masses (We will return to this later when discussing thermal relic dark matter in section 2.3). The earliest signal originates from $\mathcal{O}(100\,\mathrm{keV})$, when protons and neutrons fused together in a process called Big Bang Nucleosynthesis (BBN). The

[3]Also called 1E 0657-56

abundances of the light elements observed in the universe today can be compared with those predicted by BBN, and barring some significant anomalies show good agreement with theoretical predictions. At this point the universe was opaque, that is, it was full of free electrons and charged nuclei and photons could not travel far before scattering. As the universe cooled further, photons lost the energy required to regularly ionize Helium and Hydrogen, and electrons were soon bound with protons into neutral atoms. This is somewhat oddly called Recombination, and it marks the formation of the Cosmic Microwave Background, when photons last scattered before the universe became transparent (as defined by their mean free path becoming larger than the size of the universe).

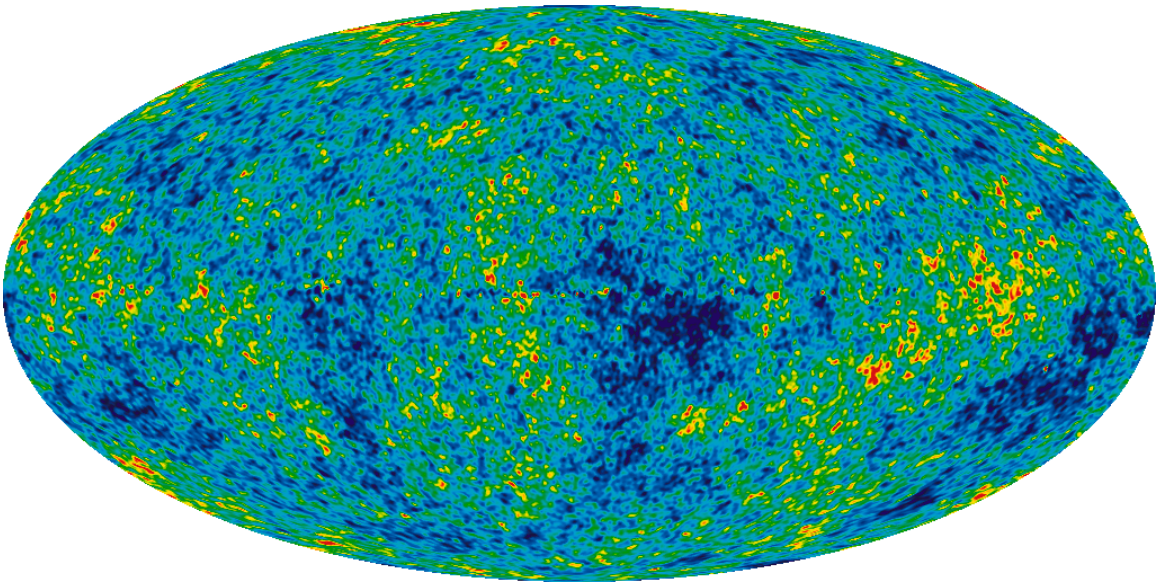

Figure 2.2: Map of temperature differences created with nine years of WMAP data. The range of temperatures shown vary by $\pm 200\mu\,\mathrm{K}$. The effects from our own galaxy were subtracted from the image. From NASA / WMAP Science Team http://map.gsfc.nasa.gov/.

Satellite telescopes like Planck[88], WMAP[4][89, 90] and COBE[5] [91] allow us to make precise measurements of CMB temperature anisotropies (see Fig. 2.2). The CMB has cooled over time as its constituent photons have been redshifted to lower temperatures, and today its temperature is measured to be $T = 2.726\,\mathrm{K}$. The CMB is very near to isotropic, with fractional variations of $\mathcal{O}(10^{-5})$. The temperature

[4]Wilkinson Microwave Anisotropy Probe
[5]Cosmic Background Explorer

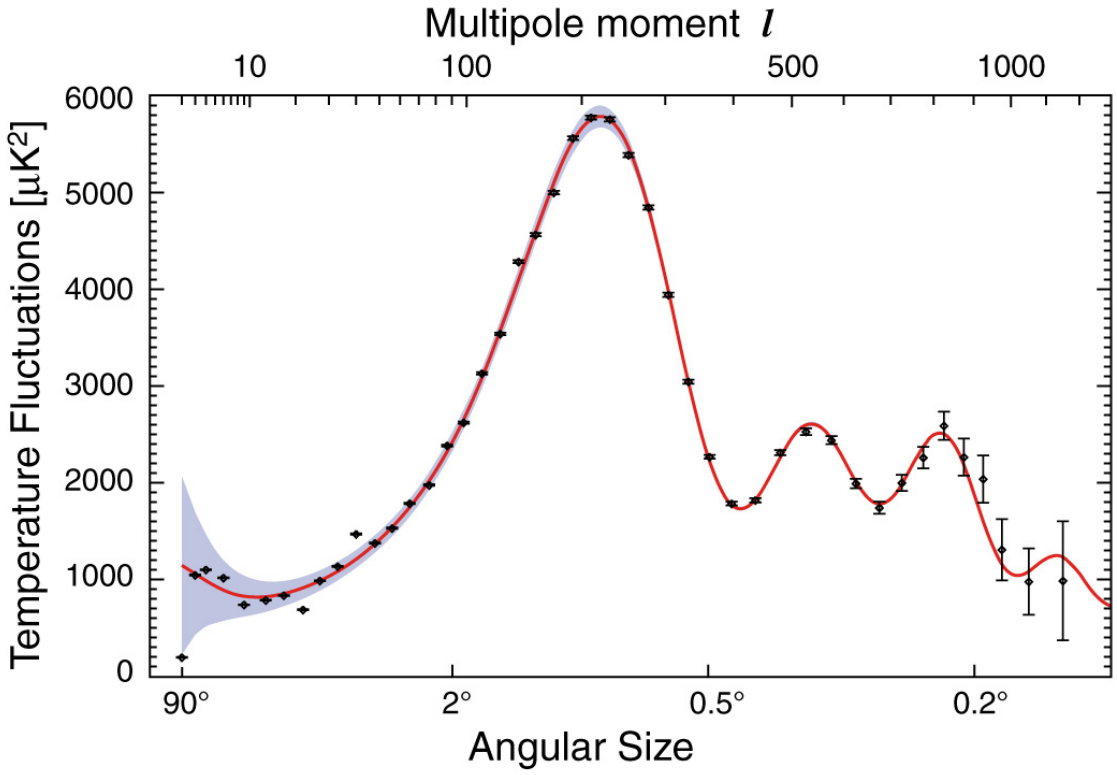

Figure 2.3: A plot of the CMB power spectrum $l(l+1)C_l/2\pi$ made using WMAP data. From NASA / WMAP Science Team http://map.gsfc.nasa.gov/.

anisotropies are expressed as a power series in terms of spherical harmonics

$$\frac{\delta T}{T}(\theta,\phi) = \sum_{l=2}^{+\infty} \sum_{m=-l}^{+l} a_{lm} Y_{lm}(\theta,\phi). \tag{2.5}$$

Normally plotted is the variance,

$$C_l \equiv \langle |a_{lm}|^2 \rangle \equiv \frac{1}{2l+1} \sum_{m=-l}^{+l} |a_{lm}|^2 \tag{2.6}$$

in the form $l(l+1)C_l/2\pi$ (see Fig. 2.3). By comparing the relative heights of the peaks, and in combination with other measurements, precision calculations of the matter density, $\Omega_m = 0.315$ and the baryon density, $\Omega_b = 0.0499$, can be made [68].

Other cosmological means can be employed to estimate the baryonic matter density, including comparisons with the predictions of BBN and the Lyman-α forest. The abundances of light elements produced in the early universe during BBN provides the

earliest data point available. The ratios of light elements: D/H, He/H, and Li/H can be predicted from BBN calculations and compared with actual measurements of their abundances [92]. One can measure the abundance of elements at later times by examining the absorption lines in the light of very distant quasars in the Lyman-α Forest [93]. Constraints can be placed on cosmological models by comparing these measurements with model predictions derived from large simulations (see e.g. [94]).

2.3 Dark Matter Production: The Thermal Relic

The most popular paradigm for dark matter scenarios is that of the Weakly Interacting Massive Particle (WIMP), and for the remainder of this work we will assume that dark matter follows this convention. This is not to say there are no other possibilities (see [95] for a discussion), but WIMPs provide a wide array of natural dark matter models with a natural production mechanism.

WIMP dark matter brings with it a natural production process: the present day dark matter density is a relic left over from the much higher temperature early universe. We will begin by positing the existence of a stable state χ, which will serve as our dark matter candidate. In the early universe, χ could be produced through processes involving Standard Model particles Y, and consequently could also annihilate into SM particles Y: $\chi\bar{\chi} \leftrightarrow Y\bar{Y}$. Alternatively, should our dark matter candidate be a Majorana particle, it would be written as $\chi\chi \leftrightarrow Y\bar{Y}$. In the early universe, when the temperature $T \gg m_\chi$, where m_χ is the mass of the dark matter candidate, the production and annihilation processes would be equally efficient, and χ would be present in large abundances alongside the more familiar Standard Model particles. As the temperature declines, the χ production processes will be increasingly suppressed, while annihilation will proceed at a rate proportional to n_χ^2 where n_χ is the number density of the dark matter. So long as χ remains in thermal equilibrium with the thermal bath of Standard Model particles which fill the universe, it will constantly approach its equilibrium number density. In the nonrelativistic regime, where $T \lesssim m_\chi$, this can be written as,

$$n_{\text{eq}} = g_\chi \left(\frac{m_\chi T}{2\pi}\right)^{3/2} e^{-m_\chi/T}, \tag{2.7}$$

where g_χ is the number of internal degrees of freedom for our dark matter particle.

Were production and annihilation the only processes affecting the number density, we would expect the dark matter number density to rapidly dwindle to near zero as

the temperature declined, a behavior which is in large disagreement with the dark matter domination of the matter density observed in the present day universe. One possible solution is that dark matter is asymmetric, somehow favoring dark matter particles over antiparticles. However, we will instead consider the concept of thermal freeze out, in which the dark matter number density is diluted by the expansion of the universe to the point that annihilation also becomes inefficient due to the paucity of dark matter particles with which to annihilate. The combined effect of Hubble expansion and the tendency for the dark matter density to move towards its equilibrium density are captured in the Boltzmann equation,

$$\frac{dn_\chi}{dt} + 3Hn_\chi = -\langle\sigma v\rangle \left(n_\chi^2 - (n_\chi^{\rm eq})^2\right) \tag{2.8}$$

where H is the Hubble parameter representing the expansion rate of the Universe. H can be written as,

$$H = \frac{\dot{a}}{a} = \sqrt{\frac{8\pi^3\rho}{3M_{\rm Pl}}}, \tag{2.9}$$

where a is the scale factor of the universe, $M_{\rm Pl}$ is the Planck Mass, ρ is the energy density of the universe and $\langle\sigma_{\chi\bar{\chi}}v\rangle$ is χ's self-annihilation cross-section multiplied by the relative speed between two dark matter particles v, thermally averaged over the velocity of χ particles. The velocity distribution is normally taken to be a Maxwell-Boltzmann distribution centered on some average speed $\langle v\rangle$.

The Boltzmann equation is frequently rewritten in terms normalized by the entropy density, s, which due to the conservation of entropy per comoving volume,

$$S = sa^3 = \text{constant}, \tag{2.10}$$

effectively hides the effect of Hubble expansion. We define new dimensionless variables $Y \equiv n/s$ and $x \equiv m/T$, and can then rewrite 2.8 as

$$\frac{dY}{dx} = \frac{1}{3H}\frac{ds}{dx}\langle\sigma v\rangle \left(Y^2 - Y_{\rm eq}^2\right). \tag{2.11}$$

The temperature at which freeze-out occurs, $T_{\rm FO}$, is determined by numerically solving the Boltzmann equation. To do this, we expand the thermally averaged cross-section in terms of velocity,

$$\langle\sigma_{\chi\bar{\chi}}v\rangle = a + b\langle v^2\rangle + \mathcal{O}(v^4). \tag{2.12}$$

We then determine the freeze-out solution by iteratively solving the following equation [69],

$$x_{\rm FO} = \frac{m_\chi}{T_{\rm FO}} \approx \ln\left(c(c+2)\sqrt{\frac{45}{8}}\frac{g}{2\pi^3}\frac{m_\chi M_{\rm PL}(a+6b/x_{\rm FO})}{g_*^{1/2}x_{\rm FO}^{1/2}}\right), \tag{2.13}$$

where c has been numerically determined to be ~ 0.5, g is the number of degrees of freedom of the dark matter and g_* is the total number of relativistic degrees of freedom in the Standard Model. It decreases with falling temperature, as heavy species become nonrelativistic. One can then find an approximate expression for the WIMP density in the present day Universe,

$$\Omega_\chi h^2 \approx \frac{1.04\times 10^9 {\rm GeV}^{-1}}{M_{\rm PL}}\frac{x_{\rm FO}}{g_*^{1/2}(a+3b/x_{\rm FO})}. \tag{2.14}$$

Of particular interest is the annihilation rate required to reproduce the observed relic density [96],

$$\Omega_\chi h^2 \approx \frac{3\times 10^{-27}\,{\rm cm}^3/{\rm s}}{\langle\sigma_{\chi\bar{\chi}}v\rangle}, \tag{2.15}$$

where $h = 0.673$ is the Hubble scale factor [68] and Ω_χ is the fraction of the energy density of the universe made up of dark matter. Ω_i is defined as

$$\Omega_i \equiv \frac{\rho_i}{\rho_c}, \tag{2.16}$$

where ρ_i is the energy density of i and ρ_c is the critical density of the universe, defined as

$$\rho_c \equiv \frac{3H^2}{8\pi G}. \tag{2.17}$$

2.4 Searches

In section 2.2, we reviewed the gravitational evidence for the existence of dark matter. While this evidence is strong, it leaves us ignorant of the particle nature or mass of dark matter. To learn more, we need to observe its non-gravitational interactions with Standard Model matter. To this end, three broad search strategies are employed by a number of experiments around the world: Direct Detection, Indirect Detection and Collider Production. Each strategy reflects a different orientation of dark matter-Standard Model interactions.

2.4.1 Direct Detection

Direct detection is perhaps the most straightforward detection strategy, though by no means a simple one to utilize. These experiments probe the dark matter parameter space by searching for recoils from scattering interactions between halo dark matter passing through the earth and nuclei or electrons in their detector. Eventually, these experiments might even study the dark matter-Standard Model recoil energy spectrum.

These experiments have the advantage of being able to place relatively model independent[6] limits on the strength of dark matter interactions with SM particles, so long as dark matter couples to leptons or baryons in some way. The sensitivity of direct detection efforts weakens dramatically for very massive or very light dark matter. For low mass dark matter, the dark matter's momentum becomes correspondingly small, as even very light dark matter is non-relativistic. For elastic scattering off nuclei, the recoil can be calculated as [25]

$$E_{\text{recoil}} = \frac{\mu(m_\chi, M_{\text{nucleus}})^2 v^2 (1 - \cos(\theta))}{M_{\text{nucleus}}}, \tag{2.18}$$

where v is the speed of the dark matter, m_χ is the dark matter mass, $\mu(m_1, m_2) = \frac{m_1 m_2}{m_1 + m_2}$ and θ is the scattering angle of the nucleus. For low dark matter masses, this quickly declines beyond the point which dark matter experiments can detect, though they are making constant efforts to push the recoil threshold required for detection to lower energies (see [8] for an example of large recent improvements). At high masses, a different problem emerges in that the dark matter energy density is constant, and the flux then scales as

$$\Phi_\chi \propto \frac{1}{m_\chi}, \tag{2.19}$$

and the scattering rate naturally declines with increasing dark matter mass. These behaviors are illustrated for dark matter masses below a few GeV and above a TeV by figure 2.4.

While many dark matter particles are expected to pass through the earth every second, the actual interaction rates are tiny, forcing direct detection experiments to constantly battle against backgrounds. These experiments are frequently built deep

[6]The limits placed by direct detection experiments can be significantly altered if the scattering between dark matter and Standard Model matter is inelastic. They are also highly dependent on the local dark matter density and velocity distribution.

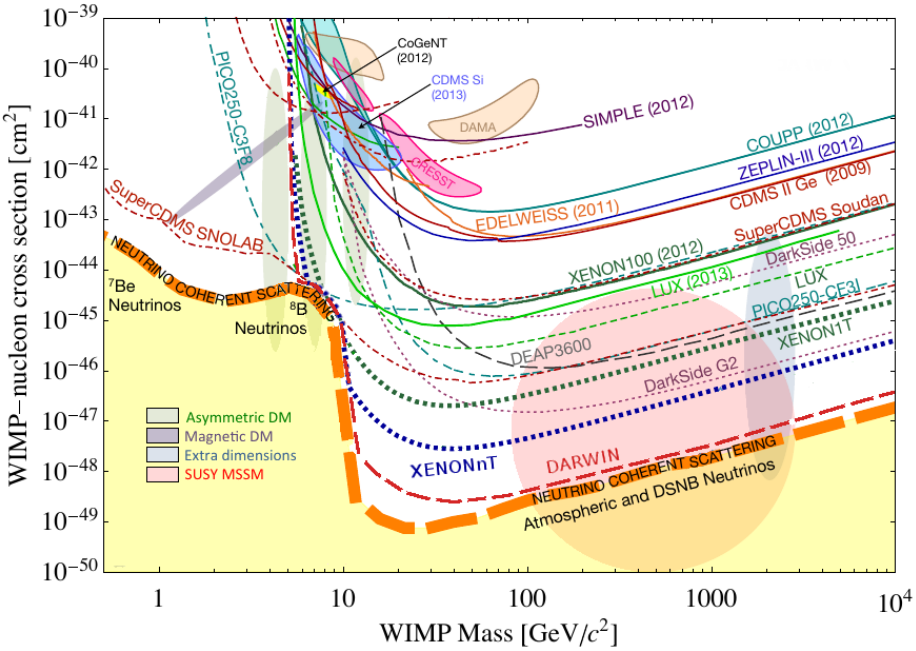

Figure 2.4: Plot of direct detection limits as of 2014. The solid lines are limits already placed by experimental analyses, and the dotted lines projected sensitivities by future analyses. Parameter space above the curves is excluded, while that below the curves is allowed. Shaded regions marked DAMA, CDMS and CRESST represent possible signal regions, though note that these are directly in conflict with each other and the exclusion limits placed by other experiments. The lines near the bottom of the plot mark where atmospheric and solar neutrinos begin to constitute a significant background in dark matter searches, and is likely to dramatically increase the difficulty of direct detection analyses. Reprinted from Proceedings, 13th International Conference on Topics in Astroparticle and Underground Physics (TAUP 2013), Vol. 4, Laura Baudis, WIMP Dark Matter Direct-Detection Searches in Noble Gases, 50-59, Copyright 2014, with permission from Elsevier [2].

underground in abandoned mines and include sophisticated veto systems in order to reduce cosmological backgrounds, but even with these measures they must still contend with cosmic neutrino induced events and the radiation present in earth itself. Understanding their backgrounds is essential to making an unambiguous dark matter detection.

Fixed target experiments employ a variety of detector media and techniques, and this diversity of approaches is advantageous to the dark matter search as a whole. The best limits are placed by Spin-Independent (SI) dark matter searches, which are capable of probing vector and scalar couplings between dark matter and the SM. Their sensitivity is greatly increased by the enormous enhancement of coherent scattering

cross sections on heavy nuclei at low energies, where the scattering rate is [25]

$$\sigma_{A,Z} = (Z + (A - Z)(f_n/f_p))^2 \, \frac{\mu_A^2}{\mu_p^2} \sigma_p, \tag{2.20}$$

where σ_p is the dark matter-proton scattering cross section, $\mu_X = m_X m_{\rm DM}/(m_X + M_{\rm DM})$ is the reduced mass, Z is the number of protons, A is the number of nucleons, $f_{n(p)}$ is the WIMP coupling to neutrons (protons), and a $f_n = f_p$ implies an isospin conserving interaction. By utilizing heavy nuclei with different ratios of A/Z, one can probe the dark matter couplings to neutrons and protons. Currently, the best SI limits are placed by CRESST-II [8], SuperCDMS [10], CDMSlite [11], XENON100 [5], LUX [12].

Another strategy is to look for Spin-Dependent (SD) scattering, which probes axial-vector interactions. The limits from spin-dependent scattering tend to be far weaker as they scale with the spin of the particle, $\propto J(J+1)$, rather than the number of nucleons squared. There is no great advantage from using heavy nuclei that SI searches enjoy. The best limits on spin-dependent scattering are placed by PICASSO [97], SIMPLE [98], and COUPP[99].

Other interesting handles available to direct detection include searches for annual modulation in the dark matter signal, and the use of directionality [72]. An annual modulation in the dark matter recoil signal is expected due to the rotation of the earth around the sun each year. This increases (or decreases) the relative speed between earth and the galactic reference frame, which should result in greater (lesser) interaction rate between halo dark matter and a detector's nuclei. The greatest enhancement to signal is expected around June $2^{\rm nd}$, and the greatest suppression in December. The DAMA/LIBRA experiment is a particularly noteworthy annual modulation experiment, as they have reported a 9.3σ annual modulation signal [100]. Whether this signal represents the discovery of dark matter or not is hotly contested, as several direct detection experiments have reported null results directly in contradiction with the DAMA/LIBRA sensitivity. CoGeNT has also reported an excess at a much lower confidence level of 1.7σ, for different combinations of nucleon scattering cross-section and mass than DAMA/LIBRA [101]. Directionality could also play a role in enhancing recoil rates in a given direction due to the Sun's orbit around the galaxy, the Earth's orbit around the Sun, and even the rotation of the Earth itself. DRIFT-II is currently the largest directional detection experiment in operation [102].

2.4.2 Indirect Detection

Rather than looking for WIMP interactions with SM particles directly, it is also possible to search for byproducts of WIMP annihilations or decays in the night sky with an indirect dark matter search. For this section we are indebted to the excellent set of TASI lecture notes by G. Gelmini, which provides a thorough treatment of indirect dark matter searches [25].

Solar Capture

The nearest possible signal originates from the Sun, and to a lesser extent the planets in our own solar system. Halo dark matter could scatter on nuclei in the Sun to a speed lower than the escape velocity, becoming captured by the gravity of the Sun. The capture rate is constant,

$$\Gamma_C = \sigma_S n_\chi, \tag{2.21}$$

where σ_S is the dark matter nucleon scattering cross section, n_χ is the dark matter's density and σ_S the rate at which dark matter particles are captured by the sun, and so we would expect the population of dark matter in the Sun to rise over time. This dark matter population would eventually be balanced by annihilation,

$$\Gamma_A = \langle \sigma_A v \rangle n_\chi^2, \tag{2.22}$$

where σ_A is the dark matter annihilation cross section either into neutrinos directly, or into other particles whose decays create neutrinos. These decay neutrinos could then be observed with large scale neutrino detectors on Earth, the premier example of which is the cubic kilometer scale IceCube detector in Antarctica [103]. It is interesting to note that because the Sun is primarily composed hydrogen, IceCube is also capable of placing competitive limits on Spin-Independent dark matter cross sections. We will revisit solar dark matter trapping and annihilation in section 3.4.

Gamma rays

Looking further afield we arrive at Gamma Ray Astronomy, where we search for the products of dark matter annihilations either directly into photons or into heavier SM particles whose decays eventually produce photons. Gamma rays are particularly useful because the universe is nearly transparent to them for energies less than a

few TeV[7], and so they retain information about the location of their source. Since the annihilation rate scales as n_χ^2, we are particularly interested in regions of high dark matter density, such as the galactic core of the Milky Way, other galaxies and galaxy clusters. These locations bring complications, in that they are also home to the largest concentrations of baryons and the backgrounds that come with them. Dwarf Spheroidal galaxies are also good candidates for gamma ray searches despite their small sizes, as they are strongly dark matter dominated.

The most obvious and unambiguous dark matter signal would result from direct annihilation into photons $\chi\bar{\chi} \to \gamma\gamma$, as this would produce a monochromatic signal with $E_\gamma = m_\chi$. However, dark matter is unlikely to directly couple to photons, and this process is therefore expected to be loop suppressed. It is more likely that the dark matter will annihilate into heavier SM particles, whose decay chains to stable particles should produce a spectrum of photons with a cutoff at some energy m. This does have an upper limit, as the mass spectrum of SM particles only reaches about 174 GeV with the top quark. These signals could be detected using both satellite telescopes like the Fermi Large Area Telescope [104], or ground-based air Cherenkov experiments like HESS [105], MAGIC [106] and VERITAS [107].

Cosmic rays

Cosmic rays in the form of high energy protons, antiprotons, electron, and positrons provide a final dark matter probe in the night sky. Cosmic rays interact with the magnetic fields of galaxies and rapidly lose most of their energy, and do not provide a clear path to their production point. However, antiparticles are relatively rare in the universe today, and dark matter annihilation would be expected to produce both particle and antiparticle in equal numbers. We can therefore glean some interesting hints from the energy distribution of the relative fluxes of particle and antiparticle. To this end, an excess in the positron flux for incident energies between 10 and 100 GeV provides a particularly promising anomaly. This was originally seen by balloon borne experiments in the 1980's, and was in fact called the HEAT excess at the time. This excess was observed again by the PAMELA[8] collaboration (see Fig. 2.5) [4], and later confirmed by FermiLAT [108] and AMS [109]. Interestingly, no corresponding excess is observed in the antiproton flux, indicating that were this signal to be the result of

[7]For higher energies, they tend to be absorbed by the CMB. They are able to travel freely again once we reach energies of approximately 10^{10} GeV.

[8]Payload for Antimatter Matter Exploration and Light-nuclei Astrophysics

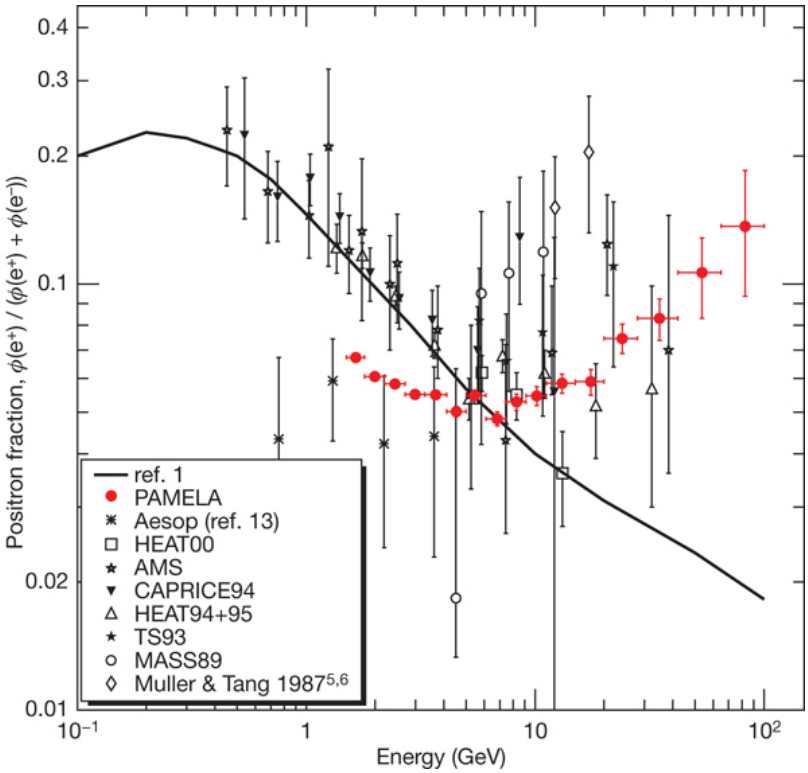

Figure 2.5: The observed excess in the positron fraction by PAMELA. The theoretically expected value is shown by the black line, adapted from [3]. A very significant rise above the expected value for the positron fraction is visible, and was later confirmed by two other satellites, FermiLAT and AMS-II. Reprinted by permission from Macmillan Publishers Ltd: O. Adriani *et al.* [PAMELA Collaboration], "An anomalous positron abundance in cosmic rays with energies 1.5-100 GeV," Nature **458**, 607-609, Copyright 2009 [4].

dark matter, it would have to be leptophilic, coupling preferentially to leptons rather than baryons or quarks.

2.4.3 Collider Production

Collider experiments such as the LHC, the Tevatron, or LEP2 provide a third means of searching for dark matter, by either attempting to produce the dark matter itself in some high energy collision, or by searching for deviations in precision measurements of otherwise well-understood Standard Model phenomena. These limits are by necessity highly model dependent, requiring both specific dark matter mass ranges and couplings.

Dark matter produced in a collider would not be easy to detect through its scatter-

ing, by definition it interacts very weakly with SM particles and, having a lifetime on the scale of that of the entire universe, is unlikely to decay into detectable Standard Model particles. Instead, these experiments search for missing transverse energy, that is, visible particles recoiling against the production of this invisible particle. When searching for a single photon recoiling against dark matter, this is called a monophoton search, and for a single gluon, a monojet. Previously, searches were performed using effective field theories, which would have assumed that any mediator between the dark matter and the Standard Model possessed a mass much larger than the momentum exchange. With the advent of the LHC these searches are frequently performed using simplified models, which are capable of describing all of the kinematics involved in dark matter production, but may still not be sufficient for more complex models that include non-dark matter candidates [110].

Dark matter can also be indirectly constrained through tests of the Standard Model. Of some interest to this work, and an example of a missing energy signal, is the invisible width of the Z-boson. If a dark matter candidate is sufficiently light, it may be produced in decays of Z bosons, $Z \to \chi\bar{\chi}$. The LEP2 experiment, an electron positron collider at CERN, has placed constraints on this width, imposing the limit $\Gamma_{Z\to\chi\bar{\chi}} < 4.2$ MeV [69]. Also of interest, and as will be discussed in further detail in section 3.2.1, is the measurement of the magnetic moment of the muon and the electron, for which there is good agreement between theory and experiment for the electron, but a large disagreement for the muon. Colliders have also imposed constraints on the masses of new charged particles, new gauge bosons, flavour changing neutral currents, and rare B decays place further constraints on the coupling between light dark matter and Standard Model states.

Chapter 3

Hidden Sector Dark Matter

3.1 Introduction

There is a lower bound on the mass of a thermal relic dark matter candidate whose interactions with the Standard Model are mediated by particles of weak scale mass and coupling strength (such as the Z boson). Lee and Weinberg noted that the annihilation cross section through weak scale mediators for heavy neutrinos was approximately

$$\langle \sigma v \rangle \approx \frac{G_F^2 m_L^2 N_A}{2\pi} \propto \frac{m_L^2}{m_Z^4}, \tag{3.1}$$

where m_L is the mass of the heavy neutrino, N_A is a fudge factor dependent on the number of annihilation channels, and G_F is the Fermi constant and m_Z is the Z boson mass. One can see that the annihilation rate declines rapidly with the mass of the particles, and expected relic abundance would increase in turn. The limit under which dark matter would be overproduced in the early universe and possess an abundance larger, possibly far larger, than is consistent with our astronomical observations is called the Lee-Weinberg bound [26]. There is a loophole in this limit, though: it assumes that annihilation proceeds through heavy Standard Model states. Introducing new light states neutral under the Standard Model gauge groups opens new dark matter to SM annihilation channels [111], greatly weakening constraints on the mass from the observed dark matter abundance. Suggesting the existence of new hidden sector states is not particularly exotic or novel, as many particles in the Standard Model are not charged under one or more of the Standard Model gauge groups, and hidden sector states are common component in theories of New Physics.

Of particular interest are dark matter scenarios that provide candidates with

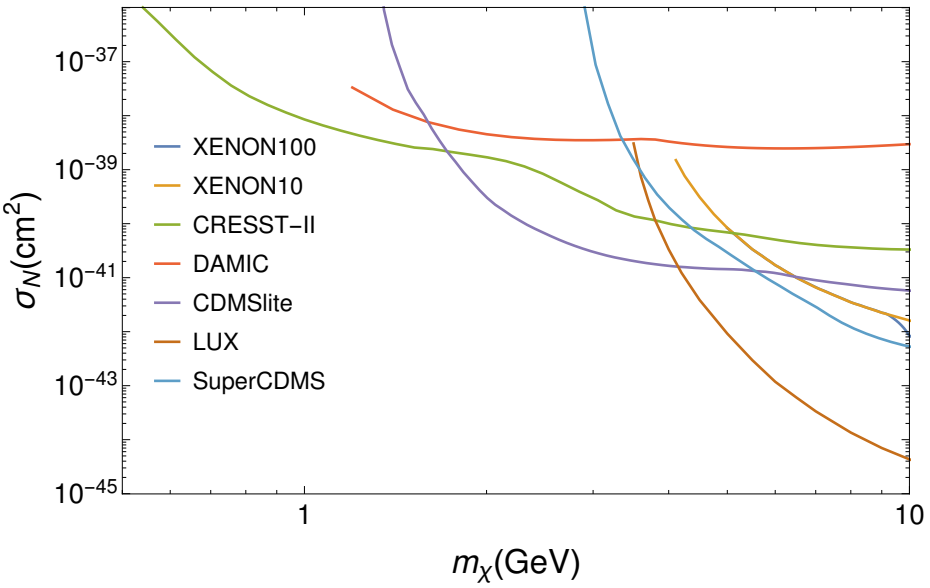

Figure 3.1: Low mass direct detection constraints as of May 2016. Regions above the curves are excluded. Results are from: XENON100 [5], XENON10 [6], CRESST-II [7, 8], DAMIC [9], SuperCDMS [10], CDMSlite [11], and LUX [12].

masses of a few MeV to a GeV, as the previously discussed direct detection constraints are dramatically weakened or non-existent in this mass range (see 3.1). In addition, low mass dark matter candidates could be produced in lower energy collider experiments, such as fixed target neutrino or beam dump experiments. These experiments possess far larger luminosities than proton colliders like the LHC or the Tevatron, opening the possibility of probing very small couplings to the Standard Model. In addition, there are a number of low energy anomalies which might be explained in part or in whole by the presence of new light states, depending on their couplings. Of particular interest in originally motivating this theoretical approach was the INTEGRAL 511 keV line [13], shown in Fig. 3.2. This line could potentially be explained by the annihilation of a dark matter candidate with a mass of a few MeV to electron-positron pairs. While it now appears that the positrons creating this signal are produced by a less exotic astrophysical source than dark matter, interest in light dark matter has not abated.

We now move onto a discussion of how a useful hidden sector containing dark matter can be formulated. The interactions of some hidden sector, uncharged under Standard Model gauge group, with Standard Model states can be parameterized as

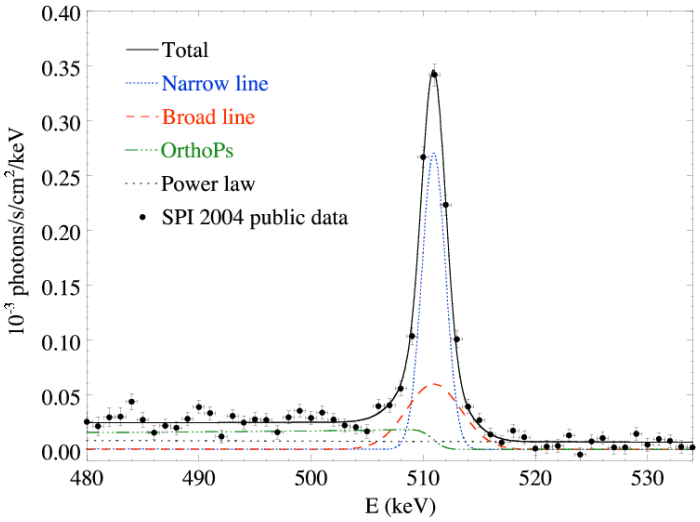

Figure 3.2: Fit of the spectrum measured by the SPI gamma-ray spectrometer aboard the INTEGRAL satellite. The dashed and dotted lines correspond to the broad and narrow peak components, respectively [13]. Pierre et. al., Astronomy & Astrophysics, vol 445, pages 579-589, 2006, reproduced with permission ©ESO.

[33]

$$\mathcal{L}_{\text{mediation}} = \sum_{k,l,n}^{k+l=n+4} \frac{\mathcal{O}_{\text{NP}}^{(k)} \mathcal{O}_{\text{SM}}^{(l)}}{\Lambda^n}, \tag{3.2}$$

where $\mathcal{O}$ are New Physics (NP) and Standard Model (SM) operators of dimension k and l, and Λ is some very large cut off scale. The case of the greatest importance for this work is that of marginal $n = 0$ interactions. The SM operators of lowest dimension are collectively known as portals [112, 113, 114, 115, 116], and include

$$\begin{array}{ll} F_{\mu\nu}^{Y} & \text{Vector Portal} \\ H^{\dagger}H & \text{Higgs Portal} \\ LH & \text{Neutrino Portal} \end{array}, \tag{3.3}$$

where $B_{\mu\nu}^{Y}$ is the hypercharge field strength, and H and L are the Higgs and Lepton doublets, respectively. These operators can be used to couple the SM to new physics without making assumptions about the mass scale of the new physics fields, and are unsuppressed by any heavy scale. The Higgs and Neutrino portals are less suitable for a low mass WIMP dark matter scenario for phenomenological reasons. Specifically, the Higgs portal is rendered problematic by measurements of Kaon decays (amongst others), while the direct coupling to neutrinos leads to unacceptable distortions of

observed supernova spectra through the suppression of neutrino energies for dark matter with a mass of a few MeV (See e.g. [117]).

One important concern for dark matter with sub-GeV mass is its commensurately high number density when compared to heavier dark matter scenarios, and the effect of this on its annihilation rate, both in the past and in the present day. Significant effort has been made to ensure that the annihilation rate is large enough so as to not overproduce[1] our dark matter candidate in the early universe, but at later times these annihilations could lead to noticeable changes in well measured astronomical signals. Of particular interest to this work are temperature anisotropies in the CMB, which are measured with great precision by satellites such as Planck, as discussed previously in 2.2.3. The CMB was imprinted on the sky around red shift $z \sim 1000$, when free electrons and protons in the universe combined into electrically neutral hydrogen during a process confusingly known as recombination. The presence of dark matter annihilations after recombination can lead to distortions in the CMB by injecting energy in the cosmic medium, which could then reionize this hydrogen [118, 119, 120].

In light of this, a light dark matter scenario must be built in a manner that does not create large energy injections at late times. For a thermal relic, this largely means suppressing the annihilation rate after freeze-out. We will choose the spins of our dark matter candidate and mediator such that annihilation proceeds through a velocity suppressed p-wave process[2]. As dark matter is expected to possess a speed in the late universe several orders of magnitude lower than it did at freeze-out, this could be expected to dramatically decrease its annihilation rate.

3.2 Kinetic Mixing

The interaction term which links the Standard Model and this scenario is chosen such that it is gauge invariant, and we charge the hidden sector under a U(1)′ gauge group. The gauge boson, labelled the V, will serve as a vector mediator with the interaction

[1] A model which predicts the overproduction of dark matter predicts a larger dark matter density than is observed.

[2] This is by no means the only option. One could also posit an asymmetric dark matter theory, where after annihilation the number density of dark matter is far higher than that of its anti-particle, in a manner very analogous (and perhaps connected) with the baryon asymmetry observed in baryonic matter [121]

term

$$\mathcal{L}_{\text{int}} = \frac{\epsilon}{2} V_{\mu\nu} B^{\mu\nu}, \tag{3.4}$$

where ϵ is the mixing strength, and $V_{\mu\nu}$ and $B^{\mu\nu}$ are the U(1)$'$ and hypercharge field strengths, respectively.

For $\epsilon \ll 1$ and before U' symmetry breaking, the Lagrangian takes the form

$$\mathcal{L}_{V,\chi} = -\frac{1}{4} V_{\mu\nu}^2 - \frac{\epsilon}{2} V_{\mu\nu} B^{\mu\nu} + |D_\mu \phi|^2 - \mathrm{U}(\phi\phi^*) + |D_\mu \chi|^2 - m_\chi^2 |\chi|^2, \tag{3.5}$$

where χ is a scalar dark matter candidate with charge e' under the hidden $U(1)'$ gauge group, m_χ is the mass of the χ, and the U(1)$'$ covariant derivative is defined as $D_\mu = \partial_\mu + ie'V_\mu$. The $U(1)'$ symmetry is spontaneously broken at low energies by the Higgs$'$ ϕ, which provides a mass term for the V, the U(1)$'$ gauge boson. The mediator interacts with Standard Model states charged under U(1) hypercharge through kinetic mixing with the vector portal, $B^{\mu\nu}$. Note that due to its coupling to hypercharge, the V will mix with the Z boson in addition to the photon, but the suppression of most processes due to the mass of the Z will render the mixing too weak to have a noticeable effect at the energy scales much smaller than the mass of the Z (this would be very different at the energy scales reached by an experiment like the LHC). We will therefore only consider its coupling to photons, and rescale the mixing factor ϵ after U' symmetry breaking to reflect only the mixing strength between the V and the photon

$$\epsilon \cos(\theta_W) \to \epsilon, \tag{3.6}$$

where θ_W is the weak mixing angle. After symmetry breaking, the Lagrangian is written as

$$\mathcal{L}_{V,\chi} = -\frac{1}{4} V_{\mu\nu}^2 + \frac{1}{2} m_V^2 V_\mu^2 + \epsilon V_\nu \partial_\mu F^{\mu\nu} + |D_\mu \chi|^2 - m_\chi^2 |\chi|^2 + \mathcal{L}_{h'}, \tag{3.7}$$

where m_V is the mass of the V boson.

To summarize, the kinetic mixing scenario possesses four parameters: the kinetic mixing strength ϵ, the gauge coupling e' (normally expressed in the form $\alpha' = \frac{(e')^2}{4\pi}$), and the two masses m_V and m_χ. We briefly outline some limits on the model parameter space. α' cannot be larger than 4π without the scenario becoming non-perturbative, though as we have never considered α' larger than 1 this is not a significant issue. For values of m_χ >500 MeV, the scenario will begin to run into significant constraints from direct detection experiments, as the dark matter candidate will pos-

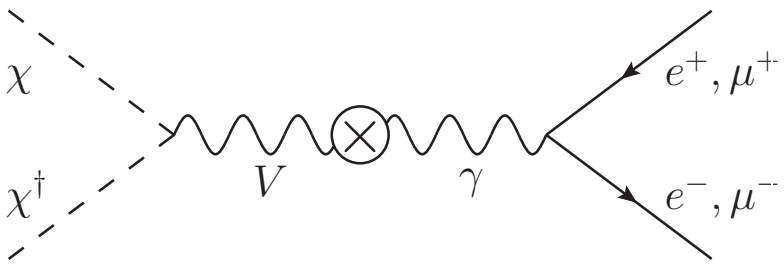

Figure 3.3: Primary diagram contributing to annihilation of dark matter into SM particles for the kinetic mixing scenario.

sess sufficient momentum produce detectable nucleon recoils in nucleon dark matter scattering, while $m_\chi <$ few MeV may run into constraints from Big Bang Nucleosynthesis. Finally, if $m_V < 2m_\chi$, the V will decay to SM particles (visible decays) rather than to hidden sector particles (invisible decays), which introduces constraints that normally apply to heavy photon models.

As we are interested in thermal relic dark matter, it is important to know the annihilation rate of a $\chi\chi^\dagger$ pairs into Standard Model particles in the early universe (see fig 3.3). The annihilation rate can be written as

$$\langle \sigma_{\chi\chi^\dagger \to \mathrm{SM}} v \rangle = \langle \sigma_{\chi\chi^\dagger \to e^+e^-} v \rangle + \langle \sigma_{\chi\chi^\dagger \to \mu^+\mu^-} v \rangle (1 + R(s)) \tag{3.8}$$

with

$$\langle \sigma_{\chi\chi^\dagger \to l^+l^-} v \rangle = \frac{8\pi}{3} \alpha' \alpha \epsilon^2 \frac{(2E_\chi^2 + m_l^2)\langle v^2 \rangle \sqrt{1 - \frac{m_l^2}{E_\chi^2}}}{(4E_\chi^2 - m_V^2)^2}, \tag{3.9}$$

where $\langle v \rangle = \beta \approx 0.3$ is the speed of the dark matter at freeze out, $E_\chi \sim m_\chi$ is the dark matter energy, m_l is the lepton mass, the angle brackets signify averaging over the thermal distribution and $R(s)$ is the R-ratio[68][3],

$$R(s) = \frac{\sigma(e^+e^- \to \gamma^* \to \text{hadrons})}{\sigma(e^+e^- \to \gamma^* \to \mu^+\mu^-)}. \tag{3.10}$$

The $\langle v^2 \rangle$ dependence in the annihilation rate reminds us that this is a p-wave annihilation process. The annihilation rate is plotted for two different values of m_V in figure 3.4. It should be noted that this equation only holds for $m_\chi < m_V$. In the other regime the annihilation channel $\chi\chi^\dagger \to VV$ is available, and should be dominant for

[3]We use the 2012 R-Ratio supplied by the PDG: http://pdg.lbl.gov/2012/hadronic-xsections/rpp2012-hadronicrpp_page1001.dat

the values of ϵ and α' considered in this work. This would be solidly in the visible V regime, where the V would be expected to decay into visible SM particles rather than invisible hidden sector states.

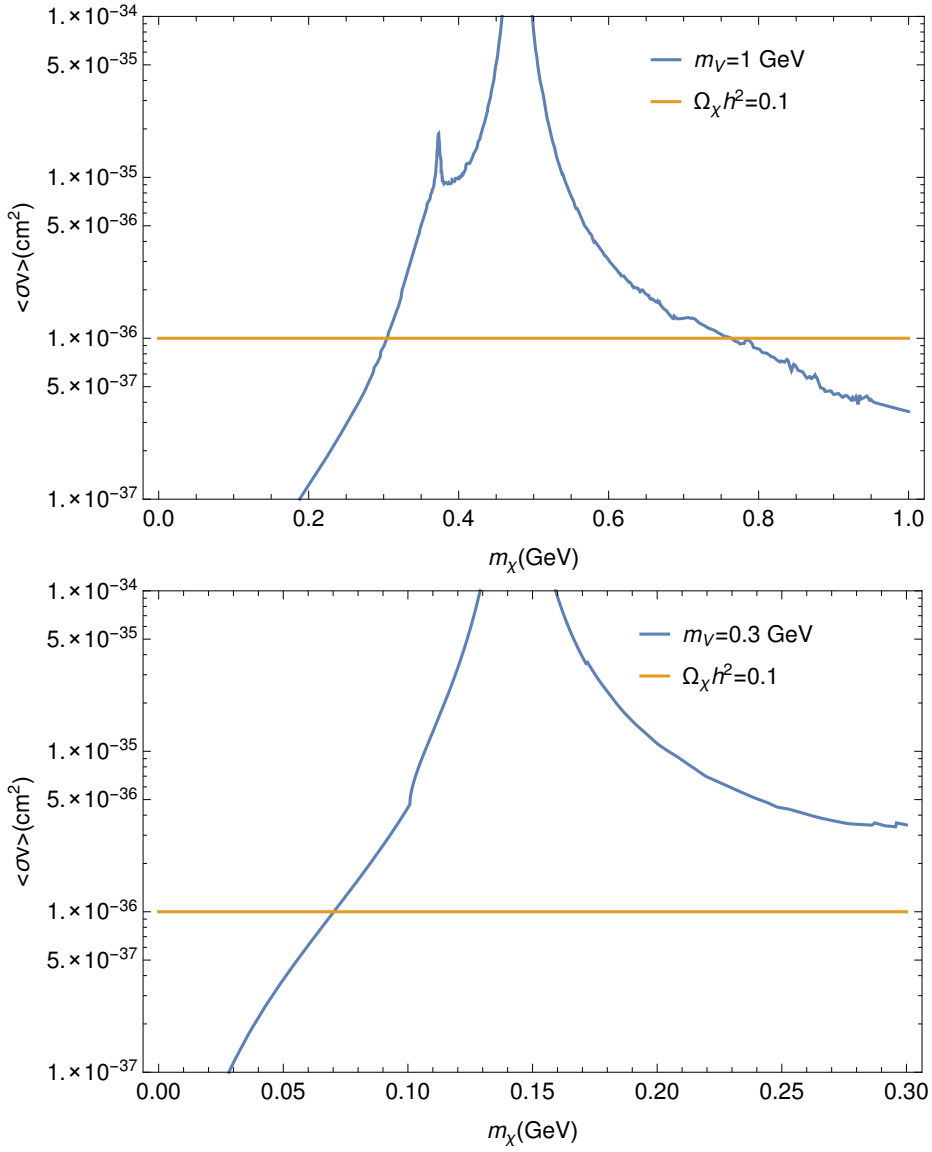

Figure 3.4: The annihilation rate $\langle \sigma_{\chi\chi^\dagger \to \mathrm{SM}} v \rangle_{\mathrm{f.o.}}$ for $\kappa = 10^{-3}$ and $\alpha' = 0.1$. Note that decreasing kappa moves the blue lines downward at a quadratic rate, and decreasing α' at a linear rate. Also plotted is $\langle \sigma v \rangle = 10^{-36}\,\mathrm{cm}^2$, which approximately reproduces the observed dark matter energy density in the universe $\Omega_\chi h^2 = 0.1$. In order to not overclose the universe, the annihilation rate should be above the $\Omega_\chi h^2 = 0.1$ line. The large peak slightly below $m_V = 2m_\chi$ is due to the dark matter annihilating into an on-shell V. Most of the other structure comes from the R-ratio.

It will also be useful to calculate the width of the V, and so we record both the

invisible and visible components of the width below

$$\begin{aligned}
\Gamma_{V\to\chi\chi^\dagger} &= \frac{\alpha'(m_V^2-4m_\chi^2)}{6m_V^2}\sqrt{\frac{m_V^2}{4}-m_\chi^2}\times H[m_V-2m_\chi],\\
\Gamma_{V\to l^+l^-} &= \frac{4\epsilon^2}{6m_V^2}\alpha_{\rm EM}(2m_l^2+m_V^2)\sqrt{m_V^2/4-m_e^2}\times H[m_V-2m_l], \quad l=e,\mu\\
\Gamma_{V\to\text{hadrons}} &= \Gamma_{V\to\mu^+\mu^-}\times R(s=m_V^2),
\end{aligned} \tag{3.11}$$

where H is the Heaviside function,

$$H[x]=\begin{cases}0 & x<0,\\ 1 & x\geq 0.\end{cases} \tag{3.12}$$

All visible decay channels are suppressed by a factor of ϵ^2 and $\alpha_{\rm EM}=\frac{1}{137}$, while the invisible channel is only suppressed by a factor of α'. The V preferentially decays to a $\chi\bar{\chi}$ pair for most of the parameter space of interest, as we will find that not only do other constraints on the model become stronger when the V decays visibly, but the sensitivity of our experimental probes of interest weakens by a factor of $\sim\alpha'$. We will still consider off-shell production, if only to show the fall in sensitivity.

3.2.1 Existing Constraints

In addition to the constraints and concerns which motivated much of our model building, there are a number of important experimental results which disfavour or entirely exclude parts of the hidden sector kinetic mixing parameters space. These constraints will be shown using plots of two dimensional slices of the parameter space, a technique that will later be used to compare the sensitivity of fixed target neutrino experiments and the existing constraints.

- *E137* - E137 was 20 GeV electron beam dump experiment carried out at the Stanford Linear Accelerator Laboratory (SLAC) from 1980-1982 [122]. A recent reexamination of the experiment's results considered the production of V bosons via bremsstrahlung off of the electron beam. The subsequent dark matter beam could be detected through hadronic showering in calorimeter material. The predicted number of events under the hidden sector dark matter scenario were compared with the experiment's null result to set stringent limits on the hidden sector parameter space [40]. This technique of probing the hidden sector

parameter space through electron beam dump experiments is one of the most promising available, and modern variations are featured in several proposed experiments (see e.g. [123]).

- *LSND* - The LSND experiment is a fixed target neutrino experiment with an 800 MeV proton beam, and a detector located approximately 35 m from the target. This experiment was capable of producing low mass dark matter particles via radiative π^0 decay (this will be discussed in great detail in chapter 4), resulting in large numbers of dark matter particles intersecting their detector. The expected scattering signal from this dark matter beam was compared to the number of scattering events reported by an experimental analysis [124] of elastic neutrino electron scattering [65, 41]. This result will be discussed in more detail in chapter 6, as it demonstrates the sensitivity of fixed target proton beam experiments to hidden sector dark matter scenarios, and provides the most straightforward example of their utility in constraining the hidden sector parameter space.

- *Missing Energy at BaBar* - BaBar is an electron-positron collider which plays a role in the study of B-physics via the production of heavy b-quark states such as the various Υ resonances. In a hidden sector dark matter scenario (or a hidden/heavy photon model), we would expect $e^+e^- \to \gamma V$ to occur some percentage of the time for sufficiently light mediators, resulting in a distinct bump in the monophoton spectrum. Limits were placed on the scenario parameter space by performing a bump hunt on BaBar data. Despite the limited data available for this analysis, very strong constraints are placed on the parameter space for almost all values of m_V for which $V \to \chi\chi^\dagger$ can occur on-shell. These limits could be dramatically improved by implementing a monophoton trigger at the planned Belle II experiment [125, 60].

- $K^+ \to \pi^+\nu\bar{\nu}$ - Here we take the invisible mode to be $K^+ \to \pi^+ V$ with an approximate branching ratio of [45]

$$\mathrm{Br}_{K\to\pi V} \approx 8 \times 10^{-5} \times \epsilon^2 \left(\frac{m_V}{100\ \mathrm{MeV}}\right)^2 \tag{3.13}$$

and compare it to limits placed by Brookhaven E949, which measured $K^+ \to \pi^+$+invisible [126]. Note that the limits weaken dramatically in the two body

decay region $K_{2\pi}$, where the background process $K^+ \to \pi^+\pi^0$ dominates over all other processes.

- $J/\Psi \to$*invisible* - A weak constraint for most values of m_V, but becomes very strong on resonance. This constraint is provided by the limit Br($J/\Psi \to$invisible)$<$ 7×10^{-4} placed by the BES collaboration [127].

- $\pi^0 \to \gamma +$*invisible* - A limit of Br$(\pi^0 \to \gamma V) < 5 \times 10^{-4}$ has been placed by the Brookhaven alternating gradient synchrotron. This imposes limits on the kinetic mixing scenario through comparison with the branching ratio (4.1) [128].

- Δm_Z *and EW fit* - The mixing of the V with hypercharge impacts the photon and the Z after electroweak symmetry breaking. This shift in the Z mass and electroweak precision fits places a weak and nearly constant constraint on the parameter space until $m_V \sim m_Z$ [129].

- CDF constraints on Monojets - Limits from searches on $pp \to$ jet+missing energy [130, 131]. This limit is largely independent of V mass.

- *Lepton* $g-2$ - Loop corrections to l-l-γ vertices involving V bosons can lead to measurable shifts in the values of the anomalous magnetic moment of the electron and muon, $a_l = \frac{g-2}{2}$. The hidden sector contributions can be calculated as [45]

$$a_l^V = \frac{\alpha}{2\pi}\kappa^2 \int_0^1 dz \frac{2m_l^2 z(1-z)^2}{m_l^2(1-z)^2 + m_V^2 z}. \tag{3.14}$$

  Electron $g-2$ is well measured and in good agreement with theory, so any significant deviation from this value excludes portions of the scenario parameter space. Muon $g-2$ is another story, as experimental measurements and theoretical calculations differ by approximately 3.4 standard deviations [132, 133]. The hidden sector scenario can actually improve the fit between theory and experiment, as shown in the blue band of the parameter space (see Fig. 3.5) where the agreement is improved to better than 3σ. We exclude parameter space which increases the disagreement to more than 5σ [134, 135, 136].

- *Direct Detection* - As a WIMP dark matter model that couples to nucleons, the hidden sector scenario is constrained by the conventional direct dark matter detection experiments previously discussed, with spin-independent scattering providing the best limits. The limits from direct detection experiments become

very weak at low masses due to the difficulty of detecting the recoil from low mass dark matter, but improve dramatically for masses about 500 MeV. See figure 3.1 for a selection of the best limits for low mass dark matter, and section 2.4.1 for a discussion of direct detection experiments. Electron scattering can also be used to constrain the kinetic mixing scenario, but the constraints imposed are weaker than those from SI-nucleon scattering [137, 138].

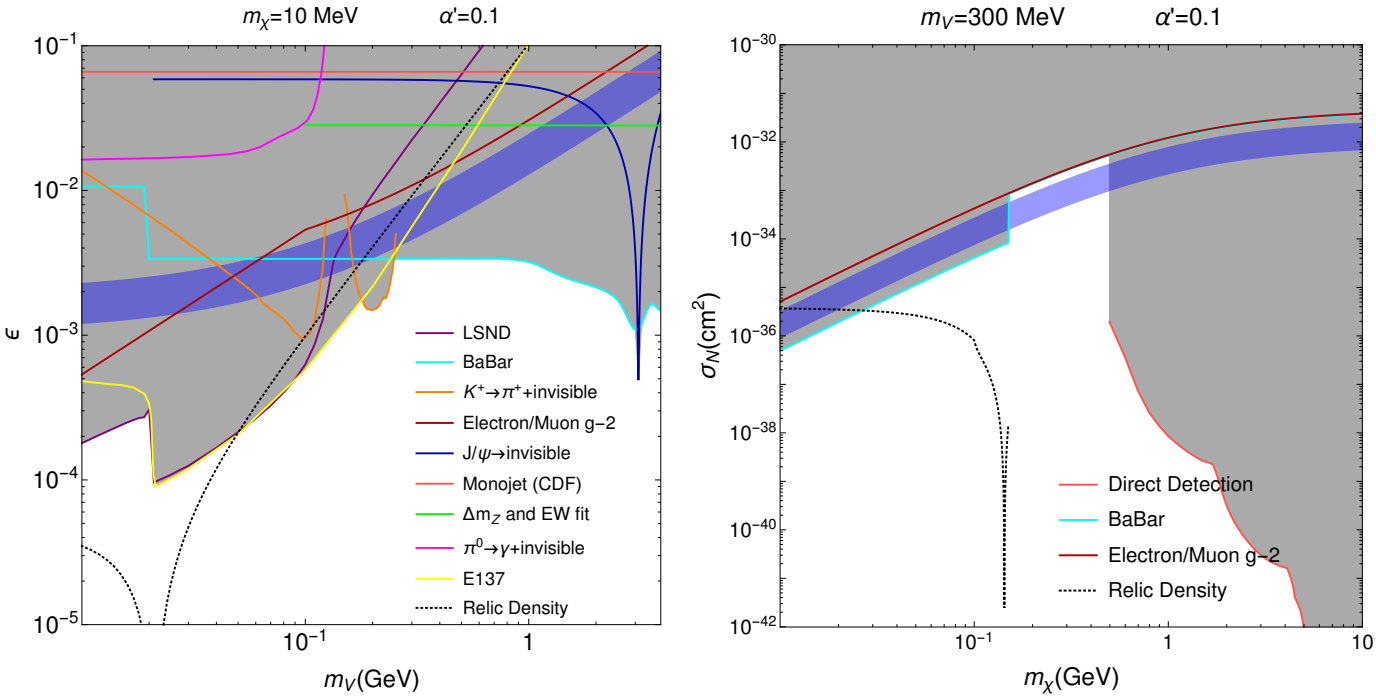

Figure 3.5: Limits on the kinetic mixing hidden sector parameter space, where regions shaded in grey are excluded. Note that while many of the limits that specifically test hidden sector dark matter weaken when the $m_V < 2m_\chi$, and thus the V can no longer decay invisibly, the limits on dark or heavy photons, which rely on the visible decay of the V to SM particles, apply and completely exclude much of this region of the parameter space (see Fig. 3.6). These figures were generated by compiling all of the limits discussed in this section. Note that many of these limits require data from the experimental papers cited, or make use of equations in Chapter 4. Earlier versions of this plot have appeared in [14] and [15].

We summarize the constraints on the parameter space of the hidden sector scenario with two 2-dimensional slices of the parameter space shown in figure 3.5. We choose some reasonably large value for the U(1)$'$ fine structure constant by setting $\alpha' = 0.1$, though this can be varied quite widely so long as the theory remains perturbative. The left-hand plot provides an analogue of the dark force or heavy photon parameter

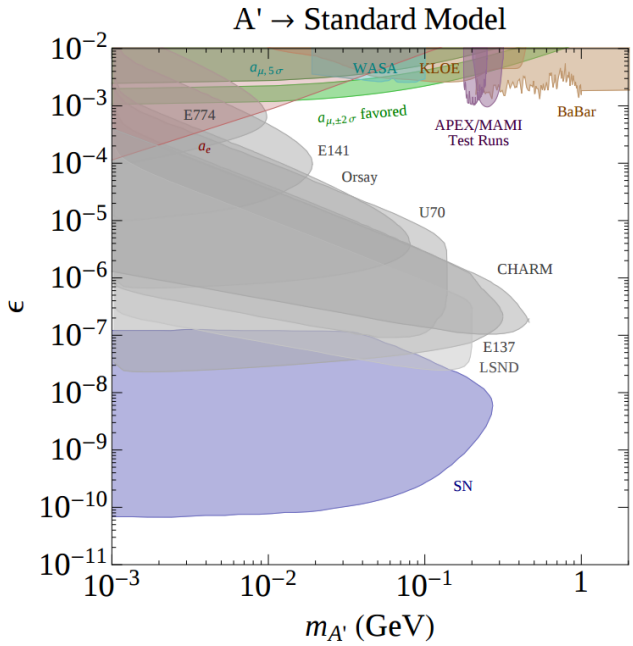

Figure 3.6: An example of the heavy photon/dark force parameter space in 2013, where the dark photon is called A'. All shaded regions are excluded by experiment. Many of the constraints are heavily dependent on Br($V \rightarrow$SM)= $\mathcal{O}(1)$. Reproduced with permission from R. Essig et al., "Working Group Report: New Light Weakly Coupled Particles", in the Proceedings of the APS DPF Community Summer Study (Snowmass 2013), http://www.slac.stanford.edu/econf/C1307292/, arXiv:1311.0029 [hep-ph], Copyright 2013 [16].

space (see Fig. 3.6 for a comparison plot), where some interesting value of m_χ is chosen, and the limits in ϵ are shown over a range of m_V values. A number of the dark force limits also appear on this plot, but are heavily suppressed due to the large branching ratio of $V \rightarrow$invisible.

On the right-hand side, we show a plot analogous to the direct detection limits imposed by direct dark matter detection searches, such as fig 2.4. Constraints are normally dependent on the kinetic mixing strength ϵ, but can be translated into limits on the dark matter nucleon scattering cross section through

$$\sigma_N \sim 16\pi \left(\frac{Z}{A}\right)^2 \alpha\alpha'\epsilon^2 \frac{\mu_{\chi,N}^2}{m_V^4}, \tag{3.15}$$

where $\frac{Z}{A} = \frac{1}{2}$ and $\mu_{\chi,N}$ is the reduced mass

$$\mu_{\chi,N} = \frac{m_\chi m_N}{m_\chi + m_N}. \tag{3.16}$$

Many of the constraints, at least those that do not come from fixed target experiments, vary only weakly with m_χ, and most of the structure of the constraint lines reflects the evolution of (3.15) with m_V.

3.3 Leptophobic

The kinetic mixing scenario considers coupling a hidden sector to the Standard Model through photons, but this is only one possible coupling. In order to cover a broader range of possible couplings to which proton colliders possess unexploited sensitivity, we also examine the possibility of hidden sector dark matter whose interactions with the Standard Model are mediated by a vector boson which dominantly couples to quarks. We do not wish to introduce any tree level flavour changing neutral current interactions, and the simplest way of avoiding this complication is for the V's quark couplings to be generation independent. In order to allow renormalizable Yukawa couplings of the quarks to the SM Higgs, the V should couple to both right- and left-handed quarks equally. Putting these pieces together, our vector mediator will be a gauge boson of the local baryon number $\mathrm{U}(1)_B$, which will be referred to as V_B [139, 140, 141, 142, 143, 144, 145, 146, 147, 148, 149, 150, 151, 64].

A local $\mathrm{U}(1)_B$ symmetry introduces gauge anomalies into the theory, and therefore what we will actually be formulating is a low energy effective theory with some ultraviolet cutoff Λ_{UV}[152]. Either at or above this cutoff scale some new states must be introduced for the theory to remain consistent. A number of strategies for the UV completion of this coupling are explored in the previously mentioned literature, some of which could be probed by high energy collider data. However, we are mainly interested in the phenomenology of the scenario at energies of at most a few GeV, we will not overly concern ourselves with their exact implementation and focus on the low energy effective theory.

The leptophobic Lagrangian is written

$$\mathcal{L}_{V,\chi} = |D_\mu \chi|^2 - m_\chi^2 |\chi|^2 - \frac{1}{4}(V_B^{\mu\nu})^2 + \frac{1}{2} m_V^2 (V_B^\mu)^2 - \frac{\epsilon}{2} V_B^{\mu\nu} F_{\mu\nu} + g_B V_{B,\mu} J_B^\mu + ..., \tag{3.17}$$

where $D^\mu = \partial^\mu - ig_B q_B V_B^\mu$, g_B is the U(1)$_B$ charge of the χ, and $J_B^\mu = \frac{1}{3}\sum_i \bar{q}_i \gamma^\mu q_i$ is the baryon current. It should be noted that this Lagrangian includes the kinetic mixing interaction, allowing it to emulate all of the phenomenology of the previous section. In a sense, this Lagrangian generalizes the previously discussed kinetic mixing hidden sector scenario. It is possible that there exists some interesting phenomenology that mixes the two scenarios, but for most values of the scenario parameters either the baryonic coupling or the kinetic mixing will dominate the phenomenology. The leptophobic scenario is created by setting the kinetic mixing $\epsilon \to 0$, and it is this parameter space that we will test.

An interesting point to note is that even when we set $\epsilon \to 0$, a non-zero mixing can be generated through loop diagrams. The generated mixing is expected to be $\epsilon_B \approx \frac{g_B e}{16\pi^2}$, which in most cases will have a vanishingly small effect on the phenomenology of the scenario. This does become critically important when considering parts of the parameter space in which the V_B cannot decay invisibly, $m_V < 2m_\chi$, as it opens up the $V_B \to e^+e^-$ decay channel, preventing the V_B from being long lived.

3.3.1 Existing Constraints

Though far harder to constrain, the leptophobic hidden sector scenario is not immune to experimental probes of its parameter space.

- *Angular Dependence in Neutron Scattering* - A very low mass V_B makes long-range contributions to nucleon interactions. KeV neutron-Pb scattering data imposes
$$\alpha_B < 3.4 \times 10^{-11} \left(\frac{m_V}{\text{MeV}}\right)^4$$
for $m_V > 1$ MeV [153, 151].

- $\pi^0 \to \gamma + \textit{invisible}$ - This limit is similar to the kinetic mixing limit, but we instead compare the invisible decay width to that of $\pi^0 \to \gamma V_B$ 4.5.

- $K^+ \to \pi^+ \nu\bar{\nu}$ - The handling of this constraint is a bit more uncertain than it was in the kinetic mixing case, as there are both short- and long-distance contributions. However, while the loop-induced $K^+ - \pi^+ - \gamma^*$ vertex can be inferred from the measured 3-body hadronic kaon decays using Chiral Perturbation Theory, pseudosclar mesons are uncharged under $U(1)_B$ and it is natural to anticipate

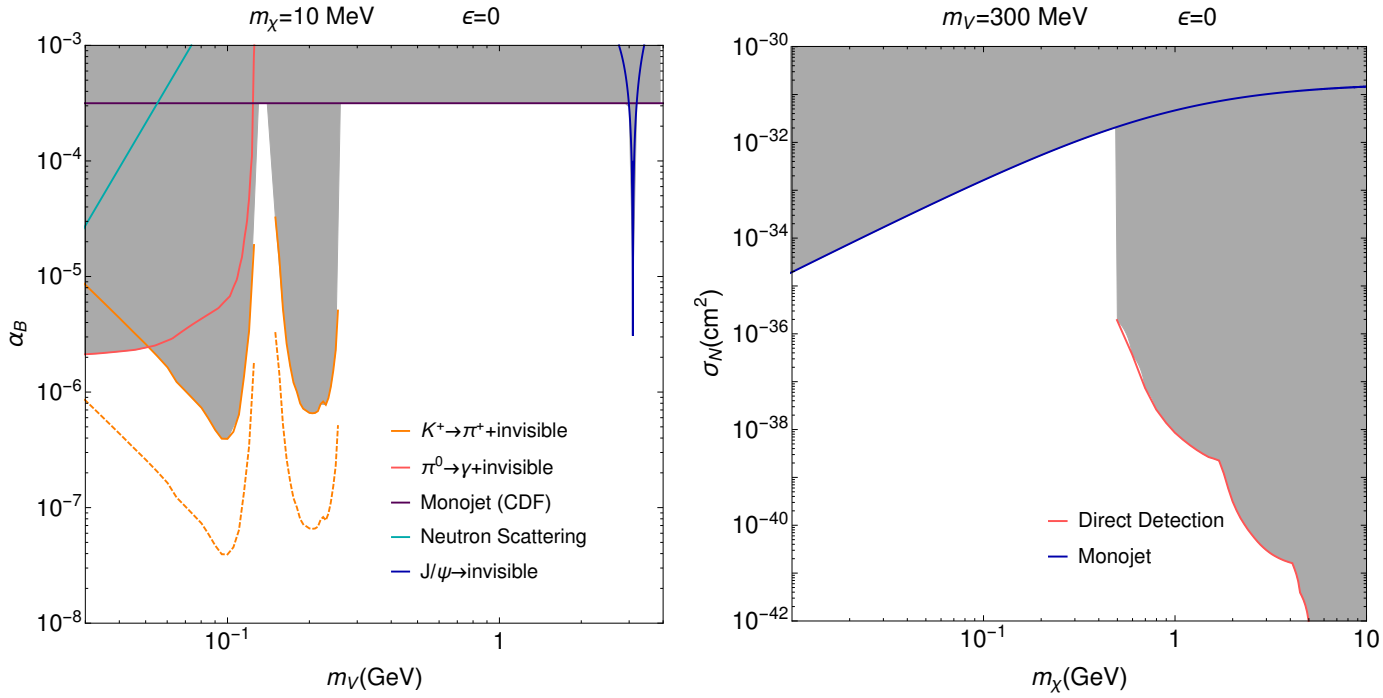

Figure 3.7: Limits on the leptophobic hidden sector parameter space. Grey shaded regions are excluded by experimental searches. Note that the limit from $K^+ \to \pi^+$invisible is shown under two possible assumptions on the value of the IR cutoff, $\Lambda_{\rm IR} = 4\pi f_\pi$ in solid orange and $\Lambda_{\rm IR} = m_\rho$ in dashed orange. An earlier version of these constraints appeared in [15].

that the long-distance contribution is suppressed. The short-distance contribution is dominated by the GIM-suppressed V_B-penguin with c- and u-quark loops. Retaining only the leading logarithm,

$$\mathcal{L}_{\rm pen} \simeq V_B^\mu \bar{s}\gamma_\mu d \times \sin 2\theta_c \frac{G_F}{\sqrt{2}} \frac{g_B}{24\pi^2} \log\left[\frac{m_c^2}{m_u^2(\to \Lambda_{IR}^2)}\right] + \text{h.c.}, \tag{3.18}$$

where θ_c is the Cabibbo angle, and m_u in the logarithm needs to be replaced with the hadronic Infrared (IR) cutoff Λ_{IR}, with e.g. $m_\rho \leq \Lambda_{IR} \leq 4\pi f_\pi$. Since we expect the long-distance contribution to be suppressed, the sensitivity to this cutoff leads to considerable uncertainty in the result. Allowing for both the baryonic and kinetic mixing portal couplings, the amplitude takes the form,

$$\mathcal{M}_{K\to\pi V_B} = \frac{m_V^2}{(4\pi)^2 m_K^2}(k+p)^\mu \epsilon_\mu^V \times (g_B W_B(m_V^2) - e\epsilon W_\kappa(m_V^2)), \tag{3.19}$$

where k and p are the kaon and pion momenta, ϵ^V is the polarization vector of V_B, and $W_\epsilon^2(m_V^2) \sim 3 \times 10^{-12}$ [45], $W_B^2(m_V^2) \sim 4 \times 10^{-13}$ in an approximation where $m_V^2 \ll m_K^2$ and the logarithm is cut off in the infrared at the scale $\Lambda \sim m_\rho$ [139, 46, 15].

- *Direct Detection* - As with the kinetic mixing scenario, the leptophobic scenario is constrained by direct detection searches through its coupling to nucleons.

- *CDF constraints on Monojets* - These constraints are similar to those for the kinetic mixing scenario, and provide the best limit over much of the higher mass scenario parameter space.

As with the kinetic mixing parameter space, we show two slices of the parameter space (see Fig. 3.7) in order to summarize the constraints, holding either m_χ or m_V constant.

$$\sigma_N \sim 16\pi\alpha_B^2\epsilon^2\frac{\mu_{\chi,N}^2}{m_V^4}, \tag{3.20}$$

where the factor of Z/A found in (3.15) has been replaced with 1 as the leptophobic scenario couples equally to neutrons and protons in the low energy limit, and $\mu_{\chi,N}$ is the reduced mass defined in (3.16). In contrast to the hidden sector scenario, where α' was fixed, we now fix $\epsilon = 0$, and allow α_B to vary.

3.4 Solar Trapping

An additional constraint on hidden sector dark matter not included in the previous discussions on model constraints, but mentioned in section 2.4, is a possible indirect signal from dark matter annihilation in the sun. It is possible that dark matter could be trapped in the sun by scattering off nuclei to speeds below the escape velocity of the sun. This dark matter would then collect in and around the center of the sun at a far higher density than would be found elsewhere in the solar system, though this statement is less accurate for dark matter masses below a GeV. The trapped dark matter would then annihilate into baryons, mesons and leptons, whose decays to neutrinos could produce a visible signal in earth-based cosmic and solar neutrino detectors. In this section, we will lay out some of the steps for performing this calculation, following the treatment of Busoni *et. al.* [154] and Bernal *et. al.* [155] (which are in turn based upon the original derivations by Gould [156, 157, 158]),

paying particular attention to dark matter masses below a GeV and assuming that the sun is optically thin to dark matter[4]. In this section we will only consider kinetically mixed hidden sector dark matter.

The evolution of the dark matter population trapped in the sun is governed by three competing processes: capture, evaporation, and annihilation. Capture occurs when a dark matter particle incident on the sun scatters to a speed below the escape velocity, $v_{\rm esc}(r)$, where r is the distance from the center of the sun. Evaporation is the inverse process, in which a dark matter particle trapped inside the sun scatters to velocity greater than the escape velocity of the sun, and its calculation is very similar to that of capture. Annihilation should be self-explanatory. The change in the number of dark matter particles can be written in terms of these three processes as follows,

$$\frac{dN_\chi(t)}{dt} = C_\odot - E_\odot N_\chi(t) - A_\odot N_\chi(t)^2, \tag{3.21}$$

where N_χ is the total number of dark matter particles captured by the sun, $C_\odot$, $E_\odot$, and $A_\odot$ are the capture, evaporation and annihilation coefficients, respectively. Note that $C_\odot$, $E_\odot$, and $A_\odot$ are rates, and therefore possess units of inverse time, s^{-1}. Each of these coefficients must be calculated in turn. Integrating (3.21), one finds the total number of dark matter particles trapped in the sun,

$$N(t_\odot) = \sqrt{\frac{C_\odot}{A_\odot}} \frac{\tanh(kt_\odot/\tau)}{k + \frac{1}{2}E_\odot \tau \tanh(kt_\odot/\tau)} = N_\chi \tag{3.22}$$

where $\tau \equiv 1/\sqrt{C_\odot A_\odot}$ and $k \equiv \sqrt{1 + (E_\odot \tau/2)^2}$. So long as $kt_\odot/\tau \gg 1$, the number of dark matter particles in the sun has reached its equilibrium value and the hyperbolic functions go to 1. This is expected to hold for the hidden sector dark matter scenario. The evolution of dark matter in the sun can be largely classified into either an evaporation dominated regime, where capture goes into equilibrium with evaporation, or an annihilation dominated regime, where annihilation goes into equilibrium with capture. If the regime is strongly evaporation dominated such that $E_\odot \gg N(t_\odot)A_\odot$, then a much simpler form can be adopted

$$N(t_\odot) = \frac{C_\odot}{E_\odot}\left(1 - e^{-E_\odot t_\odot}\right). \tag{3.23}$$

[4]For $\epsilon = 10^{-3}$, it appears that we should be on the very edge of an optically thick sun, but the suppression of the evaporation rate from this regime would not be large enough to affect our conclusions.

Low mass dark matter tends to be evaporation dominated, as the dark matter requires a smaller momentum transfer in a collision with a nucleus to reach the escape velocity[5] and (3.23) is expected to be sufficient.

The annihilation coefficient is defined as,

$$A_\odot \equiv \langle \sigma v_\chi \rangle_\odot \frac{\int_{\text{Sun}} n_\chi(r)^2 \mathrm{d}^3 r}{\left(\int_{\text{Sun}} n_\chi(r) \mathrm{d}^3 r\right)^2}, \tag{3.24}$$

where $\langle \sigma v_\chi \rangle_\odot$ is the thermally averaged dark matter annihilation rate and $n_\chi(r)$ is the dark matter number density at radius r. Note that this assumes that the annihilation rate is the same for dark matter at all solar radii, which may be a poor assumption for p-wave annihilation. The dark matter number density can be written as,

$$n_\chi(r) = n_0 e^{-m_\chi \phi(r)/T_\chi}, \tag{3.25}$$

where n_0 is the dark matter density at the center of the sun, $\phi(r)$ is the gravitational potential with respect to the sun's core and T_χ is the temperature of the dark matter distribution. The gravitational potential can be written as

$$\phi(r) = \int_0^r \frac{G_N M_\odot(r')}{r'^2} \mathrm{d}r', \tag{3.26}$$

where $M_\odot(r)$ is the solar mass inside of a radius r. This requires the use of a density profile from a solar model, and we have chosen to use AGSS09[6] [159]. T_χ is set equal to the solar temperature at the mean DM orbit radius,

$$T_\chi = T_\odot(\langle r_\chi \rangle). \tag{3.27}$$

The mean dark matter orbit is calculated by the following expression,

$$\langle r_\chi(m_\chi) \rangle = \frac{\int_{\text{Sun}} r n_\chi(r) \mathrm{d}^3 r}{\int_{\text{Sun}} n_\chi(r) \mathrm{d}^3 r}. \tag{3.28}$$

It is evident that these definitions are circular, as n_χ is dependent on T_χ, and is itself

[5] Evaporation is inconsequential for heavy dark matter for much the same reason, as it rarely gains enough energy from collisions to reach the escape velocity. Additionally, it is heavily concentrated in the center of the sun, where the escape velocity is larger.

[6] See http://www.mpa-garching.mpg.de/~aldos/SSM/AGSS09/model_agss09.dat for a table of solar properties generated by the AGSS09 solar model over a range of solar radii.

used in the evaluation of T_χ. For most m_χ this can be solved iteratively. If we pick some arbitrary value for $\langle r_\chi(m_\chi)\rangle$, use it to find T_χ, and then use that T_χ to find a new value for $\langle r_\chi(m_\chi)\rangle$, the values will rapidly converge on the physical solution. For $m_\chi \in [0.5, 2]$ GeV, the physical solution becomes unstable, and this process becomes slow or fails entirely. It is slower, but safer, to search the parameter space of $\langle r_\chi(m_\chi)\rangle$ for a value that, when iterated on as above, returns a value of $\langle r_\chi(m_\chi)\rangle$ that is very close to the starting mean radius.

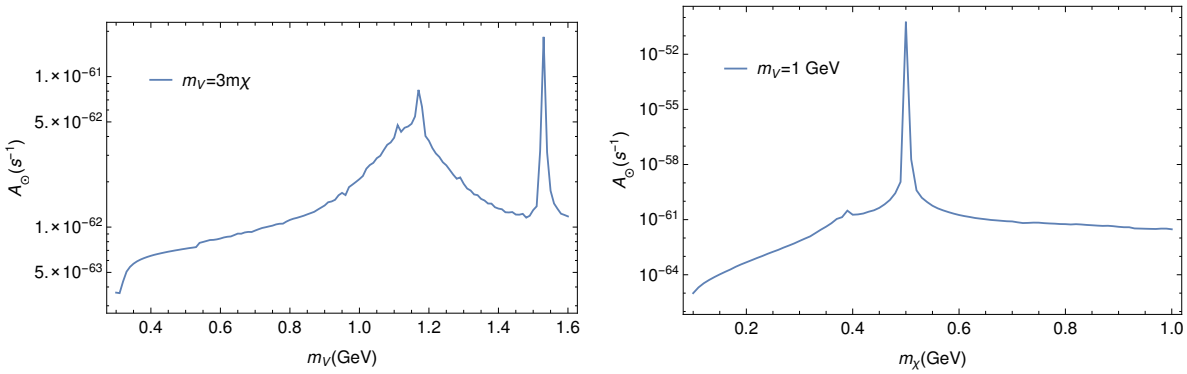

Figure 3.8: The annihilation coefficient for hidden sector kinetically mixed dark matter with $\epsilon = 10^{-3}$ and $\alpha' = 0.1$. The left-hand plot scales m_χ with m_V, maintaining a constant ratio between the masses, while the right-hand plot fixed m_V and changes m_χ. These values of the annihilation coefficient are incredibly small, and would require very dark matter numbers in the sun to produce a detectable dark matter annihilation signal. The one possible exception when $m_V = 2m_\chi$, as the annihilation rate spikes dramatically, though the dark matter is still strongly evaporation dominated.

The capture coefficient can be written as

$$C_\odot = \sum_i \int_{\text{Sun}} \mathrm{d}^3 r \int_0^\infty \mathrm{d}u \frac{f_{v_\odot}(u)}{u} w(r) \int_0^{v_{\text{esc}}(r)} \mathrm{d}v R_i^-(w \to v) |F_i(w, v)|^2 \tag{3.29}$$

where $f_{v_\odot}(u)$ is the velocity distribution of the dark matter halo in the sun's rest frame (averaged over angles), $w(r) = \sqrt{v_{\text{esc}}(r)^2 + u^2}$ is the speed of free dark matter in the sun and u is the speed of free dark matter at infinity. $R_i^-(w \to v)$ is the probability of a DM particle scattering off a Maxwell-Boltzmann distribution of nuclei i from a larger speed w to a smaller speed v per unit time and $F_i(w, v)$ is a form factor that suppresses dark matter scattering when there is a large mismatch between m_χ and m_{N_i}, see Busoni [154] or Gould [156, 158] for more explicit definitions of these quantities. The sum is over the different species of nuclei found in the sun, as provided

by the AGSS09 solar model.

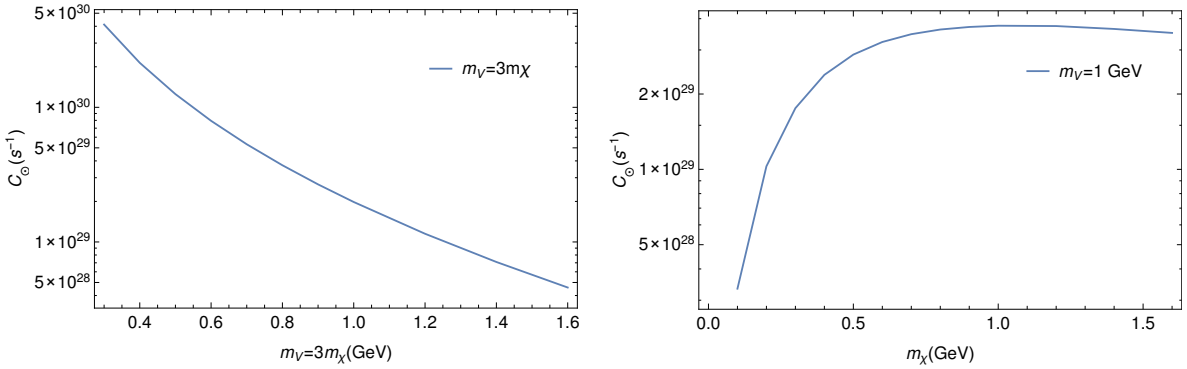

Figure 3.9: The capture coefficient for hidden sector kinetically mixed dark matter with $\epsilon = 10^{-3}$ and $\alpha' = 0.1$.

The evaporation coefficient is very similar in form to $C_\odot$,

$$E_\odot = \sum_i \int_{\text{Sun}} \mathrm{d}^3 r \int_0^\infty \mathrm{d}w f_\odot(w, r) \int_{v_{\text{esc}}(r)}^\infty \mathrm{d}v R_i^+(w \to v), \tag{3.30}$$

where $f_\odot(w, r)$ is the velocity distribution of WIMPs trapped in the sun, and $R_i^+(w \to v)$ is the probability of a DM particle scattering off a Maxwell-Boltzmann distribution of nuclei i from a smaller speed w to a larger speed v per unit time. $f_\odot(w, r)$ should be a truncated velocity distribution, though exactly where to cut off the distribution is less clear. At the very least, it should be truncated at $v_{\text{esc}}(r)$, though Gould argues for one at or below 80% of $v_{\text{esc}}(r)$, depending on the exact location in the sun [157].

With all three coefficients in hand, the number of DM particles trapped in the sun can be calculated using (3.22), and the DM annihilation rate can be expressed as

$$\Gamma_A = \frac{1}{2} A_\odot N_\chi^2. \tag{3.31}$$

We would be concerned primarily with dark matter annihilation into charged pions and charged muons, though perhaps heavier charged mesons will also provide signal of some interest. Charged pions and muons will come to a stop in the sun before decaying, producing low energy neutrinos of a few tens of MeV, the signal of which could be observed by underground neutrino observatories such as Super Kamiokande. This has already been discussed in some detail by Bernal *et. al.*, though for much heavier dark matter [155]. It should be noted that the regime of interest for this dark matter scenario is strongly evaporation dominated and the dark matter will be spread

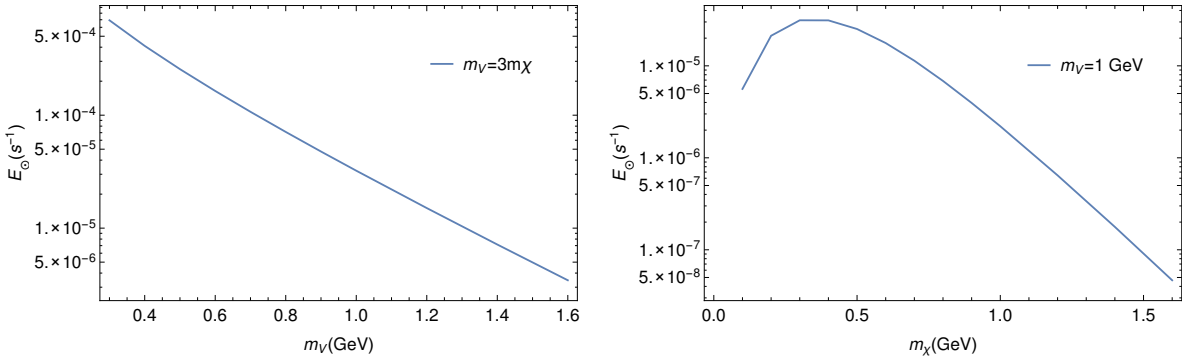

Figure 3.10: The evaporation coefficient for hidden sector kinetically mixed dark matter with $\epsilon = 10^{-3}$ and $\alpha' = 0.1$. The inverse of the evaporation coefficient indicates the time scale over which the number of dark matter particles will reach equilibrium. For the parameters shown in these plots, this ranges from as little as a few hours to as long as a year.

throughout the sun rather than collecting in the center as heavier dark matter would.

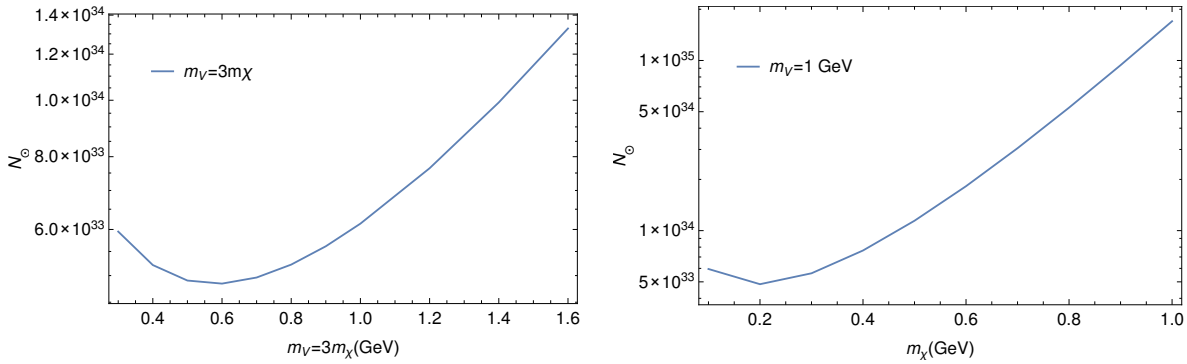

Figure 3.11: The equilibrium number of trapped dark matter particles in the sun for hidden sector kinetically mixed dark matter with $\epsilon = 10^{-3}$ and $\alpha' = 0.1$. This generally increases with mass as the evaporation rate drops far more rapidly than the capture rate.

We show the calculated annihilation (Fig. 3.8), capture (Fig. 3.9), and evaporation coefficients (Fig. 3.10) for kinetically mixed hidden sector dark matter with $\epsilon = 10^{-3}$ and $\alpha' = 0.1$, along with the equilibrium number of trapped dark matter particles in the sun (Fig. 3.11). All of the coefficients scale as κ^2, so decreasing κ would keep $N_\odot$ constant while increasing the time required for the trapped dark matter to reach its equilibrium value. The captions of each set of figures provide some observations on the calculated coefficients. The simple conclusion is that $N_\odot$ is so strongly evaporation dominated that the annihilation signal would be far too weak to

be observed by any earthbound experiment. Even were every annihilated dark matter particle to produce a neutrino, with $m_V = 2m_\chi$ to optimize the annihilation rate, we would still expect a neutrino flux of a few thousand dark matter produced neutrinos per square meter on Earth per year. It is therefore highly unlikely that solar trapping would provide constraints of any significance on low mass hidden sector dark matter.

3.5 Summary

In this chapter, we laid out the motivations for low mass dark matter scenarios, and described how one might build such a model. Two possible variants on the low mass dark matter scenario, kinetic mixing and leptophobic dark matter, were proposed. All the existing limits on these scenarios were discussed and overlaid on plots of the parameter space. We finished the chapter with an in-depth discussion of solar trapping of dark matter, and whether this could result in a neutrino signal on earth for the kinetically mixed hidden sector scenario. The population of trapped dark matter was calculated for the kinetic mixing scenario, and determined to be far too small to result in a detectable neutrino signal. In the next chapter, we will discuss how these hidden sector dark matter scenarios can be probed at fixed target neutrino experiments.

Chapter 4

Fixed Target Signatures

4.1 Introduction

Fixed Target Neutrino Experiments have the potential to impose some of the best constraints on hidden sector dark matter scenarios over much of their viable parameter space. These experiments impact thick targets with high intensity proton beams in order to produce large numbers of neutrinos that then propagate to one or more neutrino detectors located tens of meters to hundreds of kilometers away. It is expected that alongside these neutrinos one could also produce copious numbers of hidden sector dark matter particles.

We will calculate the distribution and production rate of dark matter particles expected from a set of the most promising dark matter production channels available to proton colliders, and the possible signal channels by which the presence of dark matter could be detected in the detector of a Fixed Target Neutrino Experiment. Separate treatments must be given to both the kinetic mixing and leptophobic scenarios, though several channels are only considered for the former scenario as they are suppressed in the latter.

4.2 Production Modes

Within the hidden sector scenarios described in the previous chapter, there are a number of processes which could result in the production of the dark matter for sufficiently small values of m_V and m_χ. We will calculate the contribution to a dark matter beam of the dominant processes in each mass range for m_V below a few GeV.

Many of these processes are not significant contributors to the neutrino signal or background at fixed target neutrino experiments and have not been studied in any great detail as a result. By necessity, these calculations contain several approximations and estimates, and we will emphasize the main sources of uncertainty in our production estimates.

We will consider production through:

- *Pseudoscalar meson decays*, which are expected to make large contributions to the dark matter production rate due to the ubiquitous production of pions and η's at fixed target experiments of all energies and their large radiative branching fractions.
- π^- *capture resulting in photon emission*, an important production channel at the low energies of fixed target experiments that should produce dark matter with a largely isotropic angular distribution.
- *Proton Bremsstrahlung*, highly competitive at V masses above that of the η, and likely to produce dark matter with a very small angular spread relative to the beam direction.
- *Partonic V production*, most important at masses above that of the ρ.
- *Vector mixing*, now largely superseded by proton bremsstrahlung, this channel provided initial estimates of the $X^* \to V \to \chi\bar{\chi}$ for $X = \rho, \omega, \phi$.

The baryonic state $\Delta(1232)$ was also considered as a possible contributor to a dark matter beam, as its decays are one of the primary sources of pions at fixed target neutrino experiments, and should therefore be produced at a comparable rate. Its branching ratio to a single photon, while small, is not so small as to render it completely insensitive to the hidden sector scenario. We chose not to pursue this avenue of inquiry primarily because the η decay mode could access a significantly larger range of V and χ masses than the $\Delta(1232)$ and should decay to dark matter with greater frequency.

4.2.1 Pseudoscalar Meson Decay

Kinetic Mixing

The decays of pseudoscalar mesons $X = \pi^0, \eta$ are the primary source of dark matter for scenarios with small m_V, that is $m_V \in [\text{few MeV}, m_X)$, where m_X is the mass

of the pseudoscalar meson. The decay $\pi^0 \to V\gamma$ proceeds through kinetic mixing between the photon and the V. Dark matter is produced through the chain:

1. $p + p/n \to Y + \pi^0, \eta$
2. $\pi^0, \eta \to V^{(*)} + \gamma$
3. $V^{(*)} \to \chi\chi^\dagger$

where Y refers to all the products of $p + p/n$ interactions that are not the mesons of interest, and $V^{(*)}$ allows for the possibiltiy of an off-shell V.

As the π^0 and η both have decay lengths of a few nanometers ($c\tau_{\pi^0} = 25.1\,\text{nm}$, $c\tau_\eta \simeq 0.2\,\text{nm}$), the first two steps of the decay chain can be expected to take place inside of the target. The decay lifetime of the V is strongly dependent on the model parameters, but should always be quite short for the parameter space of interest, where the invisible decay channel dominates. The vast majority of dark matter particles from this production mode will be produced by decays in flight.

For the on-shell case, in which $m_V < m_X$, and $m_V > 2m_\chi$, we can use the narrow width approximation to calculate a simple, if only approximate form for the branching ratio [33]:

$$\text{Br}(X \to \chi\chi^\dagger) = 2\epsilon^2 \text{Br}(X \to \gamma\gamma) \left(1 - \frac{m_V^2}{m_X^2}\right)^3 \text{Br}(V \to \chi\bar{\chi}), \tag{4.1}$$

where $\text{Br}(\pi^0 \to \gamma\gamma) = 0.988$ and $\text{Br}(\eta \to \gamma\gamma) = 0.3941$ [68].

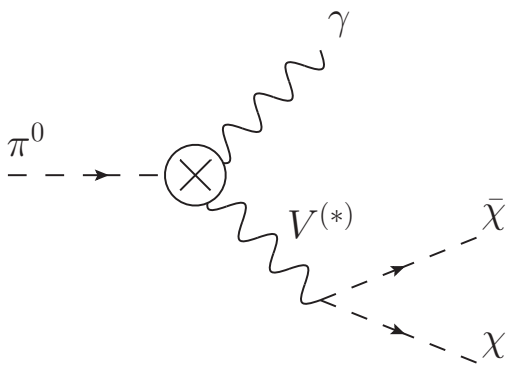

Figure 4.1: π^0 decay to $\gamma\chi\bar{\chi}$ through an off-shell V.

The expression for the branching ratio becomes more complicated when the V is produced off-shell (see Fig. 4.1), as it must be written in the form of an integral [41]

$$\mathrm{Br}(\pi^0 \to \gamma V^* \to \chi\chi^\dagger\gamma) = \frac{1}{\Gamma_{\pi^0}} \times \frac{1}{4\pi m_\pi} \int d\Pi_{\pi^0\to\gamma V} d\Pi_{V\to\chi^\dagger\chi} dq^2 |\mathcal{M}|^2, \tag{4.2}$$

where $d\Pi_{\pi^0\to\gamma V} = \sin(\theta_{\pi^0}) d\theta_{\pi^0} d\phi_{\pi^0}$ with all angles in the π^0 rest frame, $d\Pi_{V\to\chi^\dagger\chi} = \sin(\theta_V) d\theta_V d\phi_V$ with all angles defined in the V rest frame, and the amplitude is defined as

$$|\mathcal{M}|^2 = \frac{\epsilon^2 \alpha_{\mathrm{EM}}^2 \alpha'}{\pi f_\pi^2 [(s - m_V^2)^2 + m_V^2 \Gamma_V^2]} \left[(s - 4m_\chi^2)({m_{\pi^0}}^2 - s)^2 - 4s(p\cdot k_1 - p\cdot k_2)^2 \right], \tag{4.3}$$

where $q = k_1 + k_2$ is the virtual V momentum, $s = q^2$ is the off-shell mass of the V, p is the γ momentum, and k_1 and k_2 are the dark matter momenta. Evaluating some of the integrals, we can find a simpler form:

$$\mathrm{Br}(\pi^0 \to \gamma V^* \to \chi\chi^\dagger\gamma) = \int d\theta ds \alpha_D \epsilon^2 \sin^3(\theta) \frac{\sqrt{1 - \frac{4m_\chi^2}{s}} \left({m_{\pi^0}}^2 - s\right)^3 (s - 4m_\chi^2)}{8 m_{\pi^0}^6 \pi \left((s - m_V^2)^2 + m_V^2 \Gamma_V^2\right)}, \tag{4.4}$$

where θ is the angle between the V momentum in the π^0 rest frame and the χ momentum in the V rest frame. This integral must be evaluated numerically. A similar expression holds for η, but with $m_{\pi^0} \to m_\eta$ and an additional factor of $\mathrm{Br}(\eta \to \gamma\gamma)$.

Leptophobic

The leptophobic case uses the same distributions, but the branching ratio formula is slightly different from (4.1) (see [15] for more details),

$$\mathrm{Br}(X \to \gamma V_B) = 2\left(c_X \frac{g_B}{e} - \epsilon\right)^2 \left(1 - \frac{m_V^2}{m_X^2}\right) \times \mathrm{Br}(X \to \gamma\gamma), \tag{4.5}$$

where $c_\pi = 1$ and $c_\eta = 0.61$, where the coupling between the V and the neutral mesons arises due to the axial anomaly [15]. While the production of off-shell V's via meson decays are possible in this mode, they tend to be far more heavily suppressed than in the kinetic mixing case. The reason for this is simple, in both cases going off-shell imposes a penalty on the production rate of approximately α'. In the kinetic mixing case we are most interested in values of that are within an order of magnitude

of $\alpha' \approx 0.1$. In the leptophobic case, the regions of the parameter space of interest often possess values of $\alpha' \equiv \alpha_B < 10^{-4}$, which eliminates any possible sensitivity.

Meson Production

The decay of a pseudoscalar meson to a pair of dark matter particles (and a photon) is well understood and contains very little ambiguity. Unfortunately, the previous statement does not hold for estimates of the production rate and distribution of those mesons. The majority of neutrinos at fixed target experiments are produced through the decays of charged pions, with the kaons contributing to a lesser but still important extent. As a result the production rates and distributions of these particles are studied through both simulation and dedicated experiments that recreate some approximation of the target setup.

The π^0's and η's in which we are interested primarily decay via radiative channels and do not contribute to the neutrino signal or background of fixed target neutrino experiment. As a result, these particles attract less experimental study and obtaining information on their production can be difficult. Calculating N_X, the total number of mesons produced in a neutrino experiment, by simulating interactions with the target would be a daunting task, and would still suffer from large uncertainties without access to the beamline simulation maintained by the experimental collaboration[1].

An alternative approach is to estimate the π^0 production distribution using charged pion data. N_{π^0} should be very similar to $N_{\pi^\pm}$, and so we will make the estimate $N_{\pi^0} \approx \frac{N_{\pi^-}+N_{\pi^+}}{2}$. We will maintain the same approach for the momentum and angular distribution of produced π^0's,

$$\frac{d^2\sigma_{pN\to\pi^0+Y}}{d\theta_{\pi^0}dp_{\pi^0}} \approx \frac{1}{2}\left(\frac{d^2\sigma_{pN\to\pi^++Y}}{d\theta dp_{\pi^+}} + \frac{d^2\sigma_{pN\to\pi^-+Y}}{d\theta dp_{\pi^-}}\right), \tag{4.6}$$

where θ_{π^0} is the emission angle of the pion relative to the beam axis, and p_{π^0} is the momentum of the pion. This approach seems reasonable, as the production of pions proceeds through strong processes, and electromagnetic effects related to their charges should lead to minor corrections. The experimental literature lends support to this method, as production cross sections between the three pion flavours are broadly similar [160], and previous experimental studies have approximated the π^0

[1]Even access to the beamline simulation might not be sufficient. While these simulations are often calibrated with experimental data for charged meson production from replica targets, the same does not necessarily hold for π^0 or η production.

momentum distribution by the mean of the charged pion distributions with some success [161, 162]. Estimates of η production and momentum distribution are, if anything, even harder to find than those of π^0. We will use the same distributions for the eta as were used for the π^0 for lack of a better alternative.

Three distributions are used in this analysis, each suited to a different energy range. For the lowest energies, those below a GeV, we adopt the π^+ production parameterization formulated by Burman and Smith [163]. This fit can be scaled to any atomic number and interpolates between beam kinetic energies of 585 MeV and 730 MeV, though it appears to scale comfortably to energies as large as 1 GeV. The angular fit is performed using spline functions, and is well defined for production angles as large as 180° relative to the beam direction. This distribution is used for experiments with sub-GeV kinetic energy proton beams such as LSND and COHERENT. See Fig. 4.2.1 for a sample distribution.

Moving to moderate beam energies, a Sanford-Wang distribution fit has been prepared specifically for the MiniBooNE experiment [164]. As such, this fit is only applicable to the MiniBooNE beam energy of 8.9 GeV. It was calibrated using data from a thin beryllium[2] target, and so it does not include the secondary interaction effects that would be expected from thicker targets such as the 71 cm of beryllium (one nuclear interaction length) used by the MiniBooNE experiment itself. See Figs. 4.2.1 and 4.2.1 for plots of the distribution. The distribution is somewhat peaked in the forward direction, and falls off to an almost isotropic distribution at large angles. The distribution is not well defined for angles above $\pi/2$ relative to the beam direction, but is approximately isotropic at large angles and so we take

$$\frac{d^2\sigma_{pN\to\pi^0+Y}}{d\theta dp_{\pi^0}}(\theta > \pi/2) = \frac{d^2\sigma_{pN\to\pi^0+Y}}{d\theta dp_{\pi^0}}(\pi/2) \tag{4.7}$$

when required to sample angles larger than $\pi/2$.

Finally, for large energies we look to a parameterization by Bonesini, Marchionni, Pietropaolo and Tabarelli de Fatis [165], which will be called the BMPT distribution. This distribution is similar to the Burman-Smith distribution in that it can be scaled to energies as low as 10 GeV and as high as several hundred GeV such as those found at MINOS or SHiP. See Figs. 4.2.1 and 4.2.1 for plots of the distribution.

[2]This is a replica target, and therefore must be made of the same material as the MiniBooNE target.

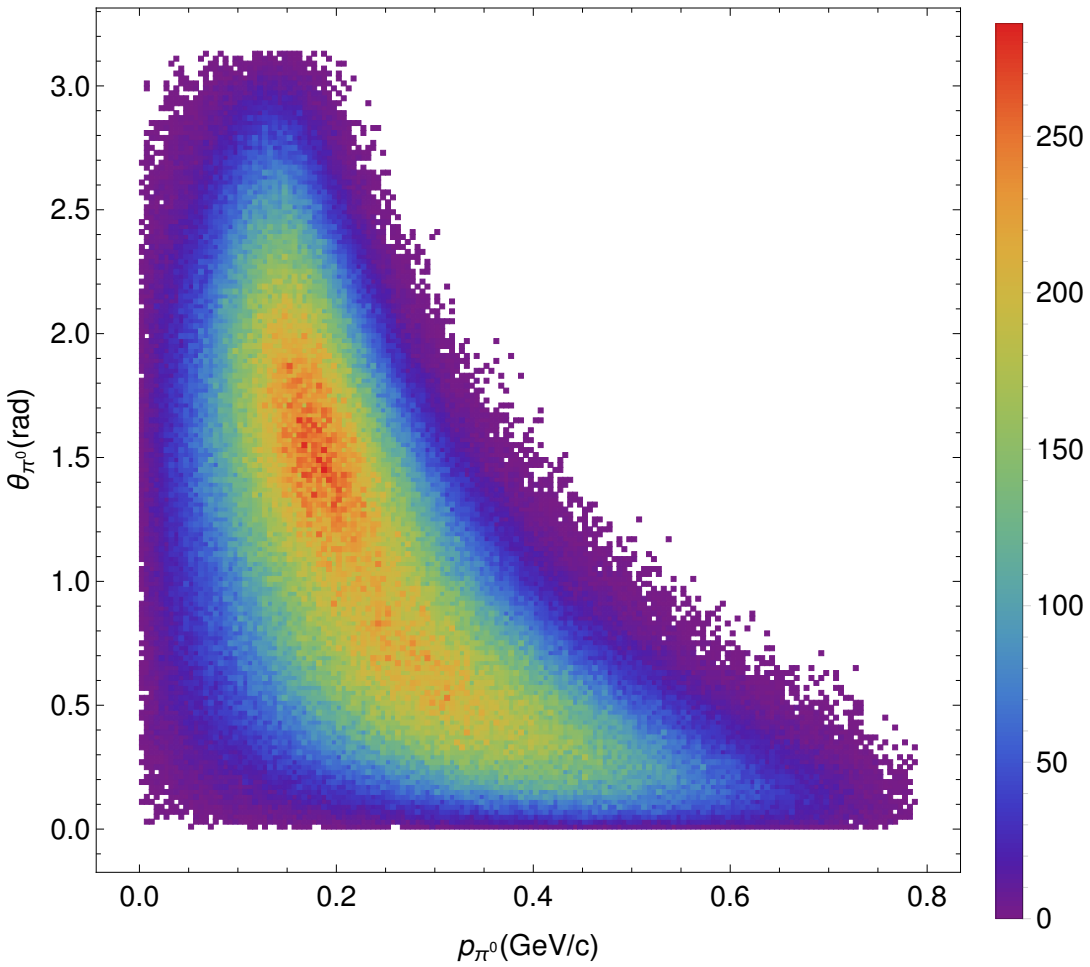

Figure 4.2: A density plot of 10^6 sample π^0's generated using the Burman-Smith distribution for a beam kinetic energy of 800 MeV incident on a carbon target (Z=6). Production exhibits a very large angular spread.

4.2.2 π^- Capture

π^- capture on protons can provide a significant source of relatively low energy dark matter particles through a Panofsky-like process

$$\pi^- + p \to n + V^* \to n\chi^\dagger\chi. \tag{4.8}$$

The π^- capture results in the emission of an isotropic and approximately monochromatic distribution of photons, and therefore we expect the same to hold true for V mediators produced through kinetic mixing. The isotropic nature of the decay channel is particularly relevant for experiments with detectors located at large angles relative

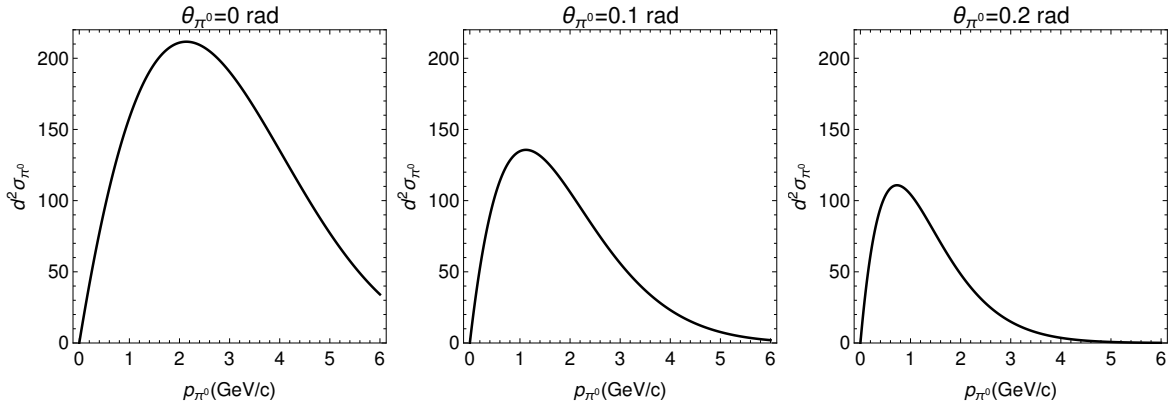

Figure 4.3: Slices of the double differential Sanford-Wang distribution. Note that while the MiniBooNE detector subtends ≈ 0.1 rad, π^0's from larger angles still make significant contributions to the signal.

to the beam axis, as their sensitivity to meson decay in flight is heavily penalized by the forward boost. Experimental data indicates that the photon emitted during the de-excitation of a nucleon following a π^- capture interaction peaks with an energy of 129 MeV, with a width of approximately six percent [166].

4.2.3 Proton Bremsstrahlung

The emission of V mesons through proton bremsstrahlung,

$$p + N \to V + p' + N,$$

could produce a significant number of dark matter particles with very little angular spread. The treatment here follows and elaborates upon previous work on vector boson production in proton bremsstrahlung[167, 168]. In this process, we define the four-vectors for the incident proton and emitted V as

$$p = (E_p = P + \frac{m_p^2}{2P}, 0, 0, P), \tag{4.9}$$

$$p_V = (E_V = zP + \frac{p_\perp^2 + m_V^2}{2Pz}, p_\perp \cos(\phi), p_\perp \sin(\phi), zP), \tag{4.10}$$

where p is the momentum of the incident proton, p_V is the momentum of the outgoing V boson, z is the fraction of the forward beam momentum carried by the outgoing V and $p_\perp$ is the V momentum perpendicular to the beam axis.

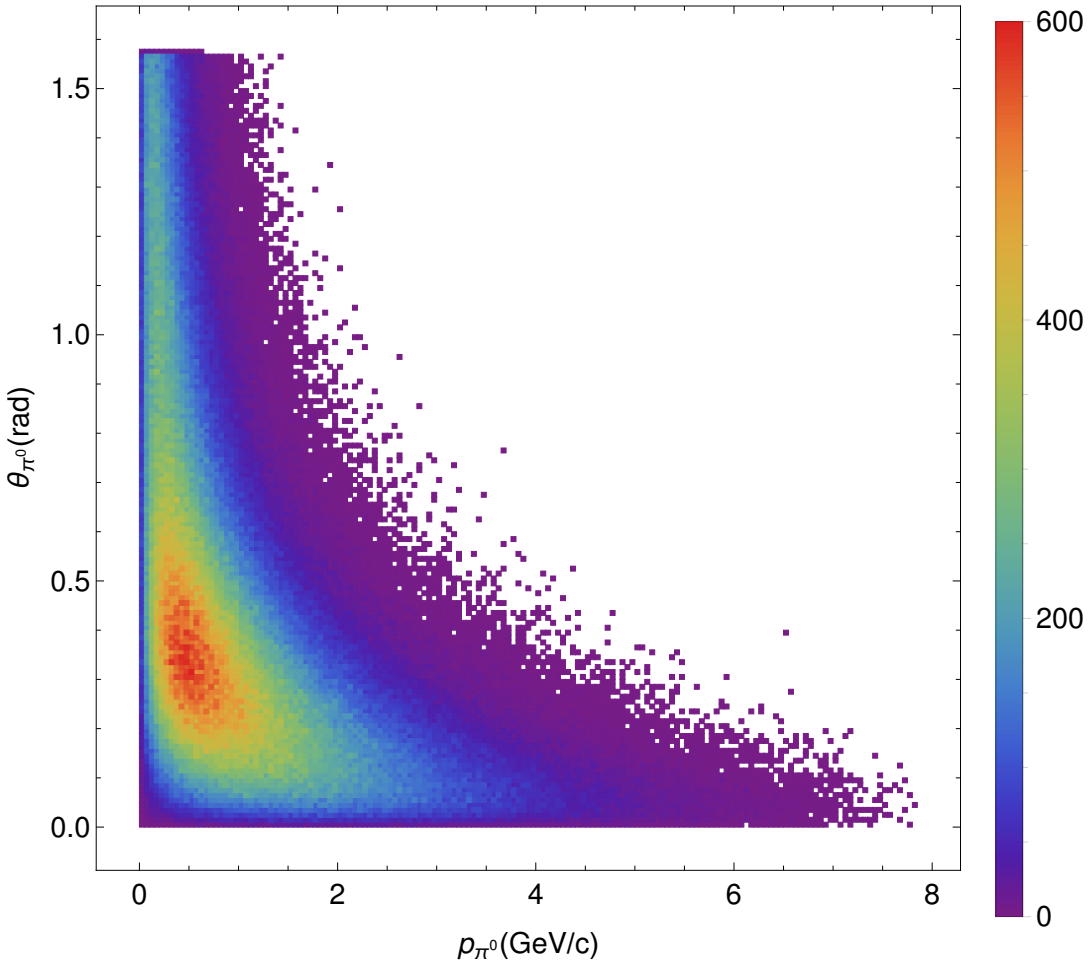

Figure 4.4: A density plot of 10^6 sample π^0's generated using the Sanford-Wang distribution. Note that the distribution becomes almost isotropic at largest angles. The number of π^0's at very small angles is suppressed by a factor of $\sin(\theta)$.

Kinetic Mixing

In the kinetic mixing scenario the differential V production rate per nucleon interaction is calculated using an analogue of the improved Weizsäcker-Williams approximation [169, 170, 171, 172]. The calculation factorizes the more complicated $2 \to 3$ bremsstrahlung process of (4.9) into inelastic proton-nucleus scattering $p + A \to X$ and the $2 \to 2$ scattering $p + b \to p' + V$. The V production rate per incident proton is written as

$$\frac{d^2 N_V}{dz dp_\perp^2} = \frac{\sigma_{pA}(s')}{\sigma_{pA}(s)} F_{1,p}^2(q^2) w_{ba}(z, p_\perp^2), \tag{4.11}$$

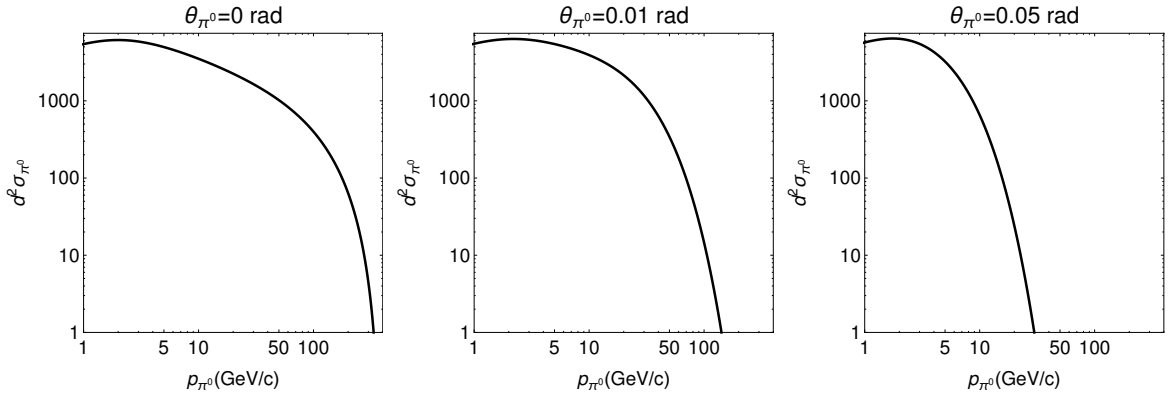

Figure 4.5: Slices of the double differential BMPT distribution for a 400 GeV proton beam incident on a Tungsten (A=184) target.

with $s' = 2m_p(E_p - E_V)$, $s = 2m_pE_p$. The photon splitting function providing the probability density for the subprocess $p \to p' + V$ is written as

$$\begin{aligned} w_{ba}(z, p_\perp^2) =& \frac{\epsilon^2 \alpha_{\rm EM}}{2\pi H}\left[\frac{1+(1-z)^2}{z} - 2z(1-z)\left(\frac{2m_p^2+m_V^2}{H} - z^2\frac{2m_p^4}{H^2}\right)\right. \\ &\left. + 2z(1-z)(z+(1-z)^2)\frac{m_p^2 m_V^2}{H^2} + 2z(1-z)^2\frac{m_V^4}{H^2}\right], \end{aligned} \tag{4.12}$$

with

$$H = p_\perp^2 + (1-z)m_V^2 + z^2 m_p^2. \tag{4.13}$$

We use a timelike form factor $F_{1,p}(q^2)$ defined in Faessler *et. al.* [17] as

$$F_{1,p}(q^2) = F_1^{(v)}(q^2) + F_1^{(s)}(q^2). \tag{4.14}$$

Under the extended Vector Meson Dominance model employed by Faessler *et. al.*, the nucleon form factors are defined in terms of their couplings to the ground and excited states of the vector mesons ρ and ω[3]. The isovector $F_1^{(v)}$ and isoscalar $F_1^{(s)}$

[3]In this model it is destructive interference between these terms that results in the asymptotic behavior $F_{1,p}(Q^2 \to \infty) \sim \frac{1}{Q^4}$.

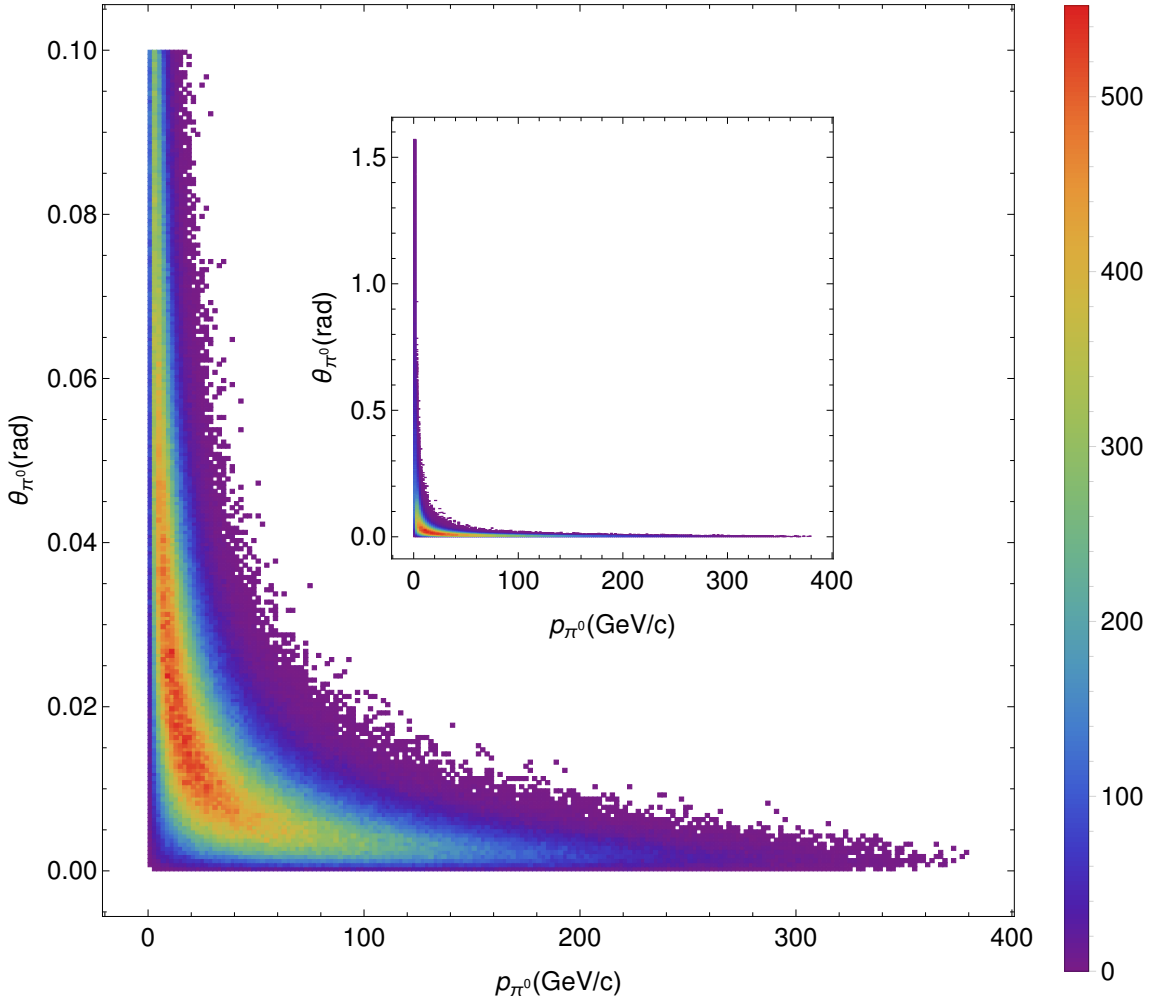

Figure 4.6: A density plot of 10^6 sample π^0's generated using the BMPT distribution for a 400 GeV proton beam incident on a Tungsten (A=184) target.

components[4] are defined as

$$F_1^{(v)} = \frac{f_1^{\rho NN}}{g_\rho}\frac{m_\rho^2}{m_\rho^2 - im_\rho\Gamma_\rho - q^2} + \frac{f_1^{\rho' NN}}{g_{\rho'}}\frac{m_{\rho'}^2}{m_{\rho'}^2 - im_\rho\Gamma_{\rho'} - q^2} + \frac{f_1^{\rho'' NN}}{g_{\rho''}}\frac{m_{\rho''}^2}{m_{\rho''}^2 - im_\rho\Gamma_{\rho''}}, \tag{4.15}$$

[4]In Faessler *et. al.* these are written as F_1^ρ and F_1^ω.

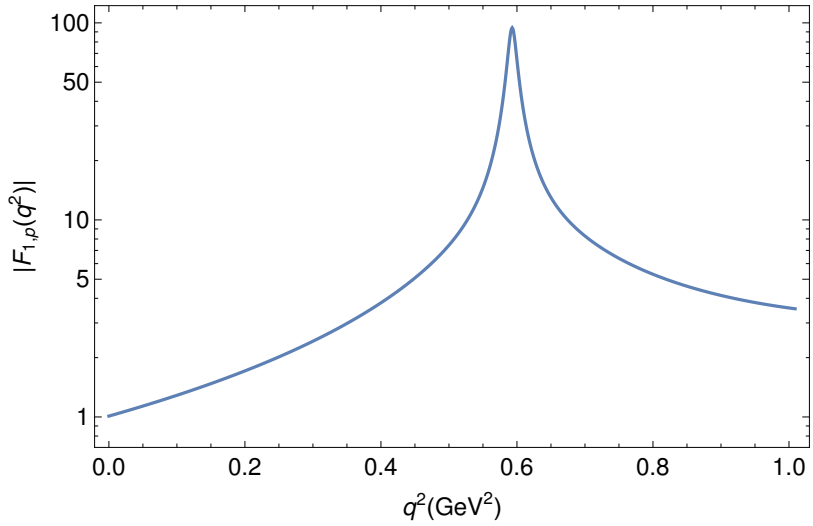

Figure 4.7: The timelike form factor $F_{1,p}(q^2)$ from [17].

and

$$F_1^{(s)} = \frac{f_1^{\omega NN}}{g_\omega} \frac{m_\omega^2}{m_\omega^2 - i m_\omega \Gamma_\omega - q^2} + \frac{f_1^{\omega' NN}}{g_{\omega'}} \frac{m_{\omega'}^2}{m_{\omega'}^2 - i m_\omega \Gamma_{\omega'} - q^2} + \frac{f_1^{\omega'' NN}}{g_{\omega''}} \frac{m_{\omega''}^2}{m_{\omega''}^2 - i m_\omega \Gamma_{\omega''}}, \tag{4.16}$$

with the parameters defined as in [17]. It should be noted that our region of interest includes a resonance peak at m_ρ for which there is little to no data, and is by necessity poorly constrained. While the inclusion of this form factor is necessary to make the best possible estimate of the V production rate, it appears likely that it overestimates production near the peak of the resonance region, and introduces significant uncertainty into the overall production rate at this point (see Fig. 4.7).

Note that due to the assumption that the incoming fermion is relativistic, and emits V at a small angle, several kinematic conditions must hold to make use of these results, summarized in [168] as

$$E_p, E_V, E_p - E_V \gg m_p, m_V, |p_\perp|. \tag{4.17}$$

In order to calculate the total V production rate, and therefore the dark matter signal χ, 4.11 must be integrated over z and $p_\perp$ with ranges chosen such that 4.17 is satisfied. These conditions are easily satisfied by $z \in [0.1, 0.9]$ and $|p_\perp| < 1$ GeV for high energy experiments such as SHiP, but we must be a bit more careful at lower energies. For MiniBooNE energies, the energy of the incident and outgoing proton,

as well as E_V, the energy of the emitted V, must be much larger than 1 GeV, though exactly what this means in this case is unclear. We have chosen a range $z \in [0.3, 0.7]$ for MiniBooNE and $|p_\perp| < 0.2$ GeV, which should allow for some margin for error.

Leptophobic

The treatment of proton bremsstrahlung in the leptophobic scenario is nearly identical to that of kinetic mixing, with changes to only the overall scaling of (4.12) and the timelike form factor. In (4.12) we make the substitution $\epsilon^2 \alpha_{\rm EM} \to (4\pi)^{-1}$, moving all couplings into the form factor. The form factor F_1^p itself is replaced with $\tilde{F}_1^p$, defined later in (4.39). Note that for $\epsilon = 0$, the isovector component drops out as expected.

4.2.4 Vector Meson Mixing

This channel estimates the production of dark matter due to the decay of vector mesons $X = \rho, \omega, \phi$ to DM pairs, $X \to \chi\bar{\chi}$. In order to avoid double counting, this channel has largely been deprecated in favor of proton bremsstrahlung production, as it provides a better estimate of the production rate from ρ and ω decays for most masses. The $\phi \to \chi\bar{\chi}$ channel can still be used alongside the proton bremsstrahlung channel, but has a negligible effect on the observed signal when $m_V \neq m_\phi$. This treatment is drawn from [15].

It will be convenient to normalize the branching ratios to $\mathrm{Br}(X \to e^+e^-)$, which occurs due to $X - \gamma$ mixing. Consider the generic couplings

$$\mathcal{L} \supset g_{XY} X_\mu Y^\mu + g_F Y_\mu \bar{F}\gamma^\mu F + i g_S Y_\mu S^* \overleftrightarrow{\partial^\mu} S, \tag{4.18}$$

where X is a vector meson, Y is either the photon or baryonic vector V_B, F is the electron or Dirac fermion DM, and S is the complex scalar DM. The partial decay widths for $X \to \bar{F}F$ and $X \to S^*S$ are given by

$$\begin{aligned}
\Gamma(X \to \bar{F}F) &= \frac{g_F^2 g_{XY}^2 m_X}{12\pi} \frac{1}{(m_X^2 - m_Y^2)^2 + m_Y^2\Gamma_Y^2} \left(1 + \frac{2m_F^2}{m_X^2}\right)\left(1 - \frac{4m_F^2}{m_X^2}\right)^{1/2}, \\
\Gamma(X \to S^*S) &= \frac{g_S^2 g_{XY}^2 m_X}{48\pi} \frac{1}{(m_X^2 - m_Y^2)^2 + m_Y^2\Gamma_Y^2} \left(1 - \frac{4m_S^2}{m_X^2}\right)^{3/2}.
\end{aligned} \tag{4.19}$$

The X-photon mixing Lagrangian under Vector Meson Dominance is

$$\mathcal{L} \supset \frac{\sqrt{2}e}{g} A^\mu \left(m_\rho^2 \rho_\mu + \tfrac{1}{3} m_\omega^2 \omega_\mu - \tfrac{\sqrt{2}}{3} m_\phi^2 \phi_\mu \right). \tag{4.20}$$

We therefore identify the photon-X mixing parameter g_{XA}, defined via Eq. (4.18), as $g_{XA} = \frac{\sqrt{2}e}{g} m_X^2 a_X$, $a_X = (1, \frac{1}{3}, -\frac{\sqrt{2}}{3})$, where g is fixed phenomenologically. The $X - V_B$ mixing Lagrangian is

$$\mathcal{L} \supset \frac{\sqrt{2}}{g} V_B^\mu \left[(-\epsilon e)\, m_\rho^2\, \rho_\mu \,+\, \tfrac{1}{3}\,(2 g_B - \epsilon e)\, m_\omega^2\, \omega_\mu - \tfrac{\sqrt{2}}{3}\,(-g_B - \kappa e)\, m_\phi^2\, \phi_\mu \right]. \tag{4.21}$$

The $X - V_B$ mixing parameter g_{XV} is thus $g_{XV} = \frac{\sqrt{2}}{g} m_X^2 a_X (c_X g_B - \epsilon e)$, where $a_X = (1, \frac{1}{3}, -\frac{\sqrt{2}}{3})$, $c_X = (0, 2, -1)$.

We then obtain the branching ratio for $X \to \chi\bar{\chi}$:

$$\begin{aligned} \frac{\mathrm{Br}(X \to \chi\bar{\chi})}{\mathrm{Br}(X \to e\bar{e})} = r_\chi \left(c_X \frac{g_B}{e} - \epsilon \right)^2 \left(\frac{g_B q_B}{e} \right)^2 \frac{m_X^4}{(m_X^2 - m_V^2)^2 + m_V^2 \Gamma_V^2} \\ \times \left(1 + a_\chi \frac{m_\chi^2}{m_X^2} \right) \left(1 - \frac{4 m_\chi^2}{m_X^2} \right)^{1/2}, \end{aligned} \tag{4.22}$$

where $r_\chi = (1, \frac{1}{4})$, $a_\chi = (2, -4)$ for a Dirac fermion and complex scalar DM. We have taken $g_S = g_B q_B$ for the DM coupling to V_B.

4.2.5 Direct production

Direct production corresponds to parton level processes such as

$$pN \to V^* \to \chi^\dagger \chi \tag{4.23}$$

as shown in fig 4.8. For this calculation we will use the narrow width approximation and produce the V on-shell. As with the on-shell meson production processes, the production cross section for a DM pair can be written as

$$\sigma(pN \to V^* \to \chi^\dagger \chi) = \sigma(pN \to V) \mathrm{Br}(V \to \chi^\dagger \chi). \tag{4.24}$$

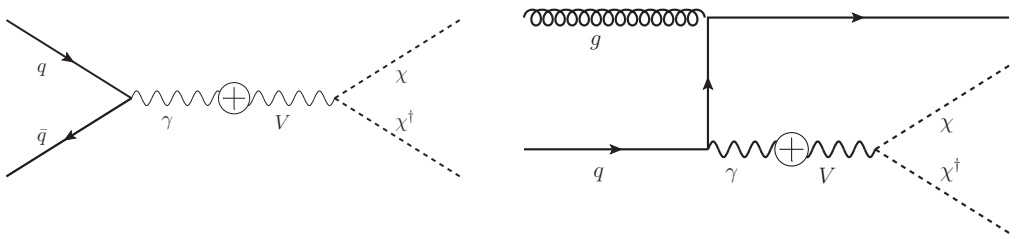

Figure 4.8: Direct production of scalar dark matter via the vector portal. The leading-order process is shown on the left, which is helicity suppressed in the forward direction. The process on the right is higher order in α_s, and also phase space suppressed, but has less helicity suppression in the forward direction. Only the leading order contribution is included.

The direct production cross section of a vector mediator is

$$\begin{aligned}\sigma\left(pp(n)\to V\right) &= \int_\tau^1 dx\ \frac{d\sigma\left(pp(n)\to V\right)}{dx} \\ &= \frac{4\pi^2\alpha\kappa^2}{m_V^2}\sum_q e_q^2\int_\tau^1\frac{dx}{x}\ \tau\left[f_{q/p}\left(x\right)f_{\bar{q}/p(n)}\left(\frac{\tau}{x}\right)+f_{\bar{q}/p}\left(x\right)f_{q/p(n)}\left(\frac{\tau}{x}\right)\right],\end{aligned} \tag{4.25}$$

where e_q is the charge of quark q in units of the positron electric charge, $\tau = m_V^2/s$, and $\sqrt{s}$ is the hadron-level center-of-mass energy. For the leptophobic case, the cross section is similar, but we use $e_q = \frac{1}{3}$ as the model couples to baryon number rather than charge.

The parton distribution function (PDF) $f_{q/p(n)}(x)$ gives the probability of extracting the quark q with momentum fraction x from a proton (neutron) and similarly for $f_{\bar{q}/p(n)}\left(x\right)$. We have omitted the scale, Q, at which the PDFs are evaluated. To obtain estimates, we use CTEQ6.6 PDFs [173] and set $Q = m_V$. Varying Q in between $m_V/2$ and $2m_V$ resulted in an uncertainty in the production cross section of less than $\sim 30\%$ for $m_V > 1$ GeV at beam energies of 30 GeV and 120 GeV. Higher-order QCD corrections are large, introducing an error that can potentially be $\mathcal{O}(1)$.

The production cross section as a function of the DM lab frame energy, E_χ, and the angle between its lab frame momentum and the beam direction, θ, can be related

to the differential cross section in Eq. (4.25) through

$$\frac{d\sigma\left(pp(n) \to V \to \bar{\chi}\chi\right)}{dE_\chi d\cos\theta} = \left[\frac{\partial(x, \cos\hat{\theta})}{\partial(E_\chi, \cos\theta)}\right] \frac{d\sigma\left(pp(n) \to V\right)}{dx} \text{Br}\left(V \to \bar{\chi}\chi\right) g\left(\cos\hat{\theta}\right), \tag{4.26}$$

where $\hat{\theta}$ is the angle between the momentum of χ and the beam in the V rest frame and the quantity in square brackets is the Jacobian associated with this variable change. The function g describes the angular distribution of the DM in the V rest frame. For scalar DM produced through a vector mediator, this is

$$g\left(\cos\hat{\theta}\right) = \frac{3}{4}\left(1 - \cos^2\hat{\theta}\right). \tag{4.27}$$

4.3 Detection Signatures

Now that we have estimates of the number and distribution of dark matter particles produced under the hidden sector scenarios, we need to determines how their presence in a fixed target neutrino experiment's detector could be observed. Four scattering channels were considered:

1. Neutral Current-like Elastic Electron Scattering $\chi e \to \chi e$,
2. Neutral Current-like Elastic Nucleon Scattering $\chi N \to \chi N$,
3. Neutral Current-like Coherent Nuclear Scattering $\chi A \to \chi A$,
4. Neutral Current-like Inelastic π^0 Production $\chi N \to \Delta\chi$, $\Delta \to \pi^0 N$.

Only Neutal Current-like Elastic (NCE) Nucleon and Coherent Nuclear Scattering will be considered for the baryonic case, while all four will be considered for the kinetic mixing scenario.

4.3.1 NCE Electron Scattering

Neutral current-like elastic electron dark matter scattering was the signal channel used at LSND to impose constraints on low mass hidden sector dark matter, and is also quite effective when employed at very high energy experiments due to its low

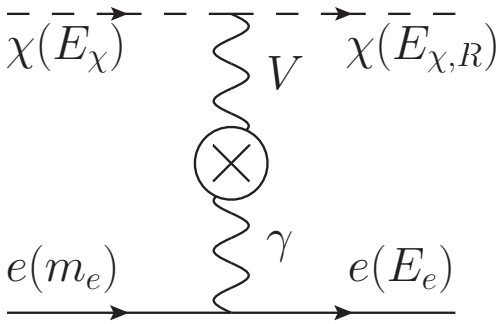

Figure 4.9: The neutral current-like elastic dark matter-electron scattering diagram, where we have labeled the energies of all external legs.

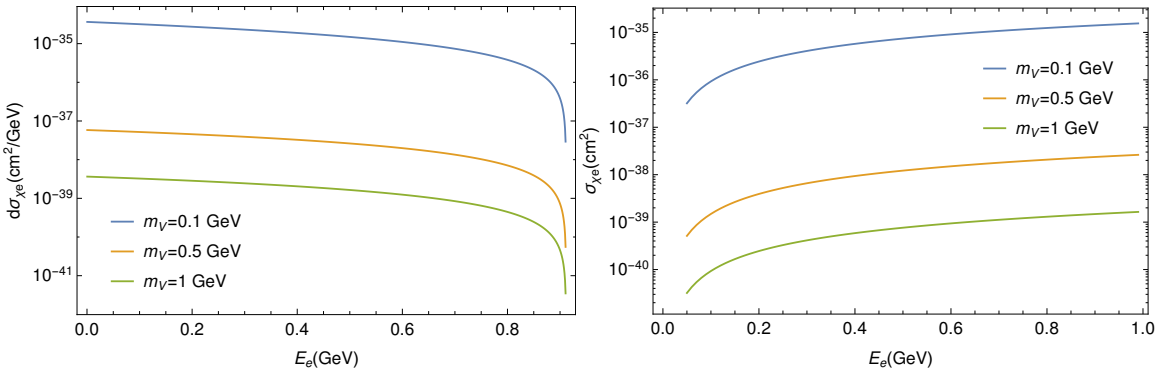

Figure 4.10: The left plot shows the differential scattering cross section given by 4.29 for $E_\chi = 1$ GeV, $m_\chi = 10$ MeV, $\epsilon = 10^{-3}$, $\alpha' = 0.1$ and three values of m_V. On the right we have plotted the total cross section given by 4.30 for a range of incident dark matter energies E_χ, while using the same model parameters as in the left plot.

angular spread. The amplitude of differential scattering cross section for neutral current-like elastic dark matter electron scattering (see Fig. 4.9) can be written as

$$\mathcal{M} = iee'(p_\chi + p_{\chi,R})_\mu \left(\frac{g^{\mu\nu} - \frac{q^\mu q^\nu}{m_V^2}}{m_V^2 - q^2} \right) \bar{u}_(p_e, s)\gamma_\nu u(p_{e,i}, r), \tag{4.28}$$

where p_χ and $p_{\chi,R}$ are the initial and final state χ four-momenta, and $p_{e,i}$ and p_e are the initial and final state electron four-momenta. Utilizing this amplitude in the lab frame, we can find the differential scattering cross-section:

$$\frac{d\sigma_{e\chi\to e\chi}}{dE_e} = 4\pi\epsilon^2\alpha'\alpha_{\rm EM}\frac{2m_eE_\chi^2 - \left(2m_eE_\chi + m_\chi^2\right)(E_e - m_e)}{(E_\chi^2 - m_\chi^2)(m_V^2 + 2m_eE_e - 2m_e^2)^2}, \tag{4.29}$$

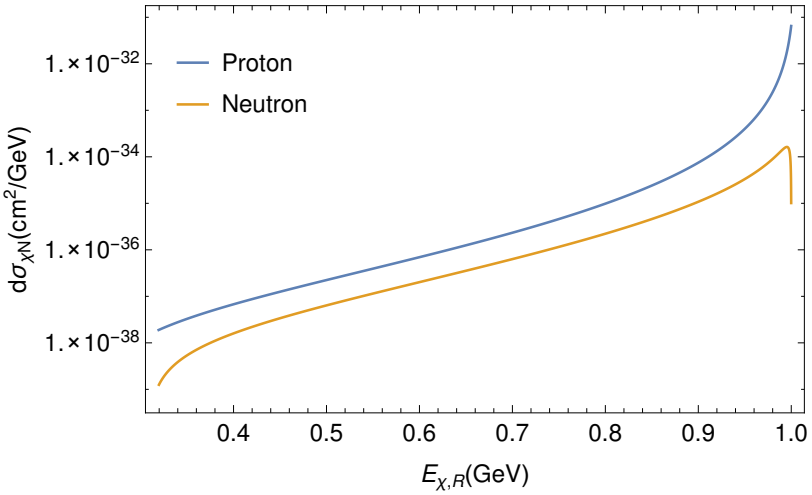

Figure 4.11: The differential nucleon-dark matter scattering cross section of equation 4.33 with $m_\chi = 10$ MeV, $m_V = 100$ MeV and $E_\chi = 1$ GeV. Note that the neutron scattering cross section falls to zero at $q^2 = 0$ because $F_{1.N}(q^2 = 0) = 0$

where E_e and m_e are the energy and mass of the recoiling electron, and E_χ is the energy of the incident dark matter particle. Unlike many of the cross sections that follow, (4.29) can be integrated analytically to find

$$\begin{aligned}\sigma_{e\chi\to e\chi}(E_e) =& 4\pi\epsilon^2\alpha_{\mathrm{EM}}\alpha' \\ &\times \frac{\frac{4E_\chi^2 m_e^2 + 2E_\chi m_e m_V^2 + m_V^2 m\chi^2}{2E_e m_E - 2m_e^2 + m_V^2} + (2E_\chi m_E + m_\chi^2)\log(2E_e m_e - 2m_e^2 + m_V^2)}{4m_e^2(E_\chi^2 - m_\chi^2)},\end{aligned} \tag{4.30}$$

where the total cross section is found by evaluating $\sigma^{\mathrm{total}}_{e\chi\to e\chi} = \sigma_{e\chi\to e\chi}(E_{e,\max}) - \sigma_{e\chi\to e\chi}(E_{e,\min})$. The recoil energy as a function of scattering angle θ is given by

$$E_e(\theta) = m_e \frac{(E_\chi + m_e)^2 + (E_\chi^2 - m_\chi^2)\cos^2(\theta)}{E_\chi + m_e)^2 + (E_\chi^2 - m_\chi^2)\cos^2(\theta)}, \tag{4.31}$$

where $E_{e,\max} = E_e(\theta = 0)$ and $E_{e,\min} = E_e(\theta = \pi/2)$.

4.3.2 NCE Nucleon Scattering

NCE nucleon-dark matter scattering is a channel of great interest for MiniBooNE, T2K and, to a lesser extent, coherent neutrino scattering experiments like COHERENT and CENNS. This channel is less useful for very high energy experiments such

as SHiP, where inelastic scattering channels would be expected to dominate due to the large momentum transfers possible.

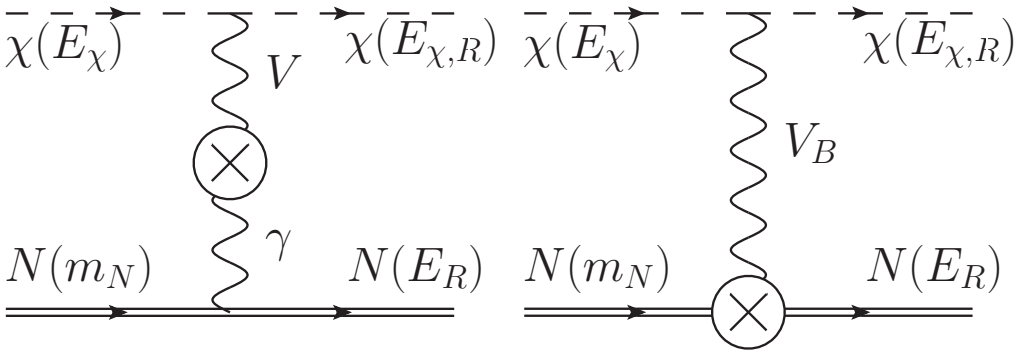

Figure 4.12: The neutral current-like elastic dark matter-nucleon scattering diagram in both the kinetic mixing (left) and leptophobic (right) models, where we have labeled the energies of all external legs.

Kinetic Mixing

The NCE nucleon-dark matter scattering amplitude in the kinetic mixing case is

$$\mathcal{M} = iee'(p_\chi + p_{\chi,R})_\mu \left(\frac{g^{\mu\nu} - \frac{q^\mu q^\nu}{m_V^2}}{m_V^2 - q^2} \right) \bar{u}(p_R, s) \left(\gamma_\nu F_{1,N} + \frac{i\sigma_{\mu\nu} q^\nu}{2m_N} F_{2,N} \right) u(p_{p,i}, r), \tag{4.32}$$

where we use the same convention as in the electron case, but with the outgoing nucleon four-momentum labeled as p_R. The differential scattering cross section was calculated in [65] to be

$$\frac{d\sigma_{N\chi\to N\chi}}{dE_{\chi,R}} = 4\pi\alpha'\alpha_{\rm EM}\epsilon^2 \frac{F_{1,N}^2(q^2)A_N + F_{2,N}^2(q^2)B_N + F_{1,N}(q^2)F_{2,N}(q^2)C_N}{(m_V^2 + 2m_N(E_\chi - E_{\chi,R}))^2(E_\chi^2 - m_\chi^2)}, \tag{4.33}$$

where $E_{\chi,R}$ is the energy of the outgoing χ and A_N, B_N and C_N are the following functions

$$A_N = 2m_N E_\chi E_{\chi,R} - m_\chi^2(E_\chi - E_{\chi,R}), \tag{4.34}$$

$$B_N = (E_{\chi,R} - E_\chi)\left((E_{\chi,R} + E_\chi)^2 + 2m_N(E_{\chi,R} - E_\chi) - 4m_\chi^2\right), \tag{4.35}$$

$$C_N = (E_{\chi,R} - E_\chi)(m_N(E_\chi - E_{\chi,R}) + 2m_\chi^2). \tag{4.36}$$

The Dirac and Pauli form factors $F_{i,N}, i = 1, 2, N = n, p$ used in this work are the

BBA-03 form factors for neutrino-nucleon scattering from [174]. These were largely chosen due to their adoption by a number of MiniBooNE analyses. More recent form factors exist, and have in fact been used, but do not have a noticeable effect on the results given the other much larger uncertainties present in this analysis.

The minimum dark matter recoil energy is given by

$$\mathrm{MIN}(E_{\chi,R}) = \frac{2m_N m_\chi^2 E_\chi (m_N^2 + m_\chi^2)}{2E_\chi m_N + m_N^2 + m_\chi^2}, \tag{4.37}$$

while the maximum recoil is equal to E_χ.

Leptophobic

The scattering cross section in the leptophobic scenario is identical to that of the kinetic mixing case up to the form factors and the coupling constants,

$$\frac{d\sigma_{N\chi\to N\chi}}{dE_{\chi,R}} = \alpha_B \frac{\tilde{F}_{1,N}^2(q^2)A_N + \tilde{F}_{2,N}^2(q^2)B_N + \tilde{F}_{1,N}(q^2)\tilde{F}_{2,N}(q^2)C_N}{(m_V^2 + 2m_N(E_\chi - E_{\chi,R}))^2(E_\chi^2 - m_\chi^2)}, \tag{4.38}$$

where $\tilde{F}_{i,N}$ are defined as

$$\tilde{F}_{i,p} = \frac{1}{2}(g_u - g_d)F_i^{(v)} + \frac{3}{2}(g_u + g_d)F_i^{(s)} + (g_u + 2g_d)F_i^{\mathcal{S}}, \tag{4.39}$$

$$\tilde{F}_{i,n} = -\frac{1}{2}(g_u - g_d)F_i^{(v)} + \frac{3}{2}(g_u + g_d)F_i^{(s)} + (g_u + 2g_d)F_i^{\mathcal{S}} \tag{4.40}$$

with $i = 1, 2$ and we have couplings

$$\begin{aligned} g_u &= \frac{g_B}{3} - \frac{2\kappa e}{3}, \\ g_d &= \frac{g_B}{3} + \frac{\kappa e}{3}, \\ g_e &= \kappa e. \end{aligned} \tag{4.41}$$

We can write the isovector and isoscalar form factors $F_i^{(v,s)}$ in terms of the Dirac and Pauli form factors used in the previous section,

$$\begin{aligned} F_i^{(v)} &= F_i^p - F_i^n, \\ F_i^{(s)} &= F_i^p + F_i^n. \end{aligned} \tag{4.42}$$

The strange form factors $F_i^{\mathcal{S}}$ are consistent with zero[175]. Note that the scattering cross section scales as α_B^2, as it picks up two factors of g_B from the form factors.

4.3.3 Coherent Nuclear Scattering

At low energies, dark matter can scatter coherently with the nucleus as a whole. This dominates for low momentum exchange, as it can add an enormous enhancement to the scattering rate for large target nuclei. The differential scattering rate scales as

$$\frac{d\sigma_{\chi A\to\chi A}}{dE_{\chi,R}} = \sum_{N=n,p} f_N(q^2)\frac{d\sigma_{\chi N\to\chi N}}{dE_{\chi,R}}. \tag{4.43}$$

where $q^2 = 2m_N(E_\chi - E_{\chi,R})$

$$f_N(q^2) = \begin{cases} n_N & q^2 > (50\,\mathrm{MeV})^2, \\ n_N^2|F_{\mathrm{Helm}}(\sqrt{q^2})| & q^2 < (50\,\mathrm{MeV})^2, \end{cases} \tag{4.44}$$

where $n_p = Z$, $n_n = (A - Z)$. For the kinetic mixing scenario only n_p contributes, while for $\mathrm{U}(1)_B$ we add both n_p and n. The Helm Form Factor is defined as [176]

$$F_{\mathrm{Helm}}(q) = \frac{3j_1(qR(A))}{qR(A)}e^{-qs}, \tag{4.45}$$

where j_1 is a Bessel function, $s \approx 0.9\,\mathrm{fm}$ is a suppression constant, and $R(A)$ calculates the radius of the nucleon based on the number of nuclei,

$$R(A) = \sqrt{c^2 + \frac{7}{2}\pi^2a^2 - 5s^2}, \tag{4.46}$$

with $a \approx 0.52\,\mathrm{fm}$ and

$$c \approx 1.23A^{1/3} - 0.6\,\mathrm{fm}. \tag{4.47}$$

4.3.4 Inelastic π^0 Production

The final detection signature considered in this work is inelastic π^0 production (see Fig. 4.13). In this process a dark matter particle excites a nucleon N to the $\Delta(1232)$ resonance, which subsequently decays via $\Delta \to N\pi^0$ with a branching ratio of $\frac{2}{3}$ [68].

While the calculation of the scattering rate itself is straightforward, assembling the theory required from the literature can be time consuming, so the relevant formulae

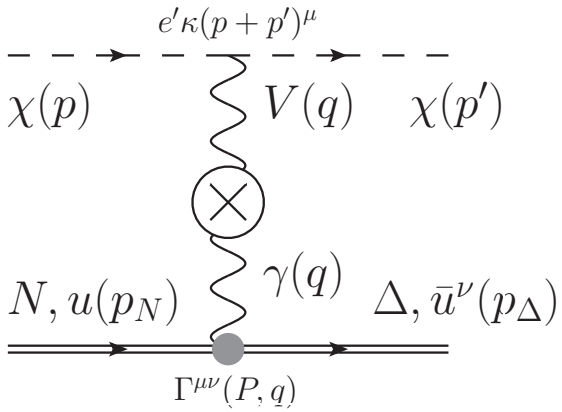

Figure 4.13: Inelastic dark matter-nucleon scattering, leading to the production of a Δ. The four-momenta of the external legs have been labeled.

will be reviewed here for the reader's convenience. The Δ is a spin-3/2 particle, the handling of which in Feynman diagram calculations is not routinely covered in particle physics texts. Spin-3/2 particles are represented by the product of both a vector particle's polarization and a spin-1/2 spinor component,

$$\psi^\mu_{3/2}(p,s) = \psi_{1/2}(p,s)\epsilon^\mu(p), \tag{4.48}$$

where $\psi^\mu_{3/2}$ is called a Rarita-Schwinger spinor [177].

The $\Delta - \gamma N$ vertex can be written as a combination of magnetic dipole, electric dipole and coulomb quadrupole terms [178]:

$$\Gamma_{\beta\mu}(P,q) = G^*_M(q^2)\mathcal{H}^M_{\beta\mu} + G^*_E(q^2)\mathcal{H}^E_{\beta\mu} + G^*_C(q^2)\mathcal{H}^C_{\beta\mu}. \tag{4.49}$$

It can be shown that for transition between an S-wave nucleon and Δ, $G^*_E(q^2), G^*_C(q^2) \to 0$ [179]. For G^*_M, the magnetic dipole form factor, we adopt a spectator quark model [179, 180, 181]. Including higher orbitals in the calculation allows for non zero electric and coulomb quadrupole contributions, but these are expected to add corrections of only a few percent. The magnetic dipole vertex is given by

$$\mathcal{H}^M_{\beta\mu} = -\frac{3(m_\Delta + m_N)}{2m_N\left((m_\Delta + m_N)^2 - q^2\right)}\epsilon_{\beta\mu\sigma\tau}P_\sigma q_\tau \times e\sqrt{\frac{2}{3}}, \tag{4.50}$$

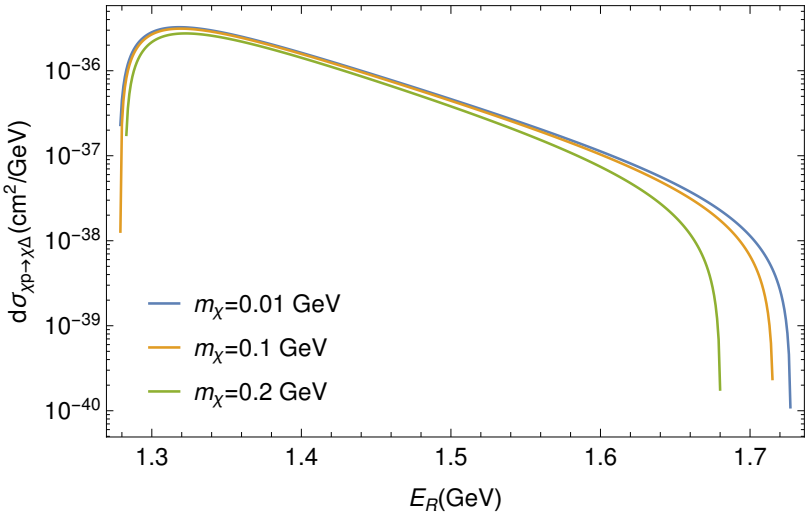

Figure 4.14: The differential $p\chi \to \Delta\chi$ scattering cross section of equation 4.59 with $m_V = 500$ MeV, $\kappa = 10^{-3}$, $\alpha' = 0.1$ and $E_\chi = 1$ GeV for three dark matter masses. Note that the Δ cannot be produced at rest due to momentum conservation.

where $q = p_N - p_\Delta$ is the momentum transfer and

$$P = \frac{p_N + p_\Delta}{2}. \tag{4.51}$$

Note that the factor of $e\sqrt{\frac{2}{3}}$ appended to the end of the magnetic dipole covariant is required to adhere to accepted normalization conventions [182].

The amplitude of the scattering process is

$$\mathcal{M} = iee'(p+p')_\mu \left(\frac{g^{\mu\nu} - \frac{q^\mu q^\nu}{m_V^2}}{m_V^2 - q^2} \right) \bar{u}_\rho(p_\Delta, s)\Gamma^{\rho\nu}(P,q)u(p_N,r) \tag{4.52}$$

$$= \frac{iee'(p+p')_\mu}{m_V^2 - q^2} \bar{u}_\rho(p_\Delta, s)\Gamma^{\rho\mu}(P,q)u(p_N,r). \tag{4.53}$$

where we have used $(p+p')\cdot q = 0$.

Squaring and averaging over initial spins,

$$\frac{1}{2}\sum_{r,s}|\mathcal{M}|^2 = \frac{(iee')^2(p+p')_\mu(p+p')_\nu}{2\left(m_V^2 - q^2\right)^2} \sum_{r,s} [\bar{u}_\rho(p_\Delta, s)\Gamma^{\rho\mu}(P,q)u(p_N,r)] \times [\bar{u}(p_N,r)\Gamma^{\sigma\nu}u_\sigma(p_\Delta,s)] \tag{4.54}$$

The spin sum over the Rarita-Schwinger spinors can be expressed in a several equiv-

alent forms. This work will follow the convention employed by [183],

$$\sum_s u^\mu(p,s)\bar{u}^\nu(p,s) = -(\not{p}+m_\Delta)\left(g^{\mu\nu} - \frac{\gamma^\mu\gamma^\nu}{3} - \frac{2p^\mu p^\nu}{3m_\Delta^2} + \frac{p^\mu\gamma^\nu - p^\nu\gamma^\mu}{3m_\Delta}\right) \tag{4.55}$$

$$= P_\Delta^{\mu\nu}(p) \tag{4.56}$$

Note that this expression is only valid for spin-3/2 particles with positive parity, a category which includes the Δ. Cleaning up the amplitude expression and evaluating the spin-sums leaves

$$\frac{1}{2}\sum_{r,s}|\mathcal{M}|^2 = \frac{(iee')^2(p+p')_\mu(p+p')_\nu}{2\left(m_V^2-q^2\right)^2}\mathrm{Tr}\left[P_\Delta^{\rho\sigma}(p)\Gamma^{\rho\mu}(P,q)(\not{p}_N+m_N)\Gamma^{\sigma\nu}(P,q)\right] \tag{4.57}$$

$$\begin{aligned}=&\frac{4\pi^2\alpha\alpha'\kappa^2 G_M^*(-t)^2(m_\Delta+m_N)^2}{m_N^2(m_V^2-t)^2}\\ &\times[((m_\Delta+m_N)^2-t)(-2m_N^2(m_\Delta^2+t)(4m_\chi^2-t)+m_N^4(4m_\chi^2-t)\\ &+t(t(4m_\chi^2-t)+(s-u)^2)+2tm_\Delta^2(t-4m_\chi^2)+m_\Delta^4(4m_\chi^2-t)],\end{aligned} \tag{4.58}$$

where t, s, and u are the standard Mandelstam variables. The final differential cross section in the lab frame is

$$\frac{d\sigma}{dE_R} = -\frac{1}{8\pi}\frac{m_N|\mathcal{M}|^2}{\lambda(s,m_\chi^2,m_N^2)}, \tag{4.59}$$

where E_R is the energy of the recoiling Δ, and λ is

$$\lambda(m_1,m_2,m_3) = m_1^2+m_2^2+m_3^2-2m_1m_2-2m_2m_3-2m_1m_3. \tag{4.60}$$

We plot both an example of the differential cross section in Fig. 4.14 and a comparison of the total cross section with NCE nucleon scattering in Fig. 4.15.

This process produces a Δ^+ (Δ^0) for proton (neutron) scattering. The produced Δ's decay to πN nearly 100% of the time, but we must refer to the isospin of the Δ^+, Δ^0 and that of their possible decay products to calculate the π^0 production rate [184]. Conveniently, both the Δ^+ and Δ^0 produce a π^0 with a branching ratio of $\frac{2}{3}$. When plotting the scattering rates for $\chi N \to \chi\Delta$ resulting inelastic pion production, this branching fraction is included.

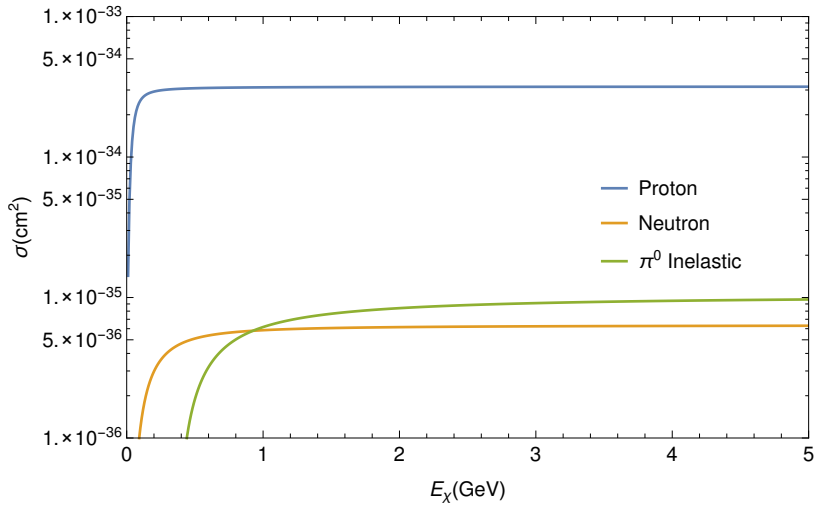

Figure 4.15: A comparison of the integrated cross section for neutral-current elastic nucleon scattering and inelastic delta production with $m_\chi = 0.01$ GeV, $m_V = 0.1$ GeV, $\kappa = 10^{-3}$ and $\alpha' = 0.1$.

Chapter 5

The BdNMC Simulation

5.1 Introduction

The earliest version of the **BdNMC**[1] software was written by Brian Batell, who implemented basic kinematics and electron scattering, and was revised and expanded by the author of this dissertation, with work beginning in late 2013. The initial objective of the software package was to provide the MiniBooNE collaboration with a means of simulating the expected hidden sector dark matter signal distribution over a range of model parameters. It has expanded beyond the scope of that initial objective, and can now be configured for a wide array of different fixed target geometries, and over a dozen production channels at a variety of energies. In addition, it supports four possible scattering interactions between hidden sector dark matter and the material in fixed target neutrino detectors..

In this chapter, we will document the most important features of the BdNMC software and their usage. We begin with a simple example set-up and an overview of code. A guide to formatting the parameter files used to customize a run of the code follows in Section 5.2, with documentation of all of the options available. Following this are further sections detailing the structure of the code and the simulation loop. These are not required reading for use of the code, but should be some assistance if you wish to modify the code. Section 5.3 covers the dark matter four-vector generation process, 5.4 briefly looks at signal calculation, 5.5 provides a schematic of the simulation loop, 5.6 documents the calculation of the total event rate and 5.7 documents the formatting of the simulation's output. We end with an overview of some

[1] Available at https://github.com/pgdeniverville/BDNMC

numerical implementation details in Section 5.8 and the detector geometry handling in Section 5.9.

5.1.1 An Example Experiment

Fixed target neutrino experiments generate neutrino beams by impacting high intensity proton beams into thick targets. The interactions of the protons with the nuclear material of the target produce enormous numbers of secondary particles, with pions chief among them. These secondary particles then decay, producing a beam of neutrinos. The interactions of these neutrinos are detected some distance away through their scattering off of nucleons and electrons. We provide a very simple example setup for one such experiment in Fig. 5.1.1 and Table 5.1.1, and will refer to this setup for examples while introducing the code. Note that while we call the experiments fixed target neutrino experiments in this section, our discussion could also be applied to a beam dump experiment such as SHiP.

In Chapter 4, we discussed the many means by which these experiments could both produce and subsequently detect a beam of dark matter particles. In our example, interactions between the target and the proton beam could lead to production of π^0's, whose radiative decays lead to the production of V's that rapidly decay to a pair of

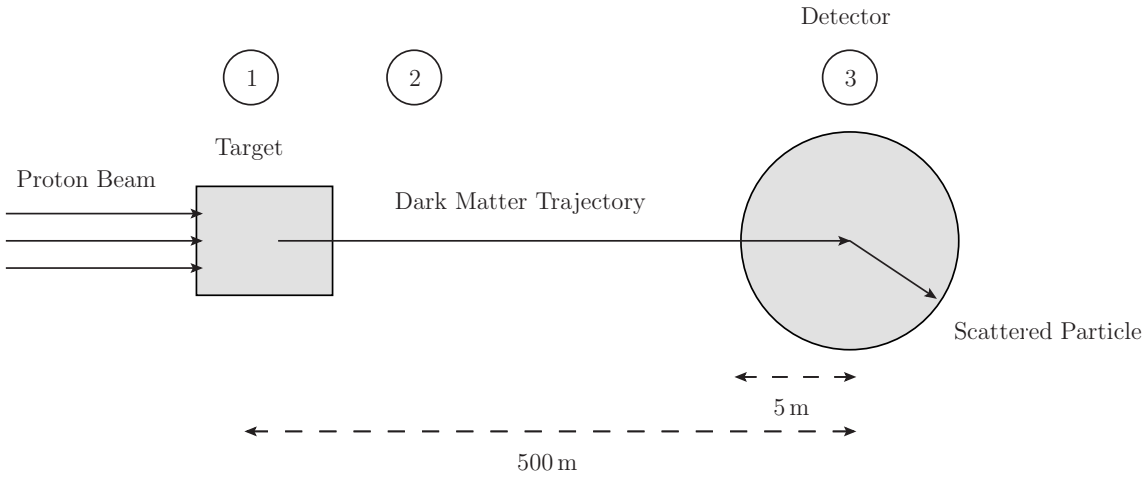

Figure 5.1: A diagram of dark matter production at a very simple fixed target neutrino experiment with geometry and beamline similar to that found at the MiniBooNE experiment. The detector is a sphere with a radius of 5 m filled with CH_2, located 500 m from the centre of the target. Most of the 500 m between the target and the detector is expected to be filled with dirt and other dense materials. Dark matter and neutrinos are produced through the interactions of an 8.9 GeV pr1oton beam impacting on the target. Integer labels refer to steps found in Fig. 5.1.2.

Parameters of the Example Experiment			
Protons on Target	2×10^{20}	Beam Energy	8.9 GeV
Production Channel	$\pi^0 \to \chi\chi\gamma$	π^0's per POT	0.9
Production Distribution	Sanford-Wang	Signal Channel	$N\chi \to N\chi$

Table 5.1: Alongside Fig. 5.1.1, this table provides a minimal set of parameters describing a simple fixed target experiment and the hidden sector dark matter scenario to be tested.

Example Model Parameters			
ϵ	10^{-3}	α'	0.1
m_χ	10 MeV	m_V	100 MeV

Table 5.2: A sample set of model parameters for use with our example experiment setup.

dark matter particles. All of this occurs on a time scale many orders of magnitude smaller than a nanosecond, the best timing resolution we could reasonably expect from a fixed target neutrino experiment, so we can assume that the initial π^0 and intermediate V do not propagate a significant distance before decaying, and the entire chain of events occurs within the target. The dark matter particles then propagate along straight-line trajectories, some of which will intersect with the neutrino detector. As the dark matter possesses very weak interactions with Standard Model matter, the number which scatter during this propagation is negligible compared to the total number produced. These particles could then interact in the neutrino detector by scattering off of nuclei or electrons, producing detectable scattering signals.

The most basic goal of the code is to calculate the number of dark matter signal events that would be observed over the lifetime of an experiment. One could perhaps calculate this with a series of integrals, but the complexity of the kinematics would make this quite difficult. For example, in the case of dark matter production via π^0's, one would need to account for the distribution of the initial angle of emission and momentum of the produced π^0's, the multistep decay chain resulting in the production of dark matter particles, and then place appropriate cuts on the domain of integration to account for the acceptance of the neutrino detector.

An alternative solution is to simulate the production and scattering of dark matter using Monte Carlo methods. In a Monte Carlo simulation, we randomly generate events from the underlying distributions (such as the momentum and angle distribution of the produced π^0's, or the differential cross section of neutral current elastic

dark matter nucleon scattering), and by aggregating large numbers of such events we can calculate an approximate signal rate. Furthermore, by generating individual dark matter production and scattering events, our code will be far easier to integrate with the simulations maintained by experimental collaborations. It is likely, for example, that an experimental collaboration possesses their own beamline simulation for the production of pions, and instead of generating pions from some phenomenological parameterization, we could use a list of pions supplied by the experimental collaboration, improving the accuracy of our signal calculation.

We will now move onto a high level overview of the components of the code. The code is written in C++ and makes significant use of inheritance in the implementation of the different production modes, scattering channels and detector geometries. Library data structures (e.g. `<vector>` and `<list>`) are used where possible. It employs the C++11 standard in order to take advantage of several libraries formerly found in the Boost C++ Libraries, in particular the random number generator supplied by `<random>` and memory management of `<memory>`.

5.1.2 Overview

A The simulation is run by calling the `Source/main` program. It accepts a single argument, a file path denoting the location of a parameter file. If no argument is provided, a default parameter file, `parameter.dat`, is loaded instead. The parameter file contains a list of parameters describing the desired run configuration. A comprehensive list of the arguments that may be provided in the parameter file will be given in Section 5.2, and we provide an example parameter card for our example setup at the end of that section. All of the valid parameter arguments are stored as variables in a `Parameter` object. After reading the parameter file, the code initializes variables describing the run (e.g. the number of events to generate, the output file to which events are to be written), the physics model (e.g. the mass of the dark matter candidate and vector mediator) and `Detector`. For our example experiment, our `Detector` would be a sphere with a radius of 5 m located 500 m from the center of target (also our origin).

1 Next, a list of the production channels is created, each element comprising an initial momentum distribution of primary beam products, `Distribution`, and a `DMGenerator` to decay those particles into dark matter pairs. In addition, a `Scatter` object is initialized to handle the interactions between the dark matter

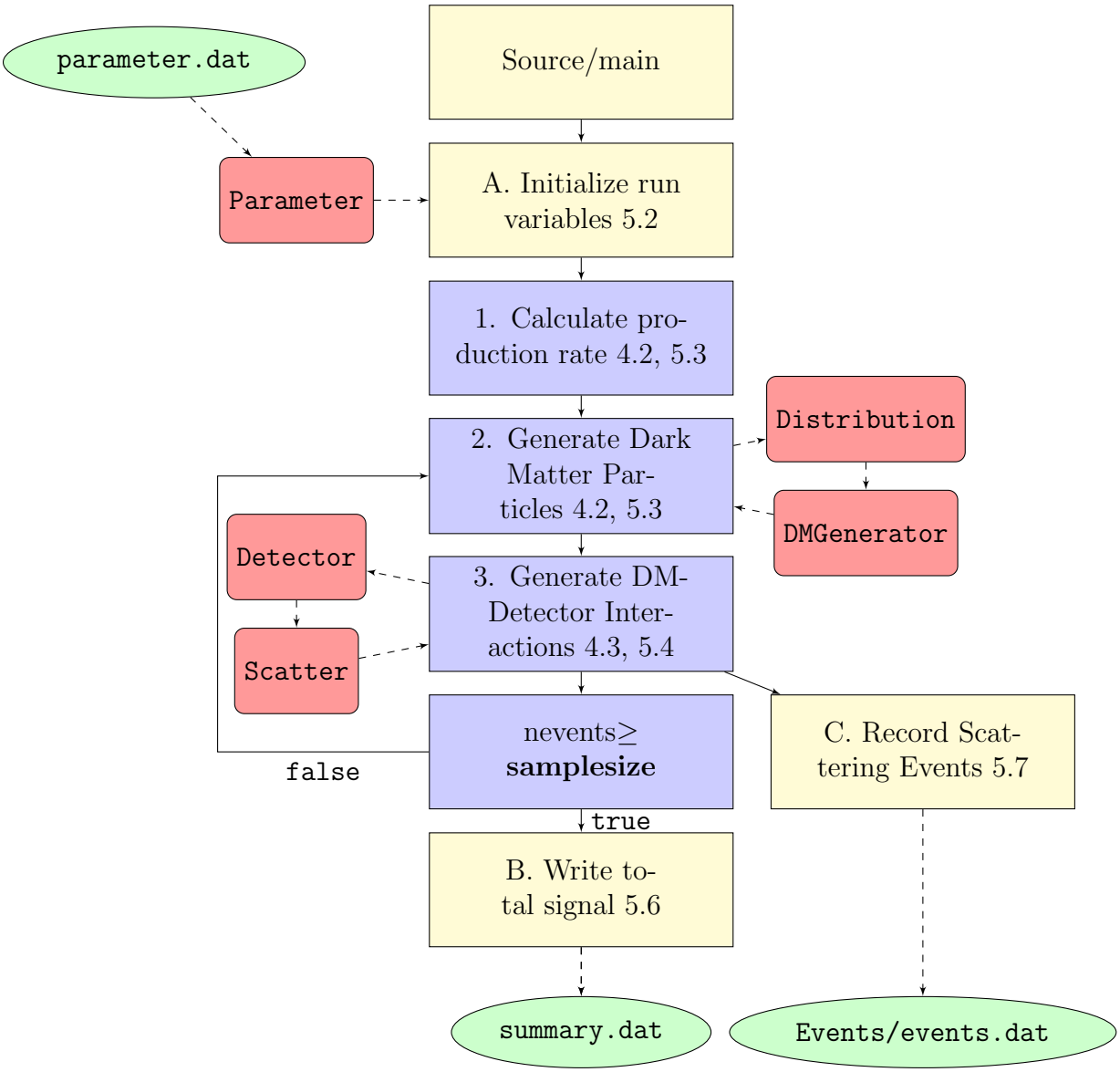

Figure 5.2: Schematic outline of the simulation code.

and the detector material. At this time, we calculate the total number of dark matter particles that is expected to be produced for a number of Protons on Target (POT) through each production channel in the list. The exact equations differ by production channel, and are described in 5.3.

In the example experiment, our list of production channels would have only one element. We would need to create a Sanford-Wang `Distribution` for an 8.9 GeV proton beam and a `DMGenerator` to simulate the decay chain $\pi^0 \to \gamma V \to$

$\gamma\chi\bar{\chi}$. The total number of dark matter particles produced would be equal to

$$N_\chi = \textbf{POT} \times \textbf{pi0\_per\_POT} \times \mathrm{Br}(\pi^0 \to \chi\chi^\dagger\gamma), \tag{5.1}$$

where **pi0_per_POT** is the number of π^0's produced per POT. For a MiniBooNE-like experiment, this is approximately 1. The `Scatter` object is created to handle neutral current-like elastic scattering between a nucleon and a dark matter particle with no cuts imposed on the outgoing energy and angle of the nucleon.

2 The simulation loop begins by selecting a production channel from the list generated in the previous step. Each channel has a probability of being chosen equal to fraction of the total number of dark matter particles that would be produced through the channel. The `Distribution` corresponding to that production channel generates the four-momentum of a meson or V produced by the interactions of the proton beam with the target. This generation is accomplished through rejection sampling using some differential particle production cross-section or by iterating through a pre-generated list of particle four-momenta. This initial particle is decayed by the `DMGenerator`, outputting a pair of dark matter particle four-momenta. The length of the intersection between these dark matter trajectories and the detector are calculated (see 5.9), and if either are found to be non-zero, then the initial meson or V and the intersecting dark matter particle(s) four-momenta are stored in a list and the code continues to step 3. More commonly, no intersection is found, and we return to the beginning of step 2 to choose another production channel.

In our example, we only have a single production channel to choose from, π^0 decay. The `Distribution` generates a momentum and emission angle for a π^0 from the Sanford-Wang distribution using rejection sampling (see 5.8.1). This initial 4-momentum is handed off to our `DMGenerator`, which decays this particle into a photon and a V, and then decays the V into two dark matter particles. A list of the initial π^0 and all the products is returned. All of these processes are assumed to occur at the origin, which defaults to the centre of the target. Only the dark matter particles will propagate outward. The two dark matter trajectories are passed to the spherical `Detector` object's `Ldet` member function, which uses the algorithm described in Section 5.9.1 to check for the length of intersection between their trajectories and the detector geometry.

3 Once a dark matter four-momentum is found to intersect with the detector, it is passed to the `Scatter` object's `probscatter` member function. The code first determines whether a dark matter scatters at all by calculating the ratio of the interaction probability of this particular dark matter particle to the maximum possible interaction probability,

$$R = \frac{\sigma(E_i) \times L_i \times n}{\text{MAX}(\sigma \times L \times n)}, \tag{5.2}$$

where $\sigma(E_i)$ is the interaction cross section for an incident dark matter particle with some energy E_i, L_i is the length of the intersection between the dark matter trajectory and the detector, and n is the number density of the particle with which our dark matter is interaction. The denominator is the largest interaction probability encountered thus far. A uniform random number $u \in [0, 1]$ is generated, and if $u < R$, no interaction occurs and the dark matter particle is discarded. If an interaction does occur, then an acceptance-rejection algorithm is used to generate a final state four-momentum by sampling from a differential distribution of the interaction cross section. This particle is added to the list generated in step 2, and the number of recorded interactions is incremented.

Continuing with our example, dark matter particles that intersect with the detector are passed on to the `Scatter` object, which first determines whether an NCE nucleon dark matter scattering event occurs at all, followed by the generation of an outgoing nucleon by selecting an energy from the differential nucleon dark matter scattering cross section through rejection sampling (The scattering angle is uniquely determined by the outgoing energy). If a scattering event occurred, the outgoing nucleon is added to list of particles generated in step 2.

B After the requested number of sample signal events have been generated, the total event rate is calculated as detailed in 5.6. This, along with other details of the run described in 5.7, is appended to the summary file.

C For each successful interaction, the four-momentum of the recoil particle is recorded in an events file with the format described in 5.7.

5.2 The Parameter File

The parameters of the experimental setup and the dark matter scenario to be studied are set in a parameter file supplied to the main code at the beginning of the run. Parameters are supplied in <**parameter_name**> <`value`> pairs, where valid values may be keywords, real numbers or integers. There is some basic error handling to catch improperly formatted parameters and notify the user, but as it has not been extensively tested, parameter files should be written with care. The simulation uses meters, seconds and GeV, except where otherwise noted, and all parameters should be supplied in these units. Any line that begins with # is treated as a comment, and is ignored by the parser. Note that many parameters possess default values that are used if they are not explicitly defined.

5.2.1 Metaparameters

These describe details of the run itself, as well as where to record the results.

burn_max The number of scatterings to perform during burn-in. Default is 1000.

burn_timeout The simulation will perform **burn_max**×**burn_timeout** burn-in loops before terminating the burn-in phase and moving on to the simulation run. This should probably be combined with a max_trials to ensure that a run will terminate in a reasonable amount of time. Default is 2×10^4.

max_trials An optional upper limit on the number of times the main simulation loop will run as counted by the `trials` variable. Default is -1, which causes the code to act as if there is no maximum.

output_file The filepath to which the event summary should be written when the simulation is set to comprehensive mode.

output_mode This determines what should be written to files during and after the run. Can be set to **comprehensive** or **summary**. Defaults to **comprehensive**.

run Every run is labelled by a string. If no run name is supplied, an integer run number will be generated from the current time.

samplesize The number of scattering events to generate before terminating the run. The code will throw an error if this is not set.

seed Choose the seed to supply to the random number generator. A seed based on the current time is generated if no seed is supplied.

summary_file The filepath to which a summary of the run should be appended.

5.2.2 Experiment setup

Parameters describing the target and proton beam of the experiment.

atomic_mass_target Not currently used for any physics.

beam_energy The total energy of the proton beam. Defaults to 8 GeV.

dm_energy_resolution The step size to use when creating an interpolation function for the scattering cross section. Should be varied before starting a large batch of runs to check if it sufficiently small. Defaults to 0.1 GeV, which may not be small enough for low energy experiments like LSND.

efficiency This is an overall factor which accounts for the percentage of signal events the experiment successfully detects and for any differences between the detector's fiducial volume and the geometry used in the simulation. Defaults to 1.0.

e_num_target The number of electrons per atom in the target. Not currently used.

pi0_per_POT The number of π^0's expected per proton on target. As many of the other meson production estimates are scaled relative to that of the π^0, it is important to have a good estimate of this quantity. Defaults to 0.9, which is appropriate for MiniBooNE on-target.

max_dm_energy Used in creating interpolation functions for scattering cross sections. This can be safely set equal to the beam energy as an upper limit, at the cost of slowing the initialization of the simulation slightly. Defaults to **beam_energy**.

max,min_scatter_angle Cuts on the scattering angle of the outgoing particle in an interaction event. This defaults to 2.1π radians and 0.0 radians respectively, which amounts to no cut on the angle.

max,min_scatter_energy Place cuts on the energy of the outgoing particle in an interaction event. Defaults to 10^9 GeV and 0.0 GeV, respectively.

n_num_target The number of neutrons per atom in the target. Defaults to 0.

n_density_target The number density of atoms in the target. Defaults to 0.

p_num_target The number of protons per atom in the target. Defaults to 0.

POT The total number of protons on target over the duration of the experiment. This value must be supplied or an error will be thrown.

proton_target_cross_section The total scattering cross section of protons on the target. Used to normalize the V production rate for partonic V production. Defaults to 0.

signal_channel Which scattering channel to use. Choose one from: **NCE_nucleon**, **NCE_nucleon_baryonic**, **NCE_electron** and **pion_inelastic**[2].

target_length The length of the target in meters. Default is 0.

timing_cut The length of the time delay required to register as an event. This currently calculates a timing efficiency

$$t_{\text{efficiency},i} = \begin{cases} 1 & t_{\text{delay},i} \geq t_{\text{cut}}, \\ \frac{t_{\text{cut}} - t_{\text{delay},i}}{t_{\text{cut}}} & t_{\text{delay},i} < t_{\text{cut}}, \end{cases} \tag{5.3}$$

where $t_{\text{delay},i}$ is the delay between the travel time of a neutrino moving between the target and the detector at c and a dark matter particle. The mean of 5.3 over all dark matter particles i produced by a given production channel is used to calculate the timing efficiency of that channel, and the total signal is multiplied by this efficiency to determine the event rate after timing cuts. The default value is 0.0, which results in a timing efficiency of 1.0.

[2]Note that coherent nucleon scattering is not currently supported in the code. This was added in a fork of the code specifically built for a coherent dark matter scattering paper[22], and was not folded back into the primary code. This should be added again at a later date.

5.2.3 Model

The model itself is determined largely by the choice of production and signal channels. A few overall parameters must be set no matter which production or signal channel is chosen.

alpha_D The dark sector coupling strength $\alpha' = \frac{\epsilon'^2}{4\pi}$, or in a baryonic model, α_B.

dark_matter_mass The mass of the dark matter candidate χ

dark_photon_mass The mass of the V mediator.

epsilon The mixing constant ϵ between the V mediator and the photon.

kappa See **epsilon**.

5.2.4 Production Channels

Any number of production channels may be specified in the parameter file. A production channel declaration begins with **production_channel** <`channel name`>, where the channel names currently supported are:

- **pi0_decay**, **pi0_decay_baryonic**,
- **eta_decay**, **eta_decay_baryonic**,
- **omega_decay**, **omega_decay_baryonic**,
- **rho_decay**,
- **phi_decay**, **phi_decay_baryonic**,
- **pi-minus_capture**,
- **parton_production**, **parton_production_baryonic**,
- **V_decay**, **V_decay_baryonic**.

Note that **rho_decay**, **omega_decay**, and **omega_decay_baryonic** should not be used with either of the proton bremsstrahlung production channels, as this would result in double counting due to the significant overlap in V production sources. All

non-π^0 decay channels require that **meson_per_pi0** be defined. This quantity is dependent both on the originator meson and the beam energy.

Following the production channel declaration, an optional production distribution can also be specified using **production_distribution** <`distribution name`>. Several of these distributions accept additional parameters, which must follow the **production_distribution** declaration in the parameter file. We now list the currently accepted distributions along with any additional parameters they accept.

- **pi0_sanfordwang**,

  distribution_parameter_file This is the filepath to a parameter file listing new values for variables **c1** through **c9** and **d1** through **d9**, as well as the **Beam_Energy** (which overrides any **beam_energy** listed in the main parameter file) and **maximum_pi_momentum**. This should be formatted in the same manner as the initial parameter file. Note that the **c** parameters are for the π^+ fit, and the **d** parameters are for the π^- fit, where the variable names correspond to those found in the MiniBooNE paper on the topic [185]. This file is parsed in the same manner as the main parameter file and any parameter names that it does not expect will be saved with their values, but otherwise ignored.

  sanfordwang_parameter_file Alternative parameter name for **distribution_parameter_file**.

- **k0_sanfordwang**

  distribution_parameter_file This is the filepath to a parameter file listing new values for variables **e1** through **e8** for the $K0$ fit in [185], where we have switched **c** from the paper for **e**. Otherwise handled identically to **pi0_sanfordwang**.

  sanfordwang_parameter_file Alternative parameter name for **distribution_parameter_file**.

- **particle_list**,

  particle_list_file The file path to a text list of particle four-momenta in the format `px py pz E`. Optionally, each can be appended with an additional four-vector describing the space-time starting position for each particle,

resulting in the format `px py pz E x y z t`. Note that the z-axis is oriented parallel to the beam direction.

particle_list_position Supply true to indicate to the parser that particle positions should be expected. Any other argument will default to false.

- **burmansmith**, this channel requires some target parameters to be set, specifically **p_num_target** and **n_num_target**.
- **bmpt**, this channel also requires **p_num_target** and **n_num_target** to be set.
- **parton_V**, **parton_V_baryonic**

  parton_V_neutron_file A file path to a text list of pairs of V momenta and differential V production cross sections $\frac{d\sigma_{pn\to V+X}}{dE_V}$ listed in microbarns per GeV. Note that the V momenta must be supplied with a constant step size.

  parton_V_proton_file As **parton_V_neutron_file**, but for $\frac{d\sigma_{pp\to V+X}}{dE_V}$.

- **proton_brem**, **proton_brem_baryonic**. These channels should be paired with **V_decay** and **V_decay_baryonic** respectively, as they produce on-shell V's which decay isotropically.

  ptmax The maximum transverse momentum which a produced V mediator may possess. The minimum is assumed to be 0.

  zmin The minimum value of $z = \frac{p_{V,z}}{P}$, where $p_{V,z}$ is the momentum of the V parallel to the z axis, and P is the total momentum of a beam proton incident on the target. See 4.2.3 for details on choosing these parameters.

  zmax The maximum value of z, defined as in the **zmin**.

5.2.5 Detector Parameters

The detector parameters describe the location, size, and material of the detector. In the current version of the code, only one detector may be declared. The detector declaration begins with **detector** <shape>, where <shape> can be **sphere** or **cylinder**. After this command, the parameter parser will expect the dimensions of the detector to be supplied, as well as a list of materials which reflect its composition. It will accept further commands describing the detector until it encounters a non-detector

variable, at which point it will return to regular parsing. For a spherical detector, the center of the detector needs to be supplied using **x-position**, **y-position**, and **z-position**, as well as the **radius**. For a cylindrical detector, the **length** must also be defined, as well as its orientation. The orientation defaults to the length of the cylinder aligned parallel to the z-axis, and it is rotated to other orientations by an angle θ by rotating about the x-axis, and then an angle ϕ by rotating about the y-axis, supplied using **det-theta** and **det-phi**, respectively.

A material is defined by providing a **material** <name>, and then providing the **number_density** in particles per cm^3 (Note that this is one of the few areas where we do not use meters), **proton_number**, **neutron_number**, **electron_number** and **mass** in GeV.

5.2.6 Parameter File Example

We provide here a simple parameter card for out MiniBooNE-like example experiment detailed in 5.1.1. For a more complicated card that implements a run with multiple production channels, see Appendix B.

```
#Parameter Card
#All masses should be provided in GeV, all lengths in meters.
#Lines preceded by a # are ignored by the parser.

#Model Parameters
epsilon 1e-3
dark_matter_mass 0.01
dark_photon_mass 0.1
alpha_D 0.1

#Run parameters
POT 2e20
pi0_per_POT 0.9
samplesize 2000
beam_energy 8.9



#Production Parameters
```

```
production_channel pi0_decay
production_distribution pi0_sanfordwang

#Scattering Parameters
signal_channel NCE_Nucleon

output_mode comprehensive

#Where to write events and summary information.
output_file Events/events.dat
summary_file Events/summary.dat

#Detector Parameters
detector sphere
x-position 0.0
y-position 0.0
z-position 500.0
radius 5.0

#Material parameters
material Carbon
number_density 3.63471e22
proton_number 6
neutron_number 6
electron_number 6
mass 11.2593

material Hydrogen
number_density 7.26942e22
proton_number 1
neutron_number 0
electron_number 1
mass 0.945778
```

5.3 Dark Matter Production

Dark matter production involves the generation of some initial particle from a production distribution (handled by the `Distribution` class), and its decay to dark matter and subsequent propagation to a detector (handled by the `DMGenerator` class). As multiple production channels often contribute to dark matter production simultaneously, a list of production channels is prepared, each with its own `Distribution` and `DMGenerator`, and the number of dark matter particles produced by each channel, `vnum[i]` (see 5.3.2), is calculated in advance. This process can be broken into a few steps:

- A production channel i is chosen randomly from the previously mentioned list with a probability
$$Prob(i) = \frac{\texttt{vnum[i]}}{\texttt{vnumtot}}, \tag{5.4}$$
where $\texttt{vnumtot} = \sum_i \texttt{vnum[i]}$.

- Some initial particle must be generated from a sample distribution that describes particle production in proton-target collisions. This is handled by the `Sample_Particle` member function supplied by `Distribution`, which assigns a `Particle` object a four-momentum drawn from some internal production distribution using rejection sampling, or from a list of four-momenta supplied from some text file. This initial particle becomes the first element of a list of particles.

- The list of particles containing the initial particle created by the `Distribution` is passed to the `DMGen` member function of the `DMGenerator` object. This function will decay the initial and all subsequently produced particles until the four-momenta for dark matter particles are generated. These dark matter four momenta are checked for intersection with the detector using the `LDet` member function of the `Detector` defined during initialization. If non-zero intersection is found, all of the produced particles are added to the supplied list of particles and the function returns `true`, indicating that the simulation should now attempt to generate a scattering.

The `Particle` Class

The `Particle` class encodes all of the salient details about a particle and provides a number of methods to calculate and set useful quantities. The most important

variables are:

- `px, py, pz, E`, the four-momentum.
- `m`, the particle mass
- `name`, a string identifying the particle. During the simulation loop, the code will look for particles named "DM" in order to propagate them to the detector and attempt to scatter them.
- `origin_coords, end_coords`, two `double[4]` arrays which record the origin point and time of the particle and where and when it was destroyed, either by decaying or scattering. The position is stored in the elements 0 to 2, and the time in element 3. This is only truly important for the dark matter at the current time, as `end_coords` records where in the detector and the time at which it scattered.

The most important methods include:

- `void Lorentz(Particle& part)`, perform a Lorentz boost on the `Particle` from the rest frame of `part` to the lab frame.
- `void Set_Time(double t)`, calculate the `end_coords` by propagating from `origin_coords` in the direction of the four-momentum of the `Particle` for `t-origin_coords[3]` seconds.
- `void ThreeMomentum(double PX, double PY, double PZ)`, set the three-momentum `px, py, pz` of a `Particle` with mass `m` to the supplied momenta, and then calculates the energy `E`.

5.3.1 Production Distributions

The `Distribution` Class

All of the distributions in the code inherit the `Distribution` class, which requires the implementation of a single function:

- `sample_particle(Particle& part)` generate a four-vector for some initial particle produced through the interactions of the proton beam and the target, ideally according to some distribution function or a supplied list of four-vectors.

The implementation of this is entirely dependent on the distribution selected. An estimate of the maximum value of the distribution is required for rejection-sampling, and as this is normally not known before run-time, each distribution will perform a short burn-in run by generating $\sim 10^4$ sample particles upon initialization. The `sample_particle` method automatically updates its estimate of the maximum value of the production cross section each time it generates an acceptable four-momentum[3].

In addition, as it is not guaranteed that a `Distribution` object will know the mass of the particle it is generating, we can indicate this at a later time by using the `set_mass(double)` member function.

Pion Distributions

The Sanford Wang and BMPT distributions both generate a pair of candidate angle θ_i and momentum p_i variables using a uniform random number drawn from the kinematically allowed regime. The differential production cross section $\sin(\theta)\frac{d^2\sigma}{d\theta dp_\pi}(\theta, p_\pi)$ is compared with MAX $\left(\sin(\theta)\frac{d^2\sigma}{d\theta dp_\pi}\right)$ for use in rejection sampling. Once a particle has been accepted, an angle ϕ is generated by drawing a uniform random variable from the range $[0, 2\pi)$. The Burman-Smith distribution is used in a similar manner, but samples π kinetic energy instead of momentum.

Direct V production

The partonic V distribution produces V mediators directly from quark level interactions in the colliding nuclei rather than through intermediate particles. This calculation requires knowledge of Parton Distribution Functions that are not included in the simulation, and is currently handled by an external code written by David McKeen [66]. This code supplies two csv files containing $\frac{d\sigma_{pN\to V}}{dp_V}$ for proton-proton and proton-neutron collisions for a given beam energy and V mass. The `parton_V_gen` class constructs interpolation functions based on these files, and uses acceptance rejection sampling to generate V momenta. The total V production cross section $\sigma_{pN\to V+X}$ can be calculated by summing over the numerical data. As described earlier in 4.2.5, each V is created with a momentum parallel to the proton momentum (likely along the z-axis).

[3]This does not apply to Particle Lists, which simply iterate through the list of particle 4-momenta that have been supplied.

The **proton_brem** distribution samples V four-momenta from the proton bremsstrahlung equation 4.11, where the maximum value is known to be

$$\text{MAX}\left(\frac{d^2N_V}{dzdp_\perp^2}(z,p_\perp)\right) = \frac{d^2N_V}{dzdp_\perp^2}(\mathbf{zmin},0). \tag{5.5}$$

Particle Lists

One final option is to use a particle list distribution. Rather than sampling from a distribution, this reads a list of four-vectors from a text file, and stores it in a `list`. Each time `sample_particle` is called, it iterates one step through the list, constructs a particle based on the four-momentum, and returns it. A position and timing distribution can also be supplied by appending a four-vector to each four-momentum in the supplied text file. This is especially useful when particles are supplied by a beamline simulation, as different portions of the target and surrounding materials are likely to exhibit different momentum distributions.

5.3.2 Dark Matter Generation

The `DMGenerator` Class

Once a `Distribution` has returned an initial particle, a `DMGenerator` object is tasked with simulating the chain of decays which will result in the production of dark matter. Each dark matter production channel is implemented through a class is derived from `DMGenerator`. The most important member variables of `DMGenerator` are:

- `mv, mx, kappa, alphaD`, the parameters describing the hidden sector dark matter scenario.
- `chan_name`, a string storing the name of the production channel. As an example, the $\pi^0 \to \gamma\chi\bar{\chi}$ channel is called "pi0_decay".
- `branchingratio`, the probability that the decay process will occur. For direct V production channels this will be nearly 1 so long as invisible decays dominate.

Classes that are derived from `DMGenerator` must implement two member functions:

- `bool DMGen(list<Particle>& plist, function<double(Particle)> det_int, Particle& initial_part)` uses the `initial_part` supplied by

`Distribution` to generate a pair of dark matter particles through some chain of decays. The produced dark matter particles (always a pair in the current code) are checked for intersection by `det_int`, the function `Ldet` supplied by the `detector` class (see 5.9). If a non-zero intersection is recorded, all of the particles involved in the production of the dark matter particle are saved, and the function returns `true`.

- `void Evaluate_Branching_Ratio()` calculates the branching ratio for the production channel and stores it in `branchingratio`. This is called automatically at initialization of `DMGenerator`.

The `DMGenerator` must be able to calculate the branching ratio for dark matter production, though the exact chain of processes is highly dependent on the production channel. Each production distribution is responsible for returning a branching ratio or some equivalent value which can be used to calculate `vnum`, the total number of V mediators produced by **POT** protons that will decay into dark matter particles. In a formula,

$$\texttt{vnum} = N_V \times \mathrm{Br}(V \to \chi\chi^\dagger), \tag{5.6}$$

where N_V is the number of V bosons generated.

Meson Decays

The most thoroughly studied production channel is that of pseudoscalar meson decay, in which we have some pseudoscalar meson X that decays radiatively as $X \to \chi\bar{\chi} + \gamma$. These production channels should be paired with one of the meson production distributions: Sanford-Wang, BMPT or Burman-Smith. For the on-shell case, in which $m_V > 2m_\chi$ and $m_V < m_X$, the decay is performed in two steps, first by decaying the meson, $X \to V + \gamma$, and then decaying the mediator, $V \to \chi\bar{\chi}$. The total branching ratio is a product of that of the two processes

$$\mathrm{Br}(X \to \chi\bar{\chi} + \gamma) = \mathrm{Br}(X \to V + \gamma)\mathrm{Br}(V \to \chi\bar{\chi}), \tag{5.7}$$

where $\mathrm{Br}(X \to V+\gamma)$ possesses an analytic form shown in 4.2.1 and $\mathrm{Br}(V \to \chi\bar{\chi}) \approx 1$ for large α'. The total `vnum` is calculated by

$$\texttt{vnum} = \mathrm{Br}(X \to \chi\bar{\chi}\gamma)\mathbf{meson\_per\_pi0} \times \mathbf{pi0\_per\_POT} \times \times \mathbf{POT}, \tag{5.8}$$

where **meson_per_pi0** = 1 for π^0. Each decay is isotropic in the parent particle's rest frame, and the momentum of the child particles is determined by

$$\lambda(m_1, m_2, m_3) = \frac{1}{2m_1}\sqrt{m_1^4 + m_2^4 + m_3^4 - 2m_1^2m_2^2 - 2m_2^2m_3^2 - 2m_3^2m_1^2}, \tag{5.9}$$

where m_1 is the parent particle, and $m_{2,3}$ are the daughter particles. After performing the $X \to V + \gamma$ decay, the V is Lorentz boosted from the X rest frame to the lab frame, and this process is repeated for the V and its daughter $\chi\bar{\chi}$ particles.

The process becomes more complicated in the off-shell case, as the decay can no longer be decomposed into two simple two-body decay processes. The branching ratio $\mathrm{Br}(X \to \chi\bar{\chi} + \gamma)$ does not possess an analytically form, and must be integrated numerically. The branching ratio is calculated as

$$\int_{4m_\chi^2}^{m_X^2} ds \frac{d\mathrm{Br}}{ds}(X \to V^* + \gamma \to \chi\bar{\chi} + \gamma), \tag{5.10}$$

where s is the center of mass energy of the V, and the integral is performed using Sinh-Tanh quadrature. At this point it should be noted that the previous paragraph on the handling of the on-shell case was not quite correct, as near threshold the off-shell contributions become competitive with the on-shell expression. As a result, the complete off-shell branching ratio is always calculated, and if off-shell corrections are found to be sufficiently large (as defined by $\mathrm{Br}(X \to \chi\bar{\chi} + \gamma) \geq 1.3 \times \mathrm{Br}(X \to V + \gamma)\mathrm{Br}(V \to \chi\bar{\chi})$), the off-shell machinery will be used.

The simulation of the off-shell decay uses rejection sampling on $\frac{d^2\mathrm{Br}}{dsd\theta}(X \to V^* + \gamma \to \chi\bar{\chi} + \gamma)$ to generate an (s, θ) pair, where θ is the angle between the χ and the z-axis in the rest frame of the V. The z-axis of this rest frame is aligned such that it is parallel to the V's momentum in the X's rest frame. In order to boost to the X rest frame, we first boost along the z-axis to match the V^* momentum, and then rotate the z-axis to be parallel to the V momentum in the X rest frame.

The simulation of vector meson oscillation is quite similar to that of the pseudoscalar meson decays, but the calculation of `vnum` is slightly different,

$$\texttt{vnum} = \mathrm{Br}(X \to \chi\bar{\chi})\textbf{meson\_per\_pi0} \times \textbf{pi0\_per\_POT} \times \times \textbf{POT}. \tag{5.11}$$

The kinematics of this process are simulated as an off-shell vector meson X oscillating into an on-shell V, which then decays normally into a $\chi\bar{\chi}$ pair. This channel is nor-

mally paired with a pion production distribution to generate a somewhat reasonable set of three-momenta from which to sample.

Direct V Production

The handling of partonic V production is quite a bit simpler, as we have only to decay the vector particle supplied by the distribution. The only complication is that the decay is not isotropic, but is instead drawn from[4]

$$g(\hat{\theta}) = \frac{3}{4}(1 - \cos^2(\hat{\theta})), \tag{5.12}$$

where $\hat{\theta}$ is the angle between the dark matter momentum and the beam direction [15]. The V production rate is calculated using the assumption that experiments are designed to have the majority of their beam protons interact with target material, and so N_V should be proportional to the ratio of the total proton-material cross section to the V production cross section,

$$N_V = \frac{\sigma_{pA\to V+X}}{\sigma_{pA}} \times \mathbf{POT}, \tag{5.13}$$

where σ_{pA} is the total proton scattering cross section with some material of mass number A.

Proton bremsstrahlung is handled in a similar manner, but the V mediators are decayed to dark matter isotropically. The total number of V's produced is calculated as

$$N_V = \mathbf{POT} \int_0^{\mathbf{ptmax}^2} dp_\perp^2 \int_{\mathbf{zmin}}^{\mathbf{zmax}} dz \frac{d^2 N_V}{dz dp_\perp^2}, \tag{5.14}$$

where $\frac{d^2 N_V}{dz dp_\perp^2}$ is defined in 4.11.

5.4 Signal Channels

Once a dark matter particle's four-momentum has been found to intersect with the experiment's detector, it is passed on to the `Scatter` object through the `probscatter` member function. The `Scatter` object determines whether an interaction occurs, and if so, generates the final state particles produced by the scattering.

[4] In the case of fermionic dark matter, this would be $\left(\cos\hat{\theta}\right) = \frac{3}{8}\left(1 + \cos^2\hat{\theta}\right)$

The `Scatter` class

Dark matter signal calculations are handled by the `Scatter` class. Each signal channel is implemented as a class derived from `Scatter`, and they all share the following variables

- `MDP, mdm, alD, kap`[5], the model parameters.
- `pMax`, the maximum scattering probability encountered.
- `Escatmax, Escatmin, min_angle, max_angle`, kinematic cuts on outgoing particles. The range of acceptable angles defaults to $[0, 2\pi)$ unless otherwise indicated.

Scattering is handled by:

- `probscatter(shared_ptr<detector>& det, list<Particle>& partlist, list<Particle>::iterator& DMit)`, where `det` is a pointer to a `detector` object, `partlist` is the list of particles produced by `DMGenerator` (see 5.3.2) and `DMit` is an iterator pointing to the dark matter particle that is being checked for scattering. Should a scattering occur, a final state particle is generated and inserted into `partlist` as the element following the dark matter. More details are provided below.

For NCE nucleon scattering and inelastic π^0 production, the total interaction cross section includes one or more integrals which must be evaluated numerically. Upon initialization these `Scatter` objects will generate an interpolation function of its interaction cross section on both neutrons and protons over $E_\chi \in$ [0,**max_dm_energy**], where E_χ is the incident dark matter energy. Any cuts on the recoil energy for the NCE nucleon channels are implemented as limits on the range of integration during this step. This is unnecessary for NCE electron scattering, as a closed form exists for its scattering cross section. In addition, an interpolation function of the maximum value the differential cross section is found for both neutron and proton scattering over the same incident dark matter energy range using the minimization algorithm described in 5.8.2.

[5]This naming convention is not consistent with `DMGenerator`.

The probability that an elastic scattering will occur for dark matter particle χ_i is calculated by

$$p_i = \sigma_{\chi N, e\to\chi X}(E_{\chi,i}) \times L_{\mathrm{Det},i} \times n_{N,e}, \tag{5.15}$$

where $\sigma_{\chi N,e\to\chi X}$ is the integrated interaction cross section, $L_{\mathrm{Det},i}$ is as defined in 5.31 and $n_{N,e}$ is the number density of nucleons or electrons. The formula for inelastic pion production is similar,

$$p_i = \frac{2}{3}\sigma_{\chi N\to\chi\Delta}(E_{\chi,i}) \times L_{\mathrm{Det},i} \times n_N, \tag{5.16}$$

where the factor of 2/3 reflects the branching ratio of $\Delta \to \pi^0$ as opposed to $\Delta \to \pi^+$. An interaction is deemed to have occurred if the inequality $p_i > u\times$`pmax`, where as before u is a uniform random number drawn from $[0, 1]$.

Once a scattering has occurred, a final state particle observable by the detector must be generated. In every signal channel, an outgoing energy is generated through rejection sampling on the differential scattering cross section, with the enveloped set by the maximum value of the differential cross section. This maximum was calculated for all possible dark matter energies during initialization. Should it pass, a scattering angle θ relative to the incoming dark matter's momentum is generated for the scattered particle, followed by $\phi \in [0, 2\pi)$. While this particle is ready for output in the case of elastic scattering, there is one additional step in the inelastic π^0 channel: the decay $\Delta \to \pi^0\gamma$. This is handled in the same manner as the $\pi^0 \to \gamma V$ decay channel, but with different masses for the parent and massive daughter particles. Note that all scatterings are handled as if the dark matter was traveling parallel to the z-axis, all output particles are rotated to the lab frame after the scattering occurs.

For the elastic scattering channels, the particles generated through this process are guaranteed to pass any energy cuts as those cuts are included in the calculation of the total scattering cross section. This is not the case for inelastic π^0 production, as the end state is not as deterministic, and so any cuts on the outgoing π^0 momentum must be checked separately. In all cases, angular scattering cuts are checked afterwards by the `main` code before being accepted as scattering events.

5.5 The Simulation Loop

Before the simulation loop proper begins, a burn-in run is conducted for each production channel to estimate `pmax`. This is very similar to the simulation loop, but the end state interaction results are not generated, and the variable `nburn` is incremented each time. The burn-in run is conducted until `burntrials` is equal to `BURNMAX`. We provide a schematic of the loop here.

1. Set `trials`=0, `nevents`=0, `ninteractions = zeros(chan_count)`.
2. While `nevent` $\leq$ `samplesize`:
   (a) `trials`++.
   (b) Generate a uniform random number `vrnd` $\in$ [0,`vnumtot`].
   (c) Set $i = 0$, `scatterswitch=False`.
   (d) While $i <$ `chan_count`:
      i. If `vrnd` $<$ `vnum`$[i]$ then break
      ii. Else set `vrnd` = `vrnd` - `vnum`$[i]$.
   (e) Initialize `Particle part` with four-momentum `p`=0.
   (f) Set the four-momentum of `part` using `Distribution`'s `Sample_Particle` method.
   (g) Initialize an empty `list` of `Particles partlist`.
   (h) Append `part` to `partlist`.
   (i) Generate a list of decay product `Particles` of `part` using `DMGenerator`$_i$'s `DMGen` member function and store them in `partlist`.
   (j) For each dark matter `Particle` j in `partlist`:
      i. If `Ldet`$_j$ == 0 then continue
      ii. Else
         A. Simulate an interaction using `Scatter`'s `probscatter` method.
         B. If probscatter returns true, then insert the end state `Particle` generated by `probscatter` after j in `partlist`, and set `scatterswitch=True`.

(k) If `scatterswitch`, then write all the particles in `partlist` to **output_file**, `nevent`++ and `ninteraction`$_i$++.

3. end while loop

5.6 Calculating the Number of Signal Events

Signal events are particle interactions which pass all experimental cuts and are successfully identified (the later condition is represented by efficiency factors). The number of signal events reported by the code is an estimate of the total number of signal events that the experiment would observe given some number of protons on target, **POT**. The number of signal events is different from the number of sample events requested, as these are mere representative events generated to estimate the total signal. The signal rate from a given production channel i is calculated as

$$\texttt{signal\_events}[i] = \frac{\texttt{ninteractions}[i]}{\texttt{trials}} \times \texttt{vnumtot} \times \texttt{pmax} \times \textbf{efficiency}, \quad (5.17)$$

where `ninteractions` and `trials` are discussed in 5.5, `vnumtot` is found in 5.3.2, `pmax` is discussed in 5.4 and **efficiency** is a parameter mentioned in 5.2.2. The total signal rate is given by the sum

$$\texttt{total\_signal\_events} = \sum_{i}^{\texttt{chan\_count}-1} \texttt{signal\_events}[i]. \quad (5.18)$$

Only the total signal number is required to estimate an experiment's discovery potential for a given new physics scenario.

5.7 Output

In all modes, the simulation will append a summary of the results to the file path supplied for **summary_file** after completing a run. Each entry begins with `Run` **run**, and is followed by a number of lines equal to `chan_count` with the results for each channel in the format:

channel_name dark_photon_mass dark_matter_mass `signal_events`$[i]$ **epsilon alpha_D signal_channel POT Efficiency samplesize** `vnum`$[i]$

The summary output terminates with one final line with the format:

`Total` **dark_photon_mass dark_matter_mass** `total_signal_events` **epsilon alpha_D signal_channel POT Efficiency samplesize** `vnumtot`

The output expected for our example setup from 5.1.1 is provided here:

```
Run 1470677009
pi0_decay 0.1 0.01 4137.09 0.001 0.1 NCE_nucleon 2e+20 1 2000
Total 0.1 0.01 4137.09 0.001 0.1 NCE_nucleon 2e+20 1 2000
```

As a further example, we show a few runs for NCE nucleon scattering with **alpha_D**=0.1, **epsilon**=$10^{-}3$, **dark_matter_mass**=5 MeV and **dark_photon_mass**=0.4 GeV:

```
Run 1446004457
pi0_decay 0.4 0.005 0.00365517 0.001 0.1 NCE_nucleon 2e+20 1 5000
eta_decay 0.4 0.005 0.996236 0.001 0.1 NCE_nucleon 2e+20 1 5000
proton_berm 0.4 0.005 0.0154329 0.001 0.1 NCE_nucleon 2e+20 1 5000
Total 0.4 0.005 1.01532 0.001 0.1 NCE_nucleon 2e+20 1 5000
Run 1446086551
pi0_decay 0.4 0.005 0.00195789 0.001 0.1 NCE_nucleon 2e+20 1 5000
eta_decay 0.4 0.005 0.93881 0.001 0.1 NCE_nucleon 2e+20 1 5000
proton_brem 0.4 0.005 3.95397 0.001 0.1 NCE_nucleon 2e+20 1 5000
Total 0.4 0.005 4.89474 0.001 0.1 NCE_nucleon 2e+20 1 5000
Run 1446086747
pi0_decay 0.4 0.005 0.00120486 0.001 0.1 NCE_nucleon 2e+20 1 5000
eta_decay 0.4 0.005 0.490378 0.001 0.1 NCE_nucleon 2e+20 1 5000
proton_brem 0.4 0.005 1.51652 0.001 0.1 NCE_nucleon 2e+20 1 5000
Total 0.4 0.005 2.0081 0.001 0.1 NCE_nucleon 2e+20 1 5000
```

In **summary** mode, the summary file is the only output produced, discounting various status reports written to the terminal. While in **comprehensive** mode, the code also writes a report of all the particles which took part in each event to **output_file**. This file begins with the run name in the format `Run` **run**. Each event output is preceded by `event nevent`, where `nevent` is the number of events at the time which it was recorded. Next, each particle in the `partlist` for the given event writes a report of its four-momentum and, if it was the final endstate particle, the position where the signal interaction occurred in the format

```
particle_name px py pz E x y z t
```

Where `x y z t` are the optional position and time coordinates only shown for the signal particle. The particle reports are followed by the line `endevent nevent`.

Once again, we provide a sample output:

```
Run 1462311643
event 1
pion            0.285398        -0.0544237      5.54369         5.55294
V               0.204215        -0.0118137      4.14206         4.14832
DM              -0.00377294     -0.00148947     0.658276        0.658307
proton          -0.185011       0.235048        0.134491        0.993941
-2.82029        -1.11338        492.064         1.64143e-06

endevent 1

event 2
pion            0.0252685       0.113951        1.771           1.77997
V               0.039564        0.105479        1.71365         1.72026
DM              -0.00213871     -0.000317347    0.733531        0.733551
proton          0.205311        -0.208192       0.118041        0.989841
-1.42464        -0.21139        488.618         1.6299e-06

endevent 2

event 3
pion            -0.0597918      -0.0244405      5.17368         5.17585
V               -0.0199172      -0.0266187      4.24083         4.24214
DM              -0.0127331      -0.0416011      4.10137         4.1016
neutron         -0.305361       -0.15944        0.0761656       1.00362
-1.53362        -5.01059        493.984         1.64785e-06

endevent 3
```

Two of the scattering events occurred between dark matter and a proton, while the last one was a rare scattering off of a neutron. All three originated with relatively low energy π^0's.

5.8 Numerical Techniques

5.8.1 Rejection Sampling

The primary method used to sample cross-sections or momentum distributions is rejection sampling, also known as acceptance-rejection (see e.g. [186]). To draw samples from some distribution $f(\mathbf{x})$, we find some easily sampled enveloping distribution

$g(\mathbf{x})$ for which

$$g(\mathbf{x}) \geq \epsilon f(\mathbf{x}) \, \forall \mathbf{x}, \tag{5.19}$$

where ϵ is some real number chosen such that 5.19 is satisfied. We then execute the following loop:

1. Generate a uniform random number $u \in [0, 1]$ and an array of random numbers $\mathbf{x}$ from g.
2. If $u > \epsilon f(\mathbf{x})/g(\mathbf{x})$, return $\mathbf{x}$.
3. Else goto to step 1.

The simplest version of this algorithm, which is employed by the simulation code, is to set $g(\mathbf{x}) = \text{MAX}\,(f(\mathbf{x}))$, which allows us to generate $\mathbf{x}$'s using uniform random numbers over the domain of f. While crude, this sampling regime is quite effective for distributions of low dimensionality that are not sharply peaked. The code does sometimes encounter issues with peaked distributions, and a more adaptive sampling algorithm could be implemented to tackle them more efficiently if required, but it has thus far not been a significant issue.

In our example experiment, we use rejection sampling to generate a momentum p_{π^0} and an emission angle θ_{π^0} for a π^0 created in the target. For the Sanford-Wang distribution, this would be done by generating a random $p_{\pi^0} \in [0, 7]\,\text{GeV}$ and $\theta_{\pi^0} \in [0, \pi/2]\,\text{rad}$, as well as a uniform random number $u \in [0, 1]$. We then check

$$SW(p_{\pi^0}, \theta_{\pi^0}) > u \times SW_{\max}, \tag{5.20}$$

where $SW_{\max}$ is the maximum possible value of the Sanford-Wang distribution. Should 5.20 hold true, we return the p_{π^0} and θ_{π^0} that we found[6]. If it fails, we try again with a new set of numbers p_{π^0}, θ_{π^0}, and u, and repeat until 5.20 is satisfied.

5.8.2 Function Extrema

Rejection-sampling requires knowledge of the extrema of the sampled functions. This is often difficult to predict ahead of time. For example, the maximum value of the dark matter interaction with the detector is dependent on detector geometry, position and composition, beam energy, dark matter production mode and distribution, and

[6]We might also want to generate an azimuthal angle $\phi \in [0, 2\pi]$ at this point

experimental cuts on the recoil momentum and angle of an outgoing particle. In these cases the relevant maxima are initially set to zero, and then updated over time. A short burn-in period, where numbers, particles, or entire scattering events are generated but not used, precedes regular running to obtain a realistic estimate of the maximum of the distribution.

There are other cases, particularly in sampling the differential scattering cross sections, where this is far less feasible, as the differential scattering cross section's shape and maximum vary with the wildly with incident dark matter energy. For one dimensional distributions such as differential cross sections $\frac{d\sigma}{dE_R}$, the simulation code employs Golden Section Search [187]. This is not the fastest routine available, but it is straightforward, makes few assumptions about the shape of the function, and is sufficiently efficient to avoid noticeably slowing the simulation. Note that this is a minimization algorithm, so we will be minimizing the value of $f(x = E_R) = -\frac{d\sigma}{dE_R}$, and setting $f(x) = 0$ for all x outside of the kinematically allowed domain of the differential scattering cross section.

In our example case, we could use this algorithm to find the maximum value of the differential NCE nucleon dark matter scattering cross section[7]. This maximum value can then be used with rejection sampling by `Scatter` to generate a recoil energy for a scattered nucleon.

It should be noted that the minimum must be bracketed before a Golden Section minimization can be attempted, that is, we find two points a and c for which there exists some b such that $a < b < c$ and $f(b) < f(a), f(c)$. The bracketing algorithm accepts two valid x values, and then begins taking ever growing steps downhill until it successfully brackets the minimum, using a parabolic fit to target likely points for a minima, or failing that, to choose the size of the next step. The golden section search itself takes the three points returned by the bracketing algorithm and repeatedly finds new brackets for the minimum by bisecting the search region into a pair of golden sections. The algorithm terminates once it has narrowed the range to a set tolerance. These algorithms only find a local minimum, but as the functions in which we are interested are all concave and possess only a single minimum, this is not an issue.

[7]For this cross section, the maximum always occurs for minimum recoil, so while it is possible to determine numerically, it is not necessary. This algorithm is much more useful for NCE electron dark matter scattering or inelastic π^0 production, which both possess minima not located at the extreme of the kinematically allowed regime.

5.8.3 Integration Techniques

We will frequently need to perform numerical integrals for functions which are difficult or impossible to integrate analytically. For example, we do not possess an analytic expression for the the total NCE nucleon-dark matter cross section,

$$\sigma_{N\chi\to N\chi}(E_\chi) = \int dE_r \frac{d\sigma_{N\chi\to N\chi}}{dE_r}(E_\chi), \tag{5.21}$$

where E_r is the recoil energy of the nucleon and E_χ is the energy of the incident dark matter particle. We need to calculate the total cross section to calculate the probability of the dark matter interacting with the neutrino detector.

One-dimensional integrals in the code are handled using Sinh-Tanh Quadrature [188], also called double exponential integration. This integration scheme is particularly good for dealing with singularities at the edges of the integration regime, which were encountered when performing integrals to calculate $\mathrm{Br}(\pi^0 \to V_B^*\gamma \to \chi\bar{\chi}\gamma)$. The technique remaps an integral of some function $f(x)$ on $x \in [-1, 1]$ to an integral on $g \in (-\infty, \infty)$, where $g(x) = \tanh(\pi/2 \sinh(x))$, and then breaking it into an Euler-Maclaurin sum. This is quite effective, largely because this transformation tends to reshape the integrand into a bell curve. The change of variable goes as follows

$$F = \int_{-1}^{1} f(x)dx = \int_{-\infty}^{\infty} f(g(t))g'(t)dt \approx h \sum_{j=-N}^{N} w_j f(x_j), \tag{5.22}$$

where $x_j = g(hj)$ and

$$w_j = g'(hj) = \frac{\frac{h\pi}{2}\cosh(hj)}{\cosh^2\left(\frac{\pi}{2}\sinh(jh)\right)}. \tag{5.23}$$

In the simulation code itself, this is adapted somewhat to increase N and decrease h until a specified fractional accuracy goal is achieved. In the code we continue to iterate until $\left|\frac{F_{n+1}-F_n}{F_{n+1}}\right| \leq 10^{-3}$, where n and $n+1$ indicates two sequential estimates of the integral.

Two dimensional integrals are handled using Simpson Cubature (see [189]). The algorithm itself is a long series of sums and not terribly enlightening, and so it will not be reproduced here. This algorithm is currently only used to calculate the total production rate of V's in Proton Bremsstrahlung (see 4.2.3).

5.9 The Detector Class

The `detector` class exists to hold details about the detector's physical characteristics (the parameters discussed in 5.2.5), and to return the length of the intersection between a ray representing a particle's trajectory and the detector geometry, which we will call `Ldet`. We discuss the algorithms in detail for each case in the following sections.

5.9.1 Spherical Geometry

For this algorithm, we define $\mathbf{p}_\chi$ to be the dark matter three-momentum, R_{det} to be the radius of the fiducial volume[8] of the detector and

$$\mathbf{o} = \mathbf{r}_{\text{det}} - \mathbf{r}_\chi, \tag{5.24}$$

where $\mathbf{r}_{\text{det}}$ is a vector pointing from the origin to the center of the detector, and $\mathbf{r}_\chi$ is a vector from the origin to the creation point of the dark matter particle. If a position distribution is not supplied to modify the momentum distribution, then $\mathbf{r}_\chi = \mathbf{0}$. We also define a few scalar quantities

$$A = \mathbf{p}_\chi \cdot \mathbf{p}_\chi, \tag{5.25}$$

$$B = -2\mathbf{o} \cdot \mathbf{p}_\chi, \tag{5.26}$$

$$C = \mathbf{o} \cdot \mathbf{o} - R_{\text{det}}^2. \tag{5.27}$$

These scalars are the coefficients of the quadratic equation $Ax^2 + Bx + C = 0$ that we solve to determine the points of intersection between the dark matter trajectory and the spherical shell of the detector. These intersection points exist if the following conditions are satisfied:

$$B^2 - 4AC > 0, \tag{5.28}$$

$$A \neq 0 \tag{5.29}$$

We now define

$$L_\pm = \frac{-B \pm \sqrt{B^2 - 4AC}}{2A}, \tag{5.30}$$

[8]This defines the volume in which we accept signal events. Events originating too close to the outer shell of the detector are often difficult to resolve efficiently.

where $L_{-(+)}$ is the entrance (exit) point along the dark matter trajectory. These points are stored for later use in generating an event position inside the detector. One final ambiguity exists in that the particle's trajectory extends both forwards and backwards in time. If an intersecting particle's three-momentum were reversed, this algorithm would still find an intersection. We can check for this by verifying that $L_{\pm} \geq 0$. If either is less than zero, we set it to 0. The length of the intersection is calculated by

$$L_{\text{det}} = (L_+ - L_-)\sqrt{A}. \tag{5.31}$$

5.9.2 Cylindrical Geometry

The geometry of a cylindrical detector is more complicated to handle, but uses many of the tricks we employed in 5.9.1. When creating a cylindrical detector object, we store a new vector $\mathbf{l}$ which points from the center of the detector to the center of one of the circular faces,

$$l_x = \text{length}/2\cos(\textbf{det-phi})\sin(\textbf{det-theta}), \tag{5.32}$$

$$l_y = \text{length}/2\sin(\textbf{det-phi})\sin(\textbf{det-theta}), \tag{5.33}$$

$$l_z = \text{length}/2\cos(\textbf{det-theta}), \tag{5.34}$$

where we are using the variables defined in 5.2.5.

There are four possible intersection points for a line through a cylinder: one through each face and two possible crossings on the circular surface. We will check each in turn, and append each intersection found to a list of crossing points L. The algorithm terminates and returns a length of intersection as soon as two points of intersection are found.

We begin by checking for intersection with the faces of the cylinder. This amounts to calculating the intersection point with a plane parallel to the face, and then checking that it is within R_{det} of the center of the face. If $\mathbf{p}_\chi \cdot l = 0$, then the trajectory is parallel to the cylinder faces, and this step can be skipped. The points of intersection with planes parallel to the cylinder are given by

$$B_{\pm} = \frac{(\mathbf{o} + \mathbf{l}) \cdot \mathbf{l}}{\mathbf{p}_\chi \cdot \mathbf{l}}. \tag{5.35}$$

We next find the vector pointing from the center of each circular face to the point of

intersection on the plane

$$r_{\text{intersect},\pm} = B_{\pm}\mathbf{p}_{\chi} \mp \mathbf{l} - \mathbf{o}, \tag{5.36}$$

and check that $r^2_{\text{intersect},\pm} \leq R^2_{\text{det}}$. If so, then $B_{\pm}$ is added to the list of intersection points.

Calculating the points of intersection with the circular surface is very similar to the spherical case, in that we define three coefficients of a quadratic equation

$$X = -(\mathbf{p}_{\chi} \cdot \mathbf{l})^2 + \mathbf{p}^2_{\chi}\mathbf{l}^2, \tag{5.37}$$

$$Y = 2(\mathbf{p}_{\chi} \cdot \mathbf{l})(\mathbf{o} \cdot \mathbf{l}) - 2(\mathbf{o} \cdot \mathbf{p}_{\chi})\mathbf{l}^2, \tag{5.38}$$

$$Z = -(\mathbf{o} \cdot \mathbf{l})^2 - R^2_{\text{det}}\mathbf{l}^2 + \mathbf{o}^2\mathbf{l}^2, \tag{5.39}$$

and solving the quadratic equation $XC^2 + YC + Z = 0$ one finds $C_{\pm} = \frac{-Y \pm \sqrt{Y^2 - 4XZ}}{2X}$. If the argument of the square root is imaginary, no intersection occurs and we skip to the next step. To check that the intersection occurred in the region of the surface bounded by the two circular faces, we define

$$D_{\pm} = \frac{C_{\pm}\mathbf{p}_{\chi} \cdot \mathbf{l} - \mathbf{o} \cdot \mathbf{l}}{\mathbf{l}^2}. \tag{5.40}$$

If $|D_{\pm}| < 1$, then an intersection occurs, and the point $C_{\pm}$ is added to the list of intersection points.

The final step of this process is almost identical to that of the spherical case. Each member of L is set to 0 if negative and the entrance and exit points are defined as

$$L_{-} = \text{MIN}(L[0], L[1]), \tag{5.41}$$

$$L_{+} = \text{MAX}(L[0], L[1]). \tag{5.42}$$

Substituting $L_{\pm}$ into 5.31 returns the length of intersection.

5.9.3 Generating Interaction Positions

The distribution of positions of interaction events within the detector can also be useful information for experimentalists. As these dark matter events occur very rarely, the event rate is roughly equal at any given point along the trajectory, and an interaction point can be generated by selecting a random number $u \in [L_{-}, L_{+}]$. The

four-vector of the position and time of the interaction event can then be calculated using

$$t_{\text{int}} = \frac{u\|\mathbf{p}_\chi\|}{\|\mathbf{v}_\chi\|} + t_0, \tag{5.43}$$

$$\mathbf{r}_{\text{int}} = (t - t_0)\mathbf{v}_\chi + \mathbf{r}_\chi, \tag{5.44}$$

where t_0 is the creation time of the dark matter particle and $\mathbf{v}_\chi$ the velocity.

5.10 Summary

This chapter provided detailed instructions on the writing of parameter files which configure the operations of the BdNMC hidden sector dark matter simulation code for fixed target experiments, as well as a listing of all the essential and most useful customizable parameters. We gave a broad outline of the structure of the code, and discussed in more detail the most important aspects of the simulation, particularly how particle generation is handled from the production of secondary particles from a distribution, their decay path into dark matter, and the dark matter signal generation in an experimental detector. We also listed all of the algorithms used in integration, sampling distributions, minimization and calculating the intersection between particle trajectories and detector geometry.

Chapter 6

Sensitivity Limits

Name	Energy	POT	Mass	Distance	Angle
LSND	800 MeV	1.8×10^{23}	167 tonnes	35 m	31°
MiniBooNE	8 GeV	1.2×10^{21}	400 tonnes	545 m	on-axis
MiniBooNE-Beam Dump	8 GeV	2×10^{20}	400 tonnes	490 m	on-axis
ND280	30 GeV	5×10^{21}	6.1 tonnes	280 m	2.5°
Super-K	30 GeV	5×10^{21}	50 kilotonnes	295 km	2.5°
SHiP	400 GeV	2×10^{20}	2.5 tonnes	100 m	on-axis
COHERENT	1 GeV	10^{23}	1 tonne	20 m	90°
CENNS	8 GeV	10^{21}	1 tonne	20 m	90°

Table 6.1: A summary of relevant characteristics of the experiments considered. The listed masses are for the fiducial mass, when available. Note that several of these experiments are in the proposal or planning stages, and their design has not been finalized.

Fixed target neutrino experiments operate with the objective of studying neutrino properties: confirming the existence of neutrino oscillations, measuring numerical properties of the neutrino sector such as the mixing angles between different flavours, and precision measurements of their interactions with Standard Model baryons and leptons. These experiments generate neutrino beams by impacting a nuclear target, often composed of graphite or beryllium, with a high intensity beam of protons with energies ranging from below a GeV to a few hundred GeV. This creates enormous numbers of secondary mesons, whose decays result in the production of an equivalently large number of neutrinos.

Studying neutrino oscillations requires an accurate determination of the number of neutrinos of each flavour produced at the target through a combination of simu-

lation and theory, or by a measurement using a near detector. Often, this involves running smaller scale experiments with replica targets to calibrate the simulations. This target (near-detector) flux is then compared with the flux observed in the (far) detector, where an absence or excess of neutrinos of a particular flavour is indicative of neutrino oscillations. A good understanding of cosmic and beam related backgrounds is necessary, often requiring careful choice of detector position and design. Many experiments use magnetic focusing horns to focus the secondary mesons in the direction of the detector before they decay, creating a more tightly collimated beam of neutrinos. In addition, some experiments can use their magnetic focusing horns to select for a neutrino (or anti-neutrino) beam, defocussing the mesons that decay into anti-neutrinos (neutrinos).

In this chapter, we will show the predicted sensitivity to hidden sector dark matter for a series of fixed target neutrino and beam dump experiments, given the dark matter production and signal channels discussed in chapter 4. Some details of the setup for each experiment will be provided, as well as a brief discussion of how these sensitivities could be turned into exclusion limits. A summary of the main properties of each experiment required for the sensitivity calculations is provided in table 6. All of the sensitivity predictions were produced using the simulation software described in chapter 5, and the other constraints listed on plots for comparison are discussed in section 3.

6.1 LSND

Experimental Details

The Liquid Scintillator Neutrino Detector was a fixed target neutrino experiment at Los Alamos Neutron Science Center that ran from 1994 to 1995 with a water target, and then from 1996 to 1998 with a target of high-Z metal [190, 124]. Over the lifetime of the experiment, they delivered 1.8×10^{23} POT with a kinetic energy of 798 MeV, of which 9.23×10^{22} was impacted on the water target, and the remaining 8.22×10^{22} on the high-z metal. LSND made a non-zero measurement of excess anti-electron neutrino events, theoretically due to neutrino oscillations, and attempted to place a bound on one of the neutrino's masses [191]. The LSND experiment has the largest POT delivered over the course of its lifetime of any experiment which will be considered, and as such is capable of extraordinary sensitivity for values of m_V below

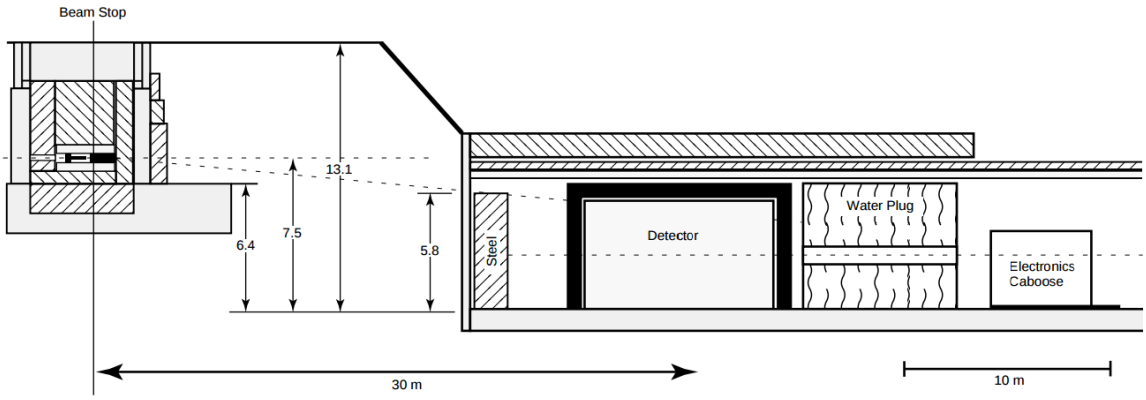

Figure 6.1: Schematic of the LSND experiment. Reprinted from Nucl. Instrum. Meth., Vol A388, Athanassopoulos, C. and others, The Liquid scintillator neutrino detector and LAMPF neutrino source, Pages 149-172, Copyright 1996, with permission from Elsevier.

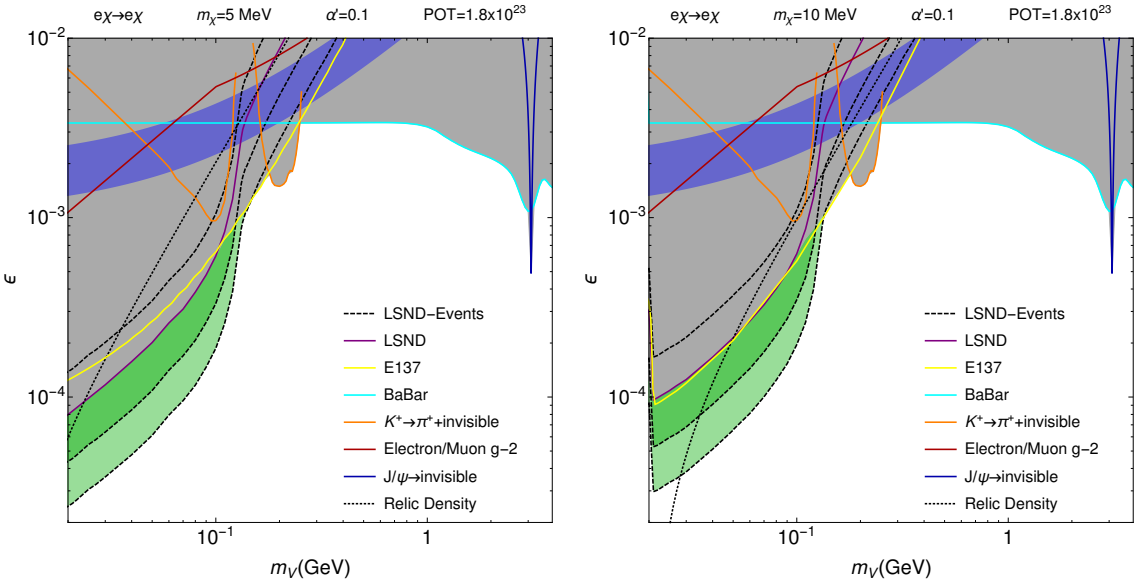

Figure 6.2: The number of NCE electron dark matter scattering events expected at LSND. We show three sensitivity contours, each representing a different range of events after cuts and efficiencies have been applied. The lightest green is the region where we expect 1-10 events, in the medium green 10-1000 events, and the darkest green (obscured on this plot) we expect more than 1000 events. Here we show the change in the LSND limits and sensitivity with a factor of 2 difference in the dark matter mass. The LSND limit corresponds to 110 expected events. The grey region is excluded by other experimental limits, and the blue region is favoured by muon g-2. More details on these limits can be found in Section 3.2.1. The sensitivity curves were generated with the code detailed in Chapter 5.

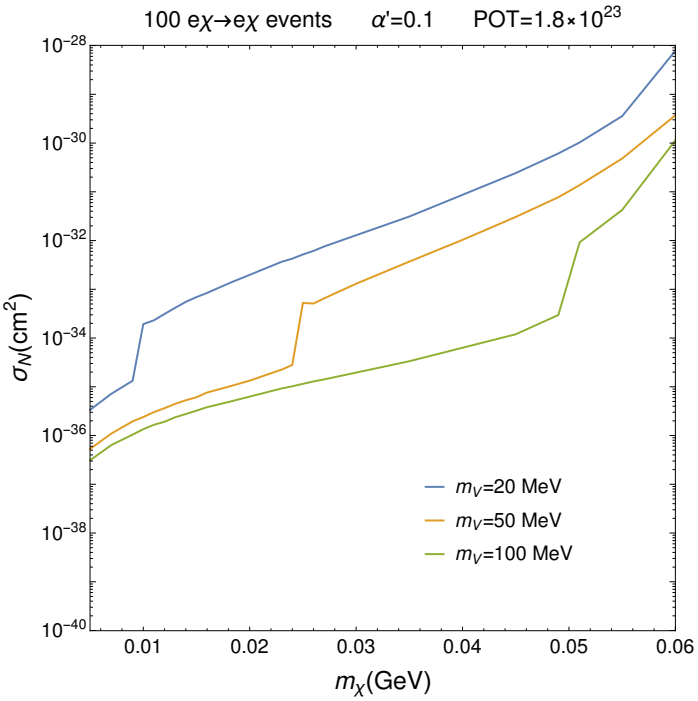

Figure 6.3: The number of NCE electron dark matter scattering events expected at LSND. This plot demonstrates how LSND's sensitivity changes with m_χ. The sudden drops are due to the V being forced off-shell.

the π^0 mass.

The detector itself is an 8.3 meter long cylinder with a diameter of 5.7 meters. The detector is filled with 167 tonnes of mineral oil, which we approximate as CH_2, with a small amount of added scintillator material. Event detection is performed through a combination of Cherenkov radiation and scintillation light. The center of the detector is located 30 meters downstream, and 4.6 meters below the target (see Fig. 6.1). Most of the neutrino production occurs via $\pi^+ \to \mu^+\nu_\mu$ and $\mu^+ \to e^+\nu_e\bar{\nu}_\mu$, where the decays largely occur at rest in the target. Most π^- are stopped and captured in the beam stop without decaying. The off-axis positioning of the detector allows the experiment to take advantage of the isotropic neutrino emission while avoiding much of the beam related background.

Production

For dark matter production at LSND, we are most interested in π^0 decays (see Section 4.2.1). As usual, N_{π^0} is expected to be within a factor of $\mathcal{O}(1)$ of N_{π^+}. This rate can be estimated by taking advantage of the isotropic neutrino signal expected, and then

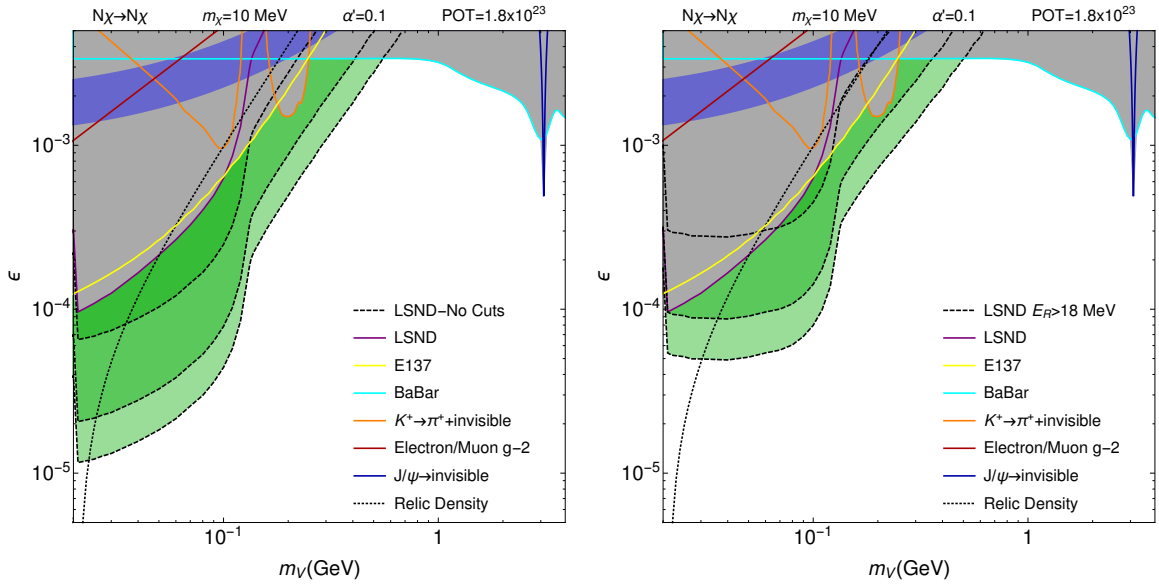

Figure 6.4: The number of NCE nucleon dark matter scattering events expected at LSND. See Fig. 6.2 for details of formatting. The optimistic expected event rates are in the left-hand plot are severely undermined by the lack of energy cuts. A more realistic estimate is made in the right-hand plot, where we implement a lower energy cut on the recoil energy of the outgoing nucleon of 18 MeV. As backgrounds are expected to be worse than in the NCE electron scattering case, a better lower energy cut would be required to improve on the limits achieved by the NCE electron scattering analysis.

LSND	
$e\chi \to e\chi$	
Efficiency	0.16
Electron Recoil Cut	[0.015,0.053] GeV
Event Limit	110

Table 6.2: Summary of cuts and efficiencies for the LSND signal

working backwards from the neutrino flux observed in the detector over the lifetime of the experiment

$$N_{\pi^+} \approx \frac{\Phi_\nu \times A_{\rm det}}{(d\Omega_{\rm lab}/4\pi)_\nu} \sim 10^{22}, \tag{6.1}$$

where $\Phi_\nu = 1.3 \times 10^{14}\ \nu\,{\rm cm}^{-2}$ is the neutrino flux over the lifetime of the experiment, $A_{\rm det} \simeq 2.5 \times 10^5$ cm^2 is the area of the detector facing the target, and $(d\Omega_{\rm lab}/4\pi)_\nu \simeq 3 \times 10^{-3}$ is the fraction of the solid angle subtended by the detector relative to the target. We will find later that this is not too far off the production rate expected for COHERENT, an experiment with similar beam energy. As the π^0's decay extremely

rapidly, and are not stopped or reabsorbed as with the charged pions, these decays are expected to occur in flight, and so we use Burman-Smith distribution to estimate the π^0 momentum distribution.

Signal

At LSND we will be particularly interested in NCE-like DM-electron scattering in the detector, as this can easily be compared to an existing experimental analysis of NCE neutrino electron scattering [124]. They accepted electron scattering events for which $E_e \in [18, 50]\,\text{MeV}$, where E_e is the electron recoil energy. Events that were less than 35 cm from the face of the detector, as well as those near the bottom (more than 120 cm below the center of the detector) were vetoed in order to reduce backgrounds. The experiment observed 55 non-standard scattering events after all cuts (and an efficiency factor of 0.19) were applied. A very conservative limit of 110 events was adopted to account for significant uncertainties in the pion production rate, and all parameter space that was shown to generate more than 110 dark matter electron scattering events is excluded. This limit was first demonstrated in [65] and expanded in [41].

Even without making any cuts on kinematics to differentiate DM from neutrino events, this number can be used in a counting experiment to exclude a large portion of the dark matter parameters space (see Fig. 6.2). There are large uncertainties which are difficult to quantify in the event rate estimate, largely linked to the π^0 production estimate. In order to address this, we will allow for the event rate to be off by as much as factor of 2 when calculating the exclusion limit.

It may be possible to dramatically improve this limit by analyzing nucleon scattering, as at low energies one would naively expect the NCE nucleon-χ scattering rate to scale as

$$\sigma_{N\chi\to N\chi} \sim \frac{m_N}{m_e}\sigma_{e\chi\to e\chi}.$$

The gain does not appear to be quite this strong in practice (see fig 6.4), though the gain in number of expected events when cuts on the recoil energy are not included is several hundred fold. This weakens dramatically if we include a cut on the kinetic energy similar to that placed on the electron, indicating that most of the expected scattering events possess extremely small momentum transfers (See Fig. 6.4). In order to make a significant gain in sensitivity over the electron limit at LSND, one would need to be able to detect very low energy recoils. The backgrounds are expected

to be at least an order of magnitude larger than in the electron case, which further diminishes the prospects for this approach.

6.2 MiniBooNE

Experimental Details

MiniBooNE - the Mini Booster Neutrino Experiment - is a fixed target experiment located at Fermilab that was run, in part, to check the results of LSND. The experiment generates a neutrino beam by impacting an 8.9 GeV proton beam provided by the Fermilab Booster onto a 70 cm long beryllium target. Following the target is a 50 m decay pipe leading to a large block of iron that serves as a beam stop. The target is surrounded by a set of magnetic focusing horns which focus the mesons, and subsequently the neutrino beam, towards the MiniBooNE detector, as well as allowing the experiment to choose between neutrino and anti-neutrino running modes. The detector itself is a 6.1 meter sphere filled with 650 tonnes of mineral oil, which, as with LSND, we represent by CH_2 (see Fig. 6.5). We exclude the outer 0.35 meters of the detector from the fiducial volume to match MiniBooNE fiducial volume cuts. The center of the detector is located 541 meters downstream of and 1.9 meters below the target.

MiniBooNE ran from 2002 to 2012 with several short breaks, and over the course of its experimental program received a total of 17.8×10^{20} POT, with 6.5×10^{20} POT in neutrino mode and 11.3×10^{20} POT in antineutrino mode [192]. As with LSND, they observed antineutrino excesses. In order to better understand the MiniBooNE oscillation signal, it became desirable to conduct additional running in a beam dump configuration. It soon became apparent that MiniBooNE, by running in a beam dump configuration, would become highly sensitive to light kinetically-mixed hidden sector dark matter.

The primary background in a dark matter search at a fixed target neutrino experiment is the neutrino signal itself, as their neutral-current elastic interactions are quite similar to each other. In a beam dump run, the proton beam is directed around the target and directly into the beam stop at the end of the decay pipe. Most produced charged mesons are stopped, if positively charged, or absorbed, if negatively charged, rather than decaying in flight, dramatically reducing the neutrino flux on the detector. In the case of MiniBooNE, directing the proton beam into the beam

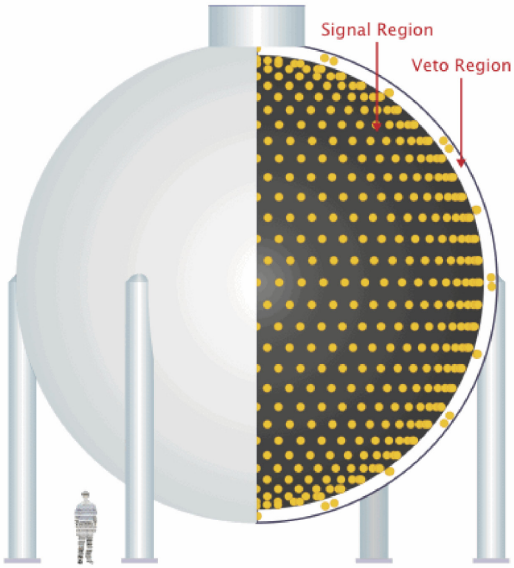

Figure 6.5: Schematic of the MiniBooNE Detector. Reprinted figure with permission from Cheng, G. and others, Physical Review, Vol. D86, pg. 052009, 2012. Copyright (2012) by the American Physical Society.

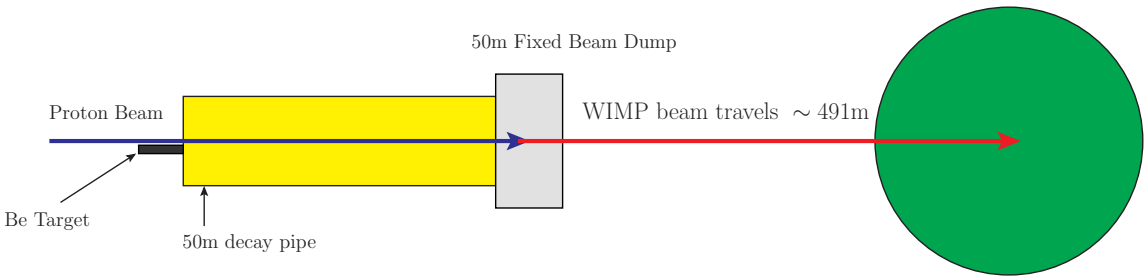

Figure 6.6: Schematic of the MiniBooNE experiment running in beam dump mode. Another possible configuration included the deployment of an additional beam stop at 25 meters down the decay pipe to further decrease neutrino background, though this ultimately was not adopted.

stop was expected to reduce the neutrino flux by a factor of approximately 40. A proposal for beam dump running was written in 2012 with the dark matter search serving as the primary motivation. After a short engineering run which served to test the concept, approximately 2×10^{20} POT were collected from December of 2013 to November of 2014 [14].

Production

The larger energy of the MiniBooNE proton beam opens up the full range of production channels discussed in Chapter 4. We use the mean of MiniBooNE's Sanford-Wang fits for π^+ and π^- to estimate π^0 production, and their K^0 distribution for the η [185]. It should be noted that this distribution was fitted for a thin beryllium target, and not a block of steel many nuclear interaction lengths thick[1] Additionally, simulated production occurs at the beam dump, or 491 meters from the detector.

We estimated the total number of π^0's produced per POT to be $\approx$0.9 by comparing with simulated multiplicities from MiniBooNE's neutrino flux analysis [185]. We conservatively set $N_\eta = N_{\pi^0}/30$ based on a comparison of their production cross sections in pp collisions[160]. For $m_V > m_\pi^0$, it is also important to consider proton bremsstrahlung. Satisfying the kinematic assumptions are a little tricky, as the beam energy is not orders of magnitude larger than the proton mass. In order to satisfy these constraints, we force $z \in [0.3, 0.7]$ and $p_\perp < 0.1$ GeV. We also consider parton level production for $m_V > 1$ GeV, though its contribution to MiniBooNE sensitivity is minimal.

Signal

Unlike LSND, MiniBooNE is sensitive to NCE electron and nucleon scattering, as well as pion inelastic scattering. We will consider all three interaction channels, and attempt to compare them to existing analyses in order to estimate kinematic cuts and expected neutrino backgrounds. The shown results will be targeted at the beam dump setup and number of POT, as the dramatic decline in neutrino background more than compensates for the drop in total dark matter production.

For NCE nucleon dark matter scattering, we take our energy cuts on the nucleon recoil E_R from discussions with members of the MiniBooNE collaboration and their

[1]Simulated π^0 production data generated using MiniBooNE's GEANT-4 target simulation was supplied by Tyler Thornton and compared with π^0's generated from the Sanford-Wang distribution, and significant differences in the distributions were observed. Qualitatively, the simulated steel distribution was much broader, with a significant number of nearly isotropic low energy π^0's. While the π^0's with significant forward momenta made up a much smaller fraction of the total π^0 sample, there were more than three times as many π^0's produced in total. This significantly larger production rate compensated for the more diffuse and lower energy emission distribution, and the final predicted dark matter event rates agreed to within $\mathcal{O}(20\%)$. Confirming some of our assumptions, the π^0 and the charged pion production rates were very similar, and their distributions did not differ to a great extent. In addition, some production still occurs in the target and decay pipe. For a true experimental analysis of the scenario to be performed, the simulated data would have to be used rather than the Sanford-Wang distribution.

MiniBooNE	
$e\chi \to e\chi$	
Efficiency	0.35
Electron Angle Cut	$\cos(\theta_{\text{beam}}) > 0.99$
Event Limit	≈ 3
$N\chi \to N\chi$	
Efficiency	0.35
Nucleon recoil cut	$KE_R \in [0.35, 1]\,\text{GeV}$
$N\chi \to N\chi\pi^0$	
Efficiency	0.35
Event Limit	$\mathcal{O}(10)$

Table 6.3: Summary of cuts and efficiencies for possible MiniBooNE signals

neutral current elastic scattering analysis paper[193]. We select cuts on the recoil nucleon's kinetic energy of $KE_R \in [0.035, 1]$ GeV, and assign an overall efficiency to the signal rate of $\epsilon_{\text{eff}} = 0.35$. It is also possible to implement a timing cut for scenarios with $m_\chi > 100\,\text{MeV}$, as MiniBooNE possesses sufficient timing resolution to differentiate the time delay[2] between the arrival of the neutrino bunch and the dark matter, though this analysis requires some significant additional work on the experimental side. We plot the results in Fig. 6.7. The same cuts are employed for the leptophobic scenario, and the results are shown in Fig. 6.11.

For inelastic π^0 production, no cuts are imposed as it appears that π^0's of all momenta can be detected by the MiniBooNE collaboration, and again assign an overall detection efficiency of $\epsilon_{\text{eff}} = 0.35$ [18]. The total number of events observed was 24164 over the course of the MiniBooNE beam on target run. As a rough estimate, we would expect the neutrino flux, and therefore the total number of π^0 production events, to decline by a factor of ≈ 213 for the beam dump run as compared to on-target operating mode. This is a product of the decline in POT by a factor of 5.1, and the 42 fold reduction in neutrino flux per POT due to the beam dump configuration. Therefore, during the beam dump run a total of ≈ 113 events would be expected, and any significant deviation from this number (which could be defined as $\mathcal{O}(\sqrt{113} \sim 10)$ events) could be attributed to the new, hidden sector dark matter (see Fig. 6.10). It is encouraging that it is possible to impose a limit through a counting experiment alone, as it appears difficult to differentiate dark matter and neutrino induced π^0's, as their momentum distributions are quite similar (see figs. 6.8 and

[2]For $m_\chi = 0.1\,\text{GeV}$ and $E_\chi = 1\,\text{GeV}$, the time delay would be $\mathcal{O}(10\text{ ns})$.

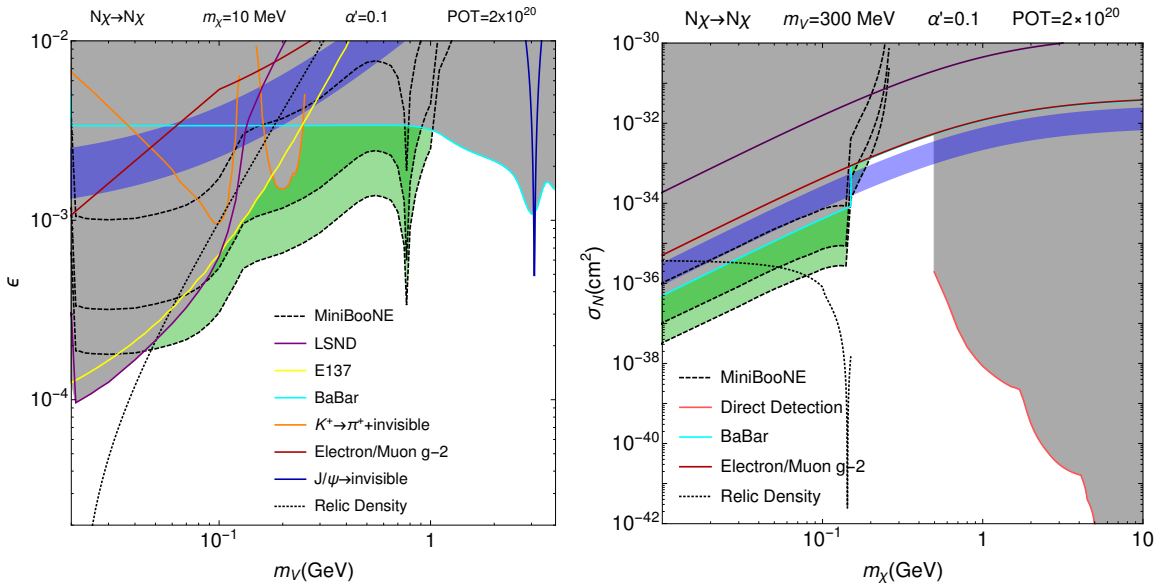

Figure 6.7: The number of NCE nucleon scattering events expected at MiniBooNE. See figure 6.2 for more details on formatting of the plots. MiniBooNE may be capable of placing new limits on the parameter space for V masses of a few hundred MeV. Note that the sharp peak where m_V approaches the ρ and ω masses arises from a peak in the form factor used for bremsstrahlung production (see Fig. 4.7).

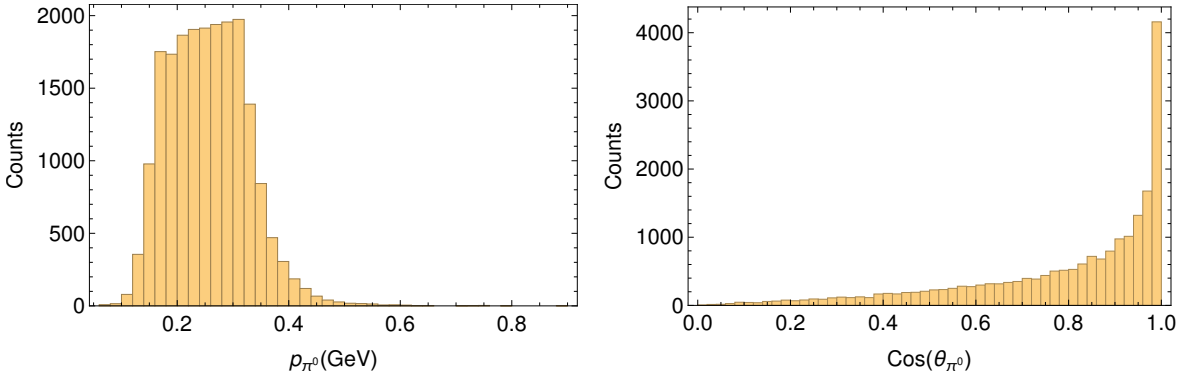

Figure 6.8: The momentum and angular distribution of recoil π^0's produced in $\chi N \to \chi N \pi^0$ inelastic scattering interactions for 2×10^4 sample events generated with $m_V = 0.2\,\text{GeV}$ and $m_\chi = 0.01\,\text{GeV}$. The momentum distribution is quite similar to that found by the MiniBooNE experiment, and would be fairly difficult to differentiate [18]. The angular distributions are quite different, with the dark matter induced π^0 production far more focused in the forward direction. The MiniBooNE distribution includes more advanced nuclear modeling with final state effects that may serve to broaden the π^0 distribution, so this difference may be decreased under a more complete analysis.

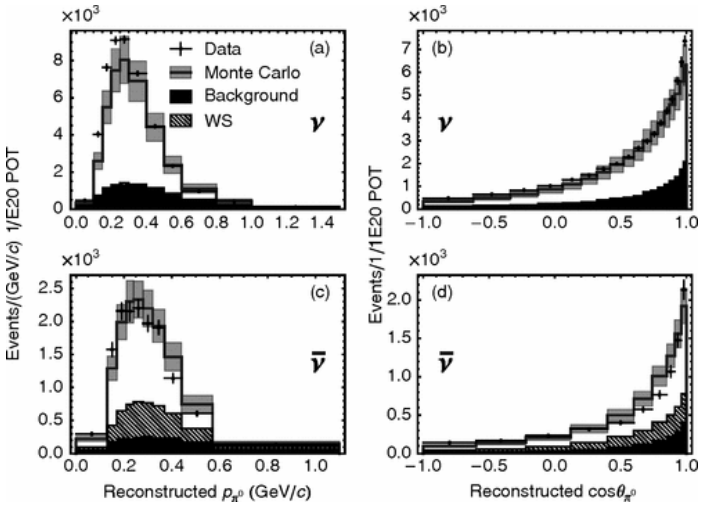

Figure 6.9: The momentum and angle distributions of π^0's produced via neutral-current interactions in the MiniBooNE detector. Reprinted figure with permission from Aguilar-Arevalo, Alexis A. and others, Physical Review, Vol. D81, 013005, 2010. Copyright 2010 by the American Physical Society. [18]

6.9). Should further analysis find some good means of differentiating the angular and momentum distributions (it is possible that the inelastic pion distribution could change dramatically for some mass parameters) or by imposing good timing cuts, then these limits could be further improved.

The NCE electron dark matter scattering analysis is still in the early stages, but preliminary estimates of backgrounds and sensitivity were made in the beam dump proposal[14]. Much of the NCE electron scattering background can be removed by placing a cut on the recoil electron scattering angle of $\cos(\theta_e) > 0.99$. With this cut in place, the dark matter signal could have a significant and noticeable effect with as few as three events. We plot the sensitivity curves in Fig. 6.12. The MiniBooNE sensitivity is just barely better than currently available limits for $m_V < 400\,\text{MeV}$. The constant $m_V = 300\,\text{MeV}$ slice also demonstrates a small improvement on current limits for all values of $m_\chi < m_V/2$.

6.3 T2K - ND280 and Super-K

Experimental Details

T2K - Tokai to Kamioka - is a fixed target off-axis neutrino experiment that began operation in 2010, whose primary goal was the measurement of the neutrino mix-

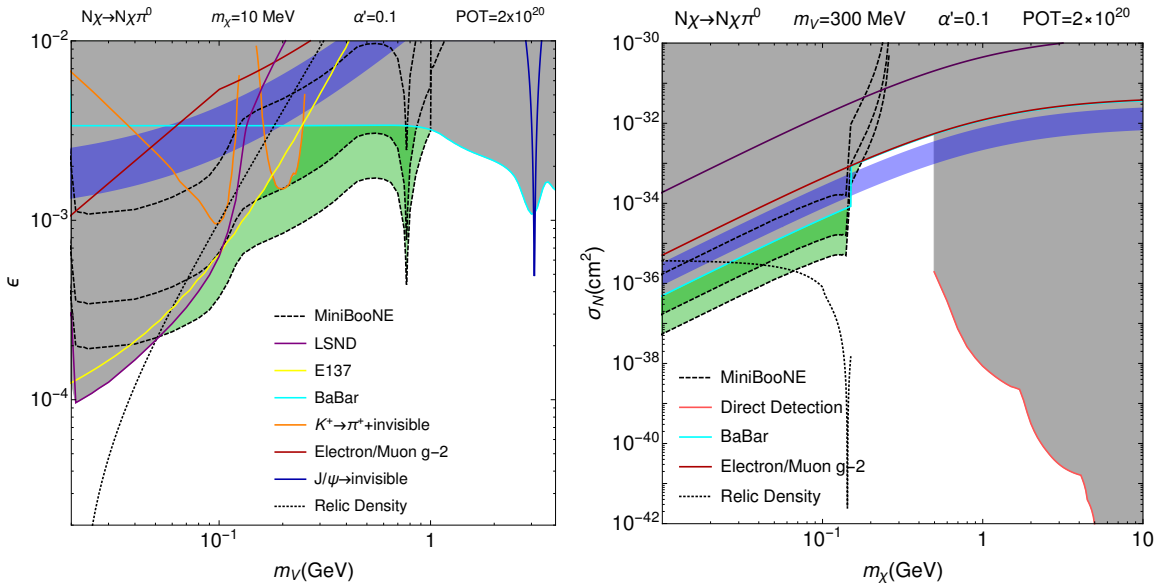

Figure 6.10: The number of inelastic pion events expected at MiniBooNE. See the caption of figure 6.2 for more details on formatting of the plots. While the number of events is lower than in the nucleon scattering case, the backgrounds sufficiently low that a limit could be placed on the parameters space predicting as few as $\mathcal{O}(10)$ dark matter scattering events.

ing angle θ_{13}. It generates a muon neutrino beam at J-PARC[3], located on the east coast of Japan, by impacting a 30 GeV proton beam on a 91.4 cm graphite target [19]. T2K actually possesses two detectors of interest to this analysis, a near detector located 280 meters from the target named ND280, and a far detector called Super Kamiokande[194] located 295 kilometers to the west in Kamioka. ND280 is a multicomponent near detector that studies the properties of the neutrino beam before significant oscillations have occurred, which can then be compared with the signal at Super-K, a 50 tonne cylindrical water Cerenkov detector. T2K's detectors are actually located at 2.5° relative to the beam axis, in order to select for a neutrino distribution with its peak energy at 0.6 GeV, which in turn maximizes the oscillation signal at Super-K. Over the course of its planned operations the T2K experiment is expected to receive approximately 5×10^{21} POT[195].

We are most interested in a single component of ND280, the Pi-zero Detector or PØD[196]. The PØD measures the rate of neutral current π^0 production, $\nu_\mu N \to \nu_\mu N \pi^0$, on water in order to constrain this rate in the Super-K detector, where it represents a significant background to ν_e appearance measurements. We represent the

[3]Japan Proton Accelerator Research Complex

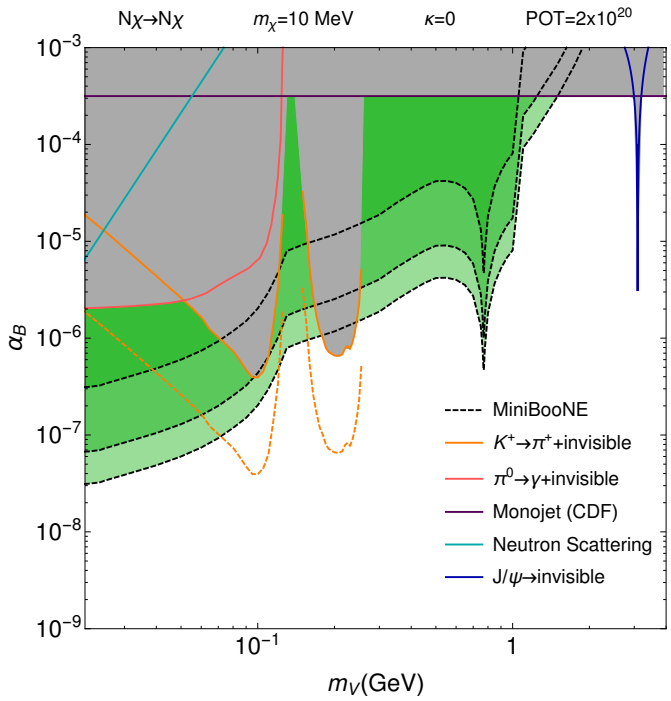

Figure 6.11: The number of NCE nucleon-dark matter scattering events expected at MiniBooNE in the leptophobic scenario. See the caption of figure 6.2 for more details on formatting of the plots. MiniBooNE is well positioned to greatly improve the limits on the leptophobic parameter space, even should the backgrounds amount to thousands of events. The sharp drop in the signal at $m_V = 1\,\text{GeV}$ is non-physical, as we turn off the proton bremsstrahlung channel at this point in order to continue to satisfy the assumptions made in 4.17. This condition can be relaxed at higher energy experiments. We do not generate events for $m_V < 2m_\chi$.

PØD by a fiducial mass of 6.1 tonnes of mixed brass, water and plastics approximately 280 meters from the target. Note that this is a bit optimistic, as the water is sometimes removed from the PØD in order to more precisely measure the π^0 production rate on water[4]. Super-K is represented by a 41 m tall cylinder with a 39 m diameter (see Fig. 6.13) filled with water.

Production

Production at T2K is very similar to that at MiniBooNE, utilizing all of the same channels. We adopt the BMPT distribution[165], a more general pion momentum

[4]By removing the water, they can compare the π^0 production rate with and without its presence in the detector. The difference between the two rates provides a precise measurement of the cross-section on water while eliminating production from other detector materials.

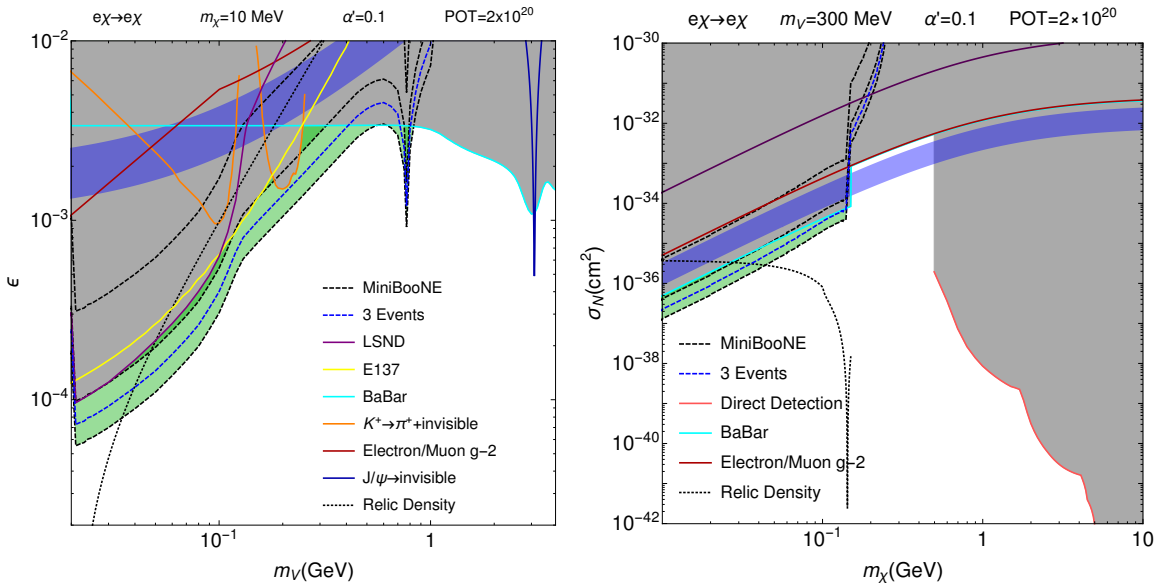

Figure 6.12: The number of NCE electron-dark matter scattering events expected at MiniBooNE. We plot a 3 event line, where preliminary estimates of backgrounds indicate limits could be placed. Were an analysis performed, it appears that MiniBooNE is well placed to beat all current limits on the hidden sector scenario for low masses of V. See the caption of figure 6.2 for more details on formatting of the plots.

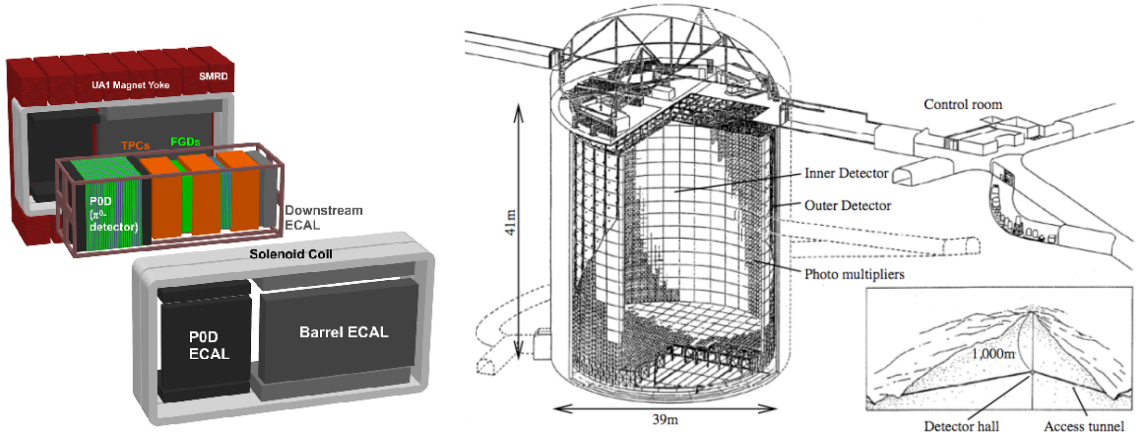

Figure 6.13: Art of ND280 (left) and Super-K (right). Reprinted from [19] with permission from Elsevier.

distribution suitable for a variety of materials and beam energies that was discussed previously in section 4.2.1, for both π^0 and η production. For proton bremsstrahlung, the much higher energies of the T2K beam allows us to relax the limits on z to $z \in [0.2, 0.8]$, and allow $p_\perp < 1\,\text{GeV}$. Finally, parton-level production becomes far more important, and the region of at least marginal sensitivity is pushed beyond

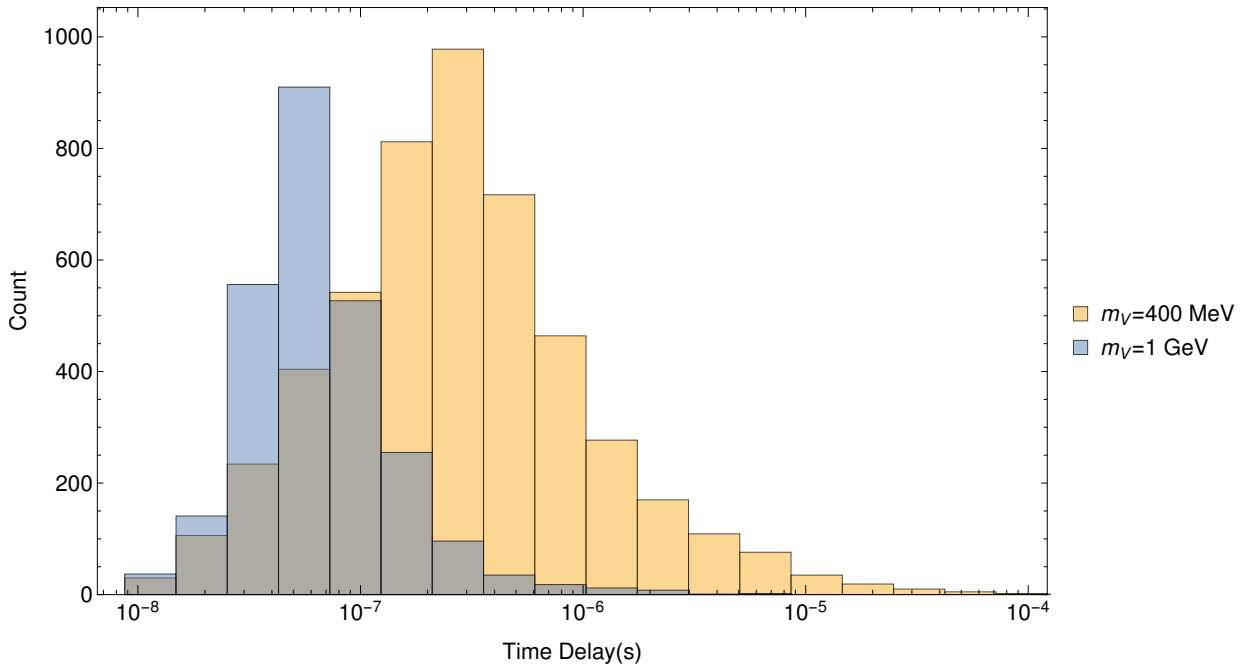

Figure 6.14: A histogram of time delays for 5000 Super-K events generated with $m_\chi = 0.1\,\text{GeV}$ and $m_V = 0.4, 1\,\text{GeV}$. The distribution peaks at 250 ns for $m_V = 0.4\,\text{GeV}$, well above the timing cut, and the timing cut efficiency of greater than 95% reflects this. For the heavier $m_V = 1\,\text{GeV}$, the median is 58 ns and the efficiency falls to 88%. A large part in the difference between the two cases is due to the change in the behavior and relative importance of the production channels. At low masses, η production is still a significant contributor, while at larger masses the higher energy partonic and bremsstrahlung channels strongly dominate.

$m_V \approx 1$ GeV.

Signal

We will make projections for inelastic π^0 production in both Super-K the PØD, and will also consider NCE nucleon-dark matter scattering in Super-K.

The number of dark matter scattering events at Super-K will necessarily be very small due to the enormous geometrical suppression the long beamline provides. However, by careful cuts on energy and timing, the majority of beam related backgrounds can be removed. Specifically, we are only interested in out-of-time scattering events, those which occur outside of the regular neutrino bunches. Neutrinos take approximately 984 μs to reach the Super-K detector, with a spill length of about 5 μs, while the dark matter experiences a time delay on the order of 100 ns to 1 μs (see Fig. 6.14).

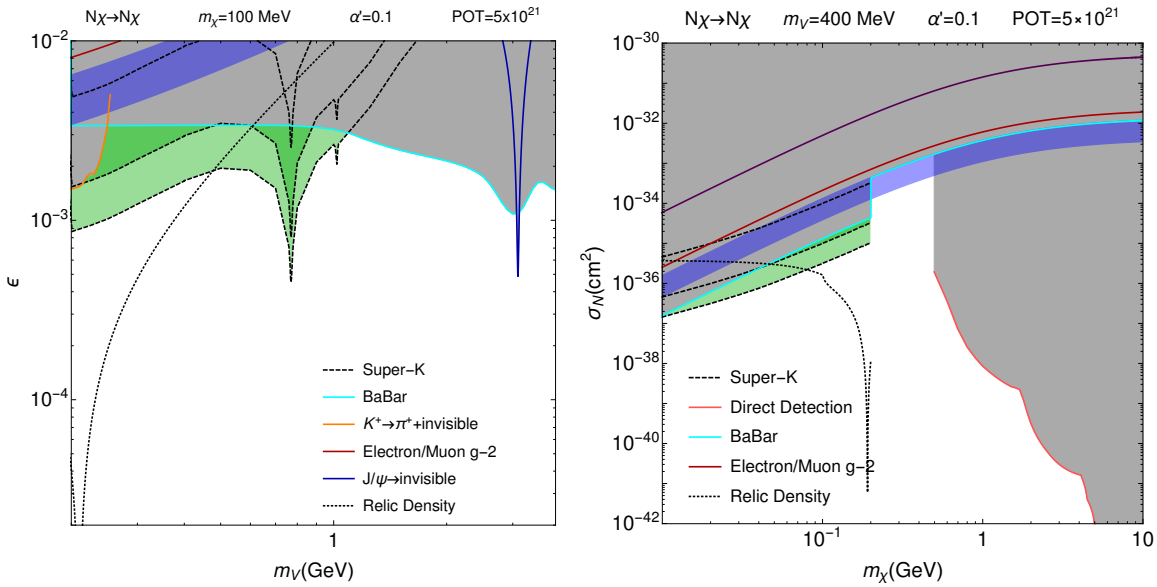

Figure 6.15: The number of NCE nucleon scattering events expected at Super-K. See figure 6.2 for more details on formatting of the plots. Super-K is capable of some sensitivity up to $m_V \approx 1\,\text{GeV}$, but it is very difficult to beat the limits imposed by BaBar. The signal rate gradually increases with increasing dark matter mass relative to the other constraints in the right-hand plot.

Super-K	
$N\chi \to N\chi$	
Efficiency	0.66
Momentum Transfer	$Q^2 > (0.05)\,\text{GeV}^2$
Timing	$t_{\text{delay}} > 50\,\text{ns}$
Event Limit	$\mathcal{O}(10)$
$N\chi \to N\chi\pi^0$	
Efficiency	0.66
Timing	$t_{\text{delay}} > 50\,\text{ns}$
ND280	
$N\chi \to N\chi$	
Efficiency	0.5

Table 6.4: Summary of cuts and efficiencies for the Super-K and ND280 PØD signals. It is difficult to make cuts or estimate backgrounds on the latter without access to an analysis.

These spills contain 8 50 ns long neutrino bunches, and any dark matter events occurring outside of these bunches would be nearly free of neutrino background[5]. For the

[5]These details of the T2K beam structure were provided by Akira Konaka

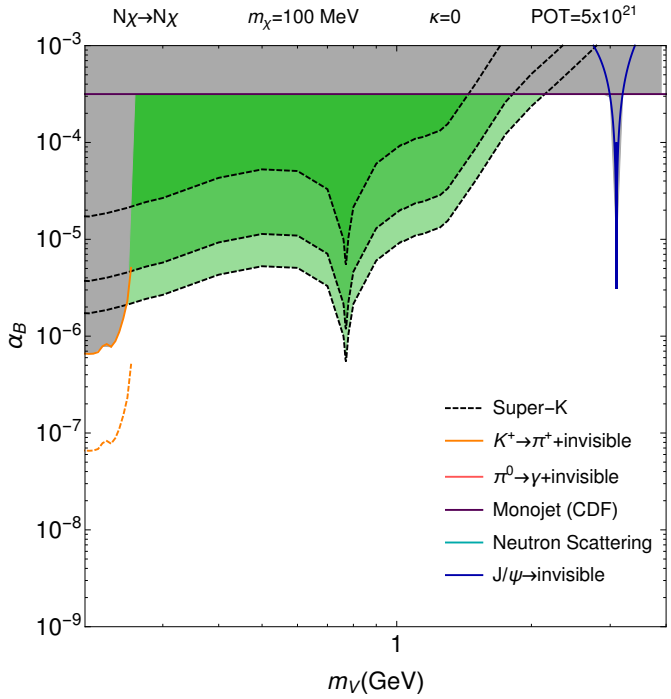

Figure 6.16: The number of NCE nucleon scattering events expected at Super-K in the leptophobic scenario. See figure 6.2 for more details on formatting of the plots. Super-K has far greater mass reach in the leptophobic scenario due to the weakness of existing constraints.

purposes of the simulation, we assume that any dark matter event occurring outside of its bunch will be recorded as an out-of-time event. We also impose a minimum energy transfer of $Q^2 > (0.05\,\mathrm{GeV})^2$. We show results for nucleon scattering for the kinetic mixing case in Fig. 6.15 and for the baryonic case in Fig. 6.16. Both cases exhibit good potential for sensitivity, should the backgrounds be as low as expected. As in the MiniBooNE case, the signal expected from inelastic π^0 is down by about an order of magnitude (see Fig. 6.17), but as it lacks an equivalent decline in backgrounds, is unlikely to be useful in constraining the dark matter scenario.

At this point, we have come to the end of our study of existing experiments. We have neglected some fixed target neutrino experiments such as MINOS and NOvA, but this is due to a combination their relatively low fiducial masses, POT and small angular acceptances. These factors combine to render their sensitivity to hidden

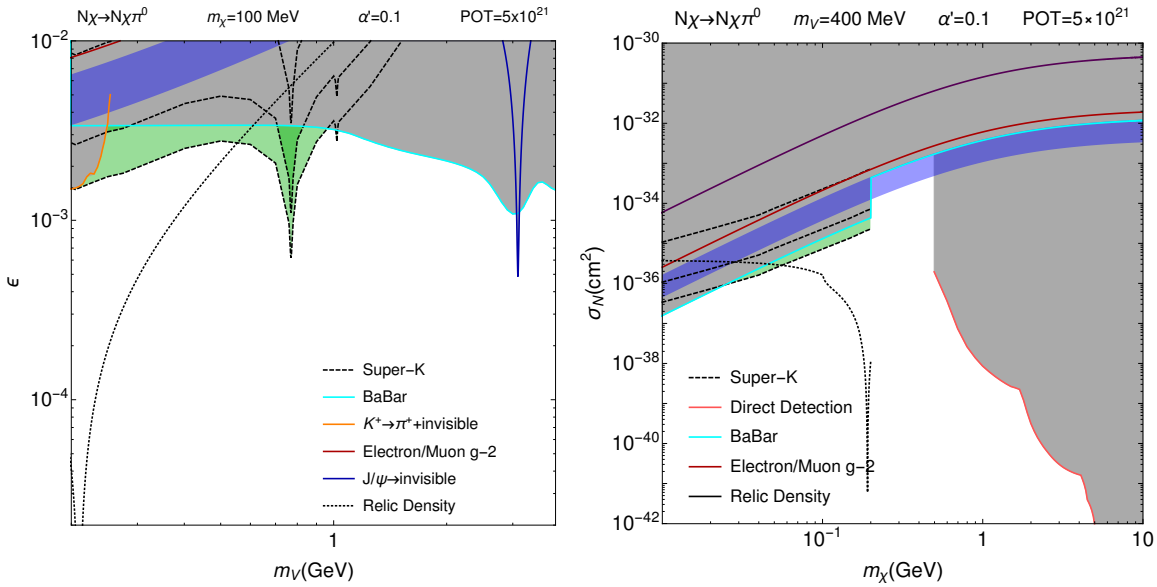

Figure 6.17: The number of neutral current inelastic π^0 events expected at Super-K. See figure 6.2 for more details on formatting of the plots. Pion-Inelastic scattering does not appear to be a viable probe of the dark matter parameter space at SuperK, as we expect that nucleon scattering backgrounds will not be much higher, and possess much stronger sensitivity.

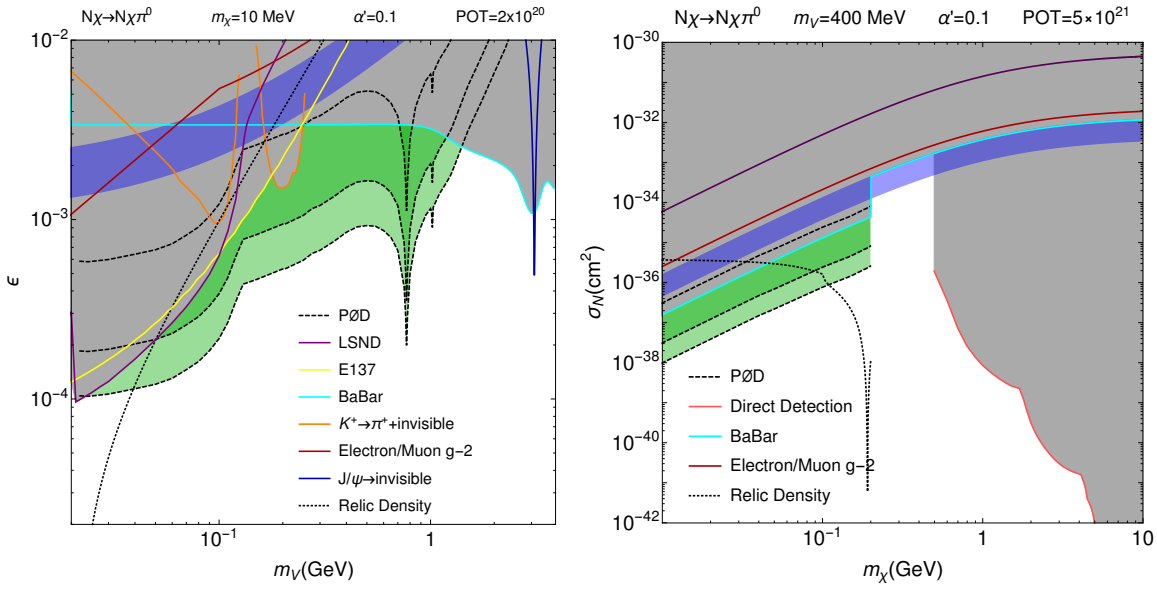

Figure 6.18: The number of inelastic pion events expected at ND280. See figure 6.2 for more details on formatting of the plots.

sector dark matter scenarios too low to beat existing constraints.

We will now provide some sensitivity estimates for hypothetical experiments that

are currently somewhere in the planning process. We hope that by making a case for their symbiotic sensitivity to hidden sector dark matter scenarios during normal running, we can improve their physics case and help them to move forward, as well as providing guidance on how these experiments can improve their sensitivity to hidden sector states.

6.4 COHERENT and CENNS

Experimental Details

Recent developments in detector technology have resulted in two similar proposals, COHERENT[197, 20] and CENNS[21], for fixed target neutrino experiments that could study coherent neutral-current neutrino-nucleus scattering (CEνNS). This would provide an interesting test of Standard Model physics, as well as being important both for detecting supernovae signals and understanding the role of neutrinos in the evolution of core collapse supernovas. Both of these experiments are in the planning stages and have not finalized their designs, so we will adopt the most advantageous setup for dark matter detection for use in our projections.

The CENNS proposal is for an off-axis experiment using the MiniBooNE target and the 8.9 GeV proton beam from the BNB. The reuse of the target simplifies our analysis considerably, as we have already established a dark matter production model. We will take this detector to be one tonne of liquid argon located 20 meters from the target, at an angle of 90° relative to the beam axis, which should dramatically reduced any decay in flight neutrino signal. In addition, we will consider a perhaps optimistic POT of 5×10^{21}, equivalent to about five years running time.

COHERENT plans to use the 1 GeV Spalation Neutron Source (SNS) at Oakridge National Laboratory. The majority of neutrinos from SNS come from stopped pion decays, which leads to a well studied neutrino distributions with a maximum energy of 52.6 MeV. As with CENNS, we will consider a one tonne target located 20 meters away and 90° relative to the beam axis, though this target would be composed of Cesium Iodide or Xenon. Note that COHERENT has a multi-phase experimental plan, beginning with smaller targets and building up to a tonne scale experiment in phase-3. We will consider 10^{23} POT, which corresponds to a year's running time at SNS.

Production

We will consider both π^0 decay in flight and π^- capture for COHERENT and CENNS. At COHERENT, the π^0 momentum distribution will be modeled by the Burman-Smith distribution used previously for LSND, as it should be appropriate for the 1 GeV beam. The number of charged pions produced at the SNS is $N_{\pi^-} = 0.05 \times \text{POT}$ and $N_{\pi^+} = 0.17 \times \text{POT}$[20]. At CENNS, we will use MiniBooNE's Sanford-Wang distribution and target multiplicities $N_{\pi^+} = N_{\pi^-} \approx 0.9 \times \text{POT}$. π^- capture results in an isotropic decay distribution, so no extra modeling should be required apart from choosing an emission energy (129 MeV) for the photon emitted during de-excitation. Finally, we will also consider η decay in flight at COHERENT, which extends the mass range to greater values of m_V.

Signal

We primarily consider coherent scattering off of Argon atoms at CENNS, and off of a mixture Cesium and Iodine atoms at COHERENT. Though we also accept NCE nucleon scattering for $Q^2 > 50\,\text{MeV}^2$, these events only make a significant contribution to the larger V masses and energies possible with the CENNS signal. Once again, neutrino scattering provides the primary background to our dark matter search, but use of timing and energy cuts can do much to differentiate the signals. The dark matter is expected to be produced promptly, due to the rapid decay of the π^0, η and absorption of π^-'s, and only the prompt neutrino signal will act as background. At COHERENT, this means only accepting events for which $E_{\text{recoil}} > 16\,\text{keV}$, and at CENNS, $E_{\text{recoil}} > 50\,\text{keV}$. Note that these results are generated with a detection efficiency of 0.5, which is only a rough estimate based upon preliminary estimates and is comparable to that seen at other neutrino experiments.

$A\chi \to A\chi$		
	COHERENT	CENNS
Atomic Nuclei A	Cs/I	Ar
Efficiency	0.5	0.5
Nuclear Recoil	$E_{\text{recoil}} \geq 15\,\text{keV}$	$E_{\text{recoil}} \geq 50\,\text{keV}$

Table 6.5: Summary of cuts and efficiencies for the COHERENT and CENNS signals.

Results are shown in figures 6.21 and 6.22. Firm backgrounds are not known at this point, but with the selected energy cuts they could be as low as $\mathcal{O}(10)$ events.

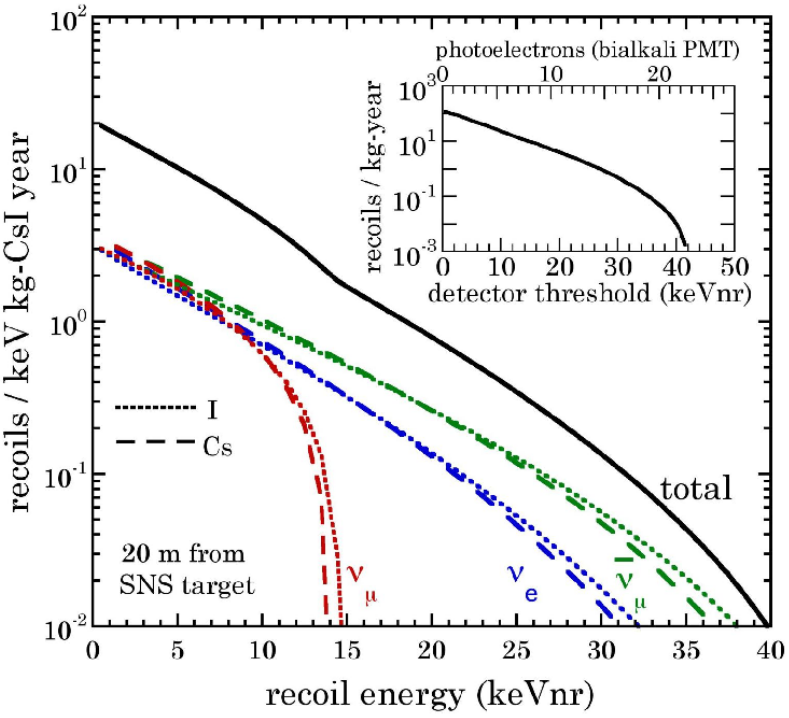

Figure 6.19: The expected neutrino-nucleus recoil spectrum expected for the COHERENT detector 20 meters from the target. Note that the ν_μ's are emitted promptly with an energy of about 30 MeV, while the production of other neutrino species is delayed. The prompt neutrino background disappears almost entirely for nuclear recoil energies greater than 15 keV. Reprinted from [20] with permission from Elsevier.

These experiments possess enormous potential sensitivity in the leptophobic scenario, and are capable of probing large regions of the parameter space for which $m_V < m_{\pi^0,\eta}$. In the kinetic mixing scenario, the sensitivity is competitive with LSND, but unlikely to improve on the limits already set by a significant margin.

6.5 SHiP

Experimental Details

SHiP - the Search for Hidden Particles - is the only dedicated beam dump experiment we will consider [67, 198]. It is still in the early planning stages and may not receive the funding needed to move forward, but it has the potential to provide one of the most interesting and high energy probes of hidden sector dark matter. SHiP would make use of a beam of 400 GeV protons from SPS, the Super Proton Synchrotron,

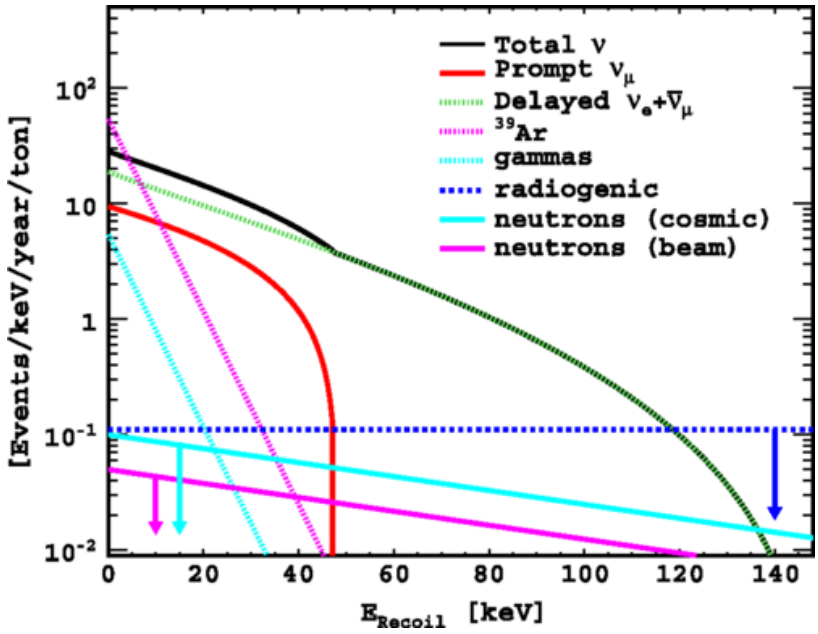

Figure 6.20: The expected neutrino-nucleus recoil spectrum expected for a far off-axis CENNS detector 20 meters from the target. The prompt signal disappears almost entirely for recoils above 50 keV. Reprinted figure with permission from Brice, S. J. and others, Phys Rev, D89, 072004, 2014. Copyright (2014) by the American Physical Society [21].

on some high-Z metal beam stop, which we will take to be Tungsten. A number of possible detector designs have been suggested, but we will consider 2.5 tonnes of liquid argon situated about 100 meters down the beamline from the target. The exact material and shape are not important at this stage, as we are mostly interested in the existence of some fiducial mass with which dark matter can interact. We perform our sensitivity estimates for a run of 2×10^{20} POT.

Production

SHiP's high energies make it particularly sensitive to higher mass χ and V particles, in the range of hundreds of MeV for the χ and several GeV for the V. We still include production from pseudoscalar mesons, and take the expected number of π^0's to be 1.8 per POT. This is a very rough estimate of multiplicity from the scaling of π^0 production with energy. Also included are bremsstrahlung, where we loosen the limits on the kinematics to $z \in [0.1, 0.9]$ and $p_\perp < 1$ GeV, and direct parton level production. In addition to these production channels, we also consider resonant V production from mixing with the $\phi(1020)$.

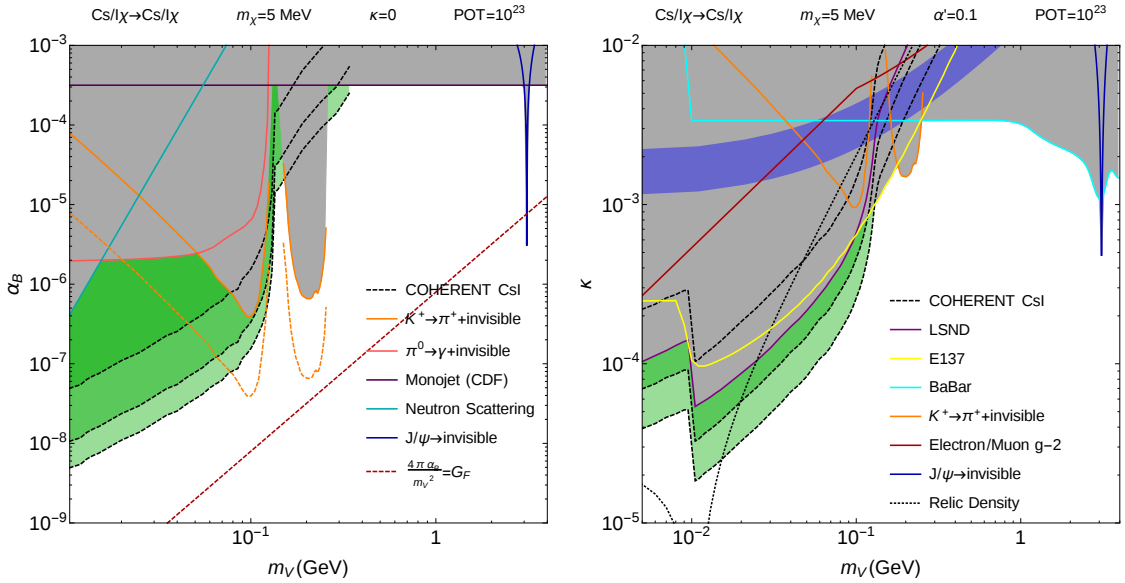

Figure 6.21: Sensitivity contours for COHERENT. The left panel shows sensitivity to the leptophobic scenario, while the right is for kinetic mixing. Also plotted is the line $4\pi\alpha_B/m_V^2 = G_F^2$, where the baryonic interaction is of comparable coupling strength to the weak exchanges. These plots originally appeared in [22]. Note that for these plots we use κ instead of ϵ, but they are equivalent.

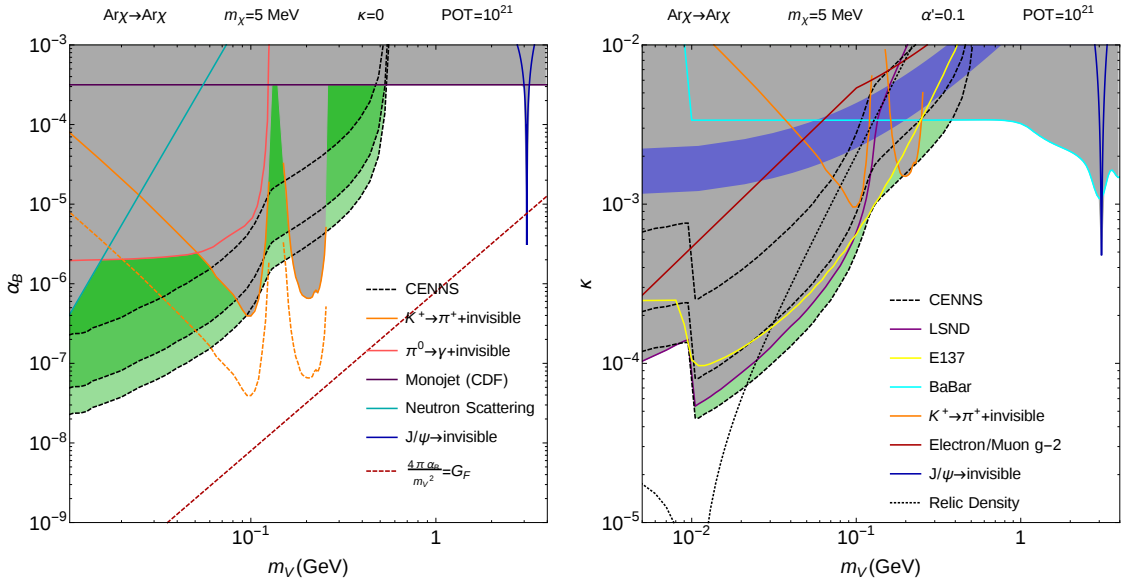

Figure 6.22: As with 6.21, but for CENNS.

Signal

For signal, we currently only include elastic scattering with electrons (see Fig. 6.23). Conversations with Walter Bonivento have led to cuts on the electron recoil distribu-

$e\chi \to e\chi$	
Efficiency	0.5
Electron Recoil	$E_e \in [2, 20]\,\mathrm{GeV}$
Scattering Angle	$\theta_e \in [10, 20]\,\mathrm{mrad}$
Event Limit	≈ 300

Table 6.6: Summary of cuts and efficiencies for the SHiP signal.

tion:

$$E_e \in [2, 20]\,\mathrm{GeV}, \quad \theta_e \in [10, 20]\,\mathrm{mrad},$$

where E_e and θ_e are the energy and angle of the recoiling electron, respectively. This cuts the expected beam related backgrounds to approximately 300 electron scattering events, while preserving much of the dark matter signal. SHiP possesses the potential to provide great sensitivity to the higher mass regions of the scenario parameter space, but will require a detector to be built which is actually sensitive to hidden sector dark matter scenarios.

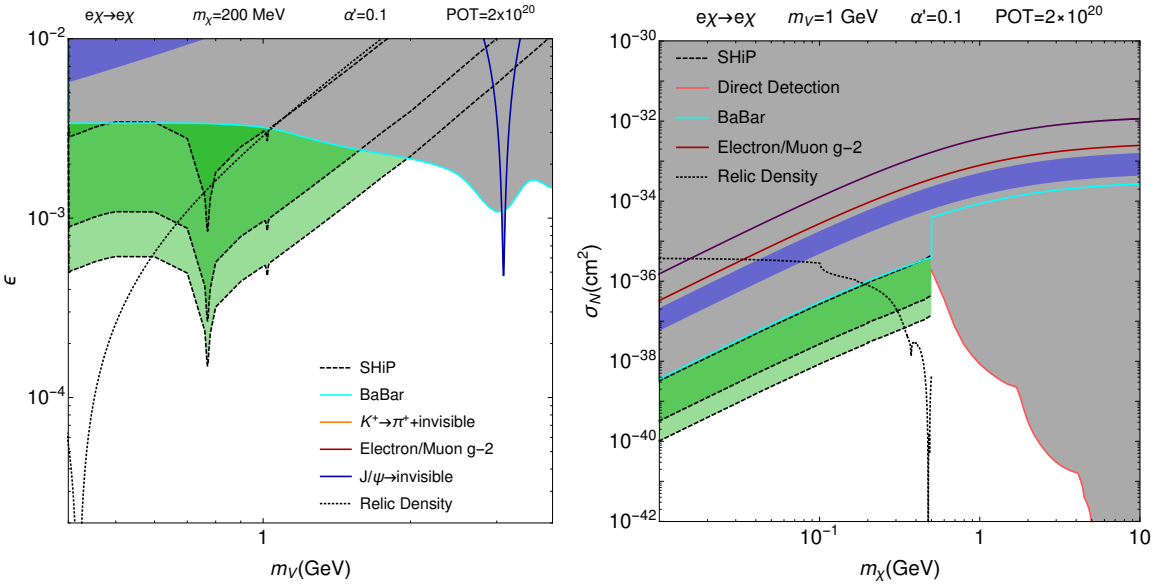

Figure 6.23: Sensitivity estimates for a possible version of the SHiP experiment. The small spike at $m_V = 1020\,\mathrm{MeV}$ corresponds to resonant ϕ production. SHiP could potentially impose constraints on the parameter space for predictions of more than 300 events. The SHiP experiment is capable of placing limits on comparatively large dark matter masses, and its reach in the parameter space is complimentary with the limits placed by the CRESST-II direct detection experiment.

Our current treatment of nuclear scattering is not appropriate for the high energies

expected at SHiP, as this is firmly in the regime of deep-inelastic scattering.

6.6 Other Experiments

DUNE

DUNE - the Deep Underground Neutrino Experiment[6] is a fixed target neutrino experiment that is planned to have the longest baseline in the world, sending a neutrino beam from the NUMI beamline at Fermilab to SURF, the Sanford Underground Research Facility, 1300 kilometers away in South Dakota[42]. The current design calls for a near detector in addition to the far detector, but the near detector designs under consideration are unlikely to be appropriate for a hidden sector dark matter search. A large liquid argon beam monitor in front of the near detector has also been considered, but would only be able to operate during low-intensity running modes. The far detector under consideration would be made of four 10-tonne liquid argon modules, for a total fiducial mass of 40 kilotonnes, which is a little smaller than Super-K.

The currently suggested experimental setup for the DUNE experiment seems unlikely to yield any interesting sensitivity that is not more easily attainable by Super-K or SHiP. If there was serious interest in using the DUNE beamline for a hidden sector dark matter search, one would have to propose some new off-axis detector (see [64] for one such possibility), or perhaps add a beam dump component to the experiment.

SBND

The Short-Baseline Neutrino Detector is a proposed liquid argon time projection chamber (LArTPC) located at the BNB. Its goal is to record and study very large numbers of unoscillated neutrino interactions in order to assist the Fermilab Short-Baseline Program, acting as a near detector for ICARUS and MicroBooNE[7]. Its current design specifies that it would be located 110 meters from the MiniBooNE target, and possess a fiducial volume of 112 tons. Purely from its detector size and location, it would possess a larger dark matter event rate than MiniBooNE, but it seems likely that neutrino backgrounds would be significant unless a run were conducted in a beam dump mode.

[6] Also known as LBNE, the Long-Baseline Neutrino Experiment, and LBNF, the Long-Baseline Neutrino Facility.

[7] See http://sbn-nd.fnal.gov/ for more details.

6.7 Summary

In this chapter we have considered the possible dark matter signals at a variety of proton beam fixed target experiments, some of which already exist while others are only in the planning stages. All of the experiments considered are capable of placing new limits on the hidden sector parameter space, but most require additional analysis.

For the kinetic mixing scenario, the best limits on lower mass ($m_V < m_{\pi^0}$) regions of the parameter space come from LSND. A MiniBooNE NCE electron-dark matter scattering analysis is capable of improving on all current low mass limits, while the coherent neutrino-nucleus scattering experiment COHERENT appears capable of placing the best limits on the same parameter space. For moderate masses of a few hundred MeV, the MiniBooNE π^0 inelastic scattering channel seems well placed to impose new constraints. For the largest masses, defined as $m_V > m_\eta$, an NCE nucleon scattering analysis using out of time data at Super-K seems like the surest option, as this is an existing experiment and the analysis has garnered some interest from members of the T2K collaboration. The signal efficiency actually increases with m_χ, as the timing cut becomes more effective as the time delay grows. The only experiment that shows promise of greater mass reach than Super-K is an NCE electron-dark matter scattering analysis at the SHiP experiment.

Many of the same experiments can place limits on the variant leptophobic parameter space, but signals from the inelastic π^0 production and NCE electron-dark matter scattering channels are heavily suppressed. COHERENT is capable of placing great limits on the low mass parameter space, while CENNS extends the sensitivity of coherent neutrino experiments to $m_V \approx m_\eta$. In the absence of a theory framework for a deep inelastic scattering at SHiP, Super-K provides the best tool for probing higher V and χ masses.

Chapter 7

Conclusion

The program of research presented in this work aimed to survey the sensitivity of fixed target proton colliders to hidden sector dark matter. We chose to focus on a scalar dark matter candidate with a vector mediator as it is straightforward for this scenario to satisfy relic density constraints without being heavily constrained or outright eliminated by other cosmological or particle physics limits. Keeping in mind the goal of maximizing the parameter space covered, two possible means of coupling to the Standard Model were considered, kinetic mixing between the the vector mediator and U(1) hypercharge, and coupling to baryon number without kinetic mixing, where the former has been referred to as the kinetic mixing scenario and the latter as the leptophobic scenario.

A large number of possible dark matter production channels were considered in order to make the best possible estimate of the dark matter production rate for scenarios with dark matter and mediator masses spanning three orders of magnitude, ranging from a few MeV to a few GeV. Finally, four possible dark matter signals have been considered: NCE electron-dark matter scattering, NCE nucleon-dark matter scattering, coherent nuclear-dark matter scattering and dark matter induced inelastic pion production. Missing from this list is deep inelastic scattering, which becomes very important at the highest energy fixed target experiments. While this was not complete at the time of writing, the calculation is in progress and should be complete before the publication of this dissertation.

The MiniBooNE collaboration took advantage of the growing interest in low mass hidden sector dark matter scenarios to motivate a dedicated beam dump run. To properly tailor an analysis to the hidden sector scenario would require far more than simply a signal estimate. Knowledge of the energy, angle, timing and position distri-

butions in the MiniBooNE detector would all be invaluable tools for differentiating between a dark matter and neutrino induced scattering event. In order to allow the MiniBooNE collaboration to generate this data, and provide it to any other experiment which should request it, a fixed target Dark Matter Monte Carlo code was created. The BdNMC code is capable of efficiently generating dark matter events for any of the signal channels considered in this work in both the leptophobic and kinetic mixing scenarios. Perhaps most useful to experiments, and as has been used in the MiniBooNE analysis, it can accept meson momenta and positions generated by their own beamline simulation in the place of a conventional production distribution parameterization.

In order to fully explore the parameter space, we have studied multiple proton fixed target experiments, as the different combinations of detector geometry, production energies and signal sensitivities enhanced the sensitivity of each to different mass ranges and couplings. While only LSND data has been used to place solid constraints on the scenario parameter space thus far, a dedicated NCE nucleon-dark matter scattering analysis is underway by the MiniBooNE collaboration using data from their aforementioned beam dump run, and is expected to place new limits on the hidden sector parameter space. The T2K experiment is also well placed to conduct a dark matter analysis using their Super-K far detector, and place new limits on the high mediator and dark matter mass regions of the parameter space. Several proposed fixed target experiments, such as SHiP, CENNS and COHERENT all show great promise as probes of hidden sector scenarios, and their collaborations have expressed varying levels of interest in pursuing such an analysis.

In summary, we have explored the sensitivity of all the most promising proton fixed target experiments both existing and in development to low mass hidden sector dark matter scenarios. Many possess the potential to place new limits on unconstrained regions of the parameter space, but will require dedicated experimental analyses to fully exploit their sensitivity. In order to render assistance in these analyses, we have written a Monte Carlo code capable of both simulating the production of dark matter and its interactions with Standard Model matter in a detector. With the cooperation of experimental collaborations, fixed target proton colliders are poised to significantly improve limits on both hidden sector scenarios considered over a wide range of scenario parameters.

Appendix A

MiniBooNE Beam Dump Running

Early work on the sensitivity of fixed target neutrino experiments to light dark matter attracted the interest of the MiniBooNE collaboration. Collaboration members indicated that MiniBooNE could be run in a beam off-target mode by redirecting the proton beam around the target and directly into the beam dump at the end of the decay pipe. This would allow MiniBooNE to become a beam dump experiment, reducing the neutrino backgrounds by one to two orders of magnitude. I provided assistance in writing a proposal for a new MiniBooNE run presented to the Fermilab Physics Advisory Committee, "Low Mass WIMP Searches with a Neutrino Experiment: A Proposal for Further MiniBooNE Running," [14] contributing to the earliest versions of several plots shown in chapter 6. The proposal was eventually accepted, and I joined the collaboration shortly before the beam dump run began. The MiniBooNE experiment operated in beam dump mode from November 2013 to September 2014.

The current objective of the collaboration is to produce a measurement of neutral current elastic nucleon scattering events. Any excess in this scattering rate could indicate the presence of hidden sector particles such as low mass dark matter. The collaboration will produce a model independent analysis, providing counts of excess scattering events over a number of nucleon recoil energy bins, as well as performing their own in-depth analysis of the data to place limits on kinetically mixed hidden sector dark matter. My contributions since joining the collaboration are summarized below:

- Worked 18 twelve-hour detector monitoring shifts.
  - In order to become an author on MiniBooNE papers, each collaboration

member must work a minimum number of detector monitoring shifts. A MiniBooNE shifter monitors the operation of the MiniBooNE detector, target and beamline. Their main responsibility is to act as a point of contact for the Fermilab Main Control Room (MCR) and to watch for anomalous behavior, such as a significant drift in the beam spot, automated detector alarms or loss of beam. Should anomalous behavior persist, they contact the appropriate experts by phone for further instructions. Shifters act as filters for transient self-correcting issues that would lead to unnecessary calls for the attention of the experts. They also document the running of the beamline and detector during their shift, recording any loss of beam or unusual behavior and producing beam summary plots at the end of their shift.

- Wrote the MiniBooNE dark matter Monte Carlo with Brian Batell.
  - I am the primary maintainer of the code, and updated it with features requested by the MiniBooNE collaboration. I instructed MiniBooNE collaboration members on its use, and provided technical support.
- Attended the weekly MiniBooNE collaboration meetings.
  - At these meetings I answered questions about dark matter theory and phenomenology and provided feedback on conference talks and posters produced by members of the collaboration. On occasion, I have presented talks of my own in order to update the collaboration on new features of the simulation or theory developments of interest to the MiniBooNE collaboration.
- Contributed to the MiniBooNE beam dump run related paper in preparation.
  - I wrote portions of the theory section of the paper, as well as preparing short descriptions of the dark matter simulation used.
- With Brian Batell, tested MiniBooNE's model independent neutral current elastic nucleon-dark matter scattering limits by performing our own statistical analysis. This will act as a cross check on MiniBooNE's own analysis.

Appendix B

Sample Parameter Card

This card implements a run for the MiniBooNE experiment in beam off-target running mode. It showcases correct formatting for a somewhat complicated run with multiple production modes and a series of cuts on the kinematics of the end state nucleon.

```
#Parameter Card
#All masses should be provided in GeV, all lengths in meters.
#Lines preceded by a # are ignored by the parser.

#Seed with which to initialize the RNG.
seed 114234

#Give your run a name. If no name is supplied, one will be
#generated from the current time.
run 14506

#Model Parameters
epsilon 1e-3
dark_matter_mass 0.01
dark_photon_mass 0.2
alpha_D 0.1

#Run parameters
POT 2e20
pi0_per_POT 0.9
```

```
samplesize 20000

burn_max 1000
burn_timeout 20000

beam_energy 8.9

#Production Parameters
#Declaring a production channel
production_channel pi0_decay

#Choosing a production distribution is optional, but it must
#be grouped with the relevant production_channel entry
production_distribution pi0_sanfordwang

#Choose your own fit for the sanfordwang distribution.
#An example set is provided.
#If this is not set, the default values will be used.
sanfordwang_file sanfordwang_parameters.dat

#Here we also call a second production mode.
production_channel eta_decay
production_distribution k0_sanfordwang
#Optionally, you may specify a number of pi0s per meson
meson_per_pi0 0.0333

#This invokes the bremsstrahlung production channel.
production_channel V_decay
production_distribution proton_brem
ptmax 0.2
zmin 0.3
zmax 0.7

#Scattering Parameters
signal_channel NCE_nucleon
```

```
efficiency 0.35

#Filepath to write events.
output_file Events/events.dat
#Filepath to write a summary of the run with number of events
#and paramaters
summary_file Events/summary.dat

#In comprehensive mode, all particles that make up an event
#are written to the output file. This overwrites the output
#file.
output_mode comprehensive

#Cuts on the kinetic energy of outgoing nucleon or electron.
#These default to min=0 and max=1e9 GeV
max_scatter_energy 0.9
min_scatter_energy 0.035
#Decreasing the resolution increases setup time but improves
#accuracy of scattering cross section.
dm_energy_resolution 0.01

#Detector Parameters
detector sphere
x-position 0.0
y-position -1.9
z-position 491.0
radius 5.0

#Material parameters
#Mass is set in GeV.
#anything not defined will be set to zero.
material Carbon
number_density 3.63471e22
proton_number 6
neutron_number 6
```

```
electron_number 6
mass 11.2593

material Hydrogen
number_density 7.26942e22
proton_number 1
neutron_number 0
electron_number 1
mass 0.945778
```

Bibliography

[1] M. S. Roberts and R. N. Whitehurst, "The rotation curve and geometry of M31 at large galactocentric distances.," *Astrophys. J.* **201** (Oct., 1975) 327–346.

[2] L. Baudis, "WIMP Dark Matter Direct-Detection Searches in Noble Gases," *Phys. Dark Univ.* **4** (2014) 50–59, arXiv:1408.4371 [astro-ph.IM].

[3] I. V. Moskalenko and A. W. Strong, "Production and propagation of cosmic ray positrons and electrons," *Astrophys. J.* **493** (1998) 694–707, arXiv:astro-ph/9710124 [astro-ph].

[4] **PAMELA** Collaboration, O. Adriani *et al.*, "An anomalous positron abundance in cosmic rays with energies 1.5-100 GeV," *Nature* **458** (2009) 607–609, arXiv:0810.4995 [astro-ph].

[5] **XENON100** Collaboration, E. Aprile *et al.*, "Dark Matter Results from 225 Live Days of XENON100 Data," *Phys. Rev. Lett.* **109** (2012) 181301, arXiv:1207.5988 [astro-ph.CO].

[6] **XENON10** Collaboration, J. Angle *et al.*, "A search for light dark matter in XENON10 data," *Phys. Rev. Lett.* **107** (2011) 051301, arXiv:1104.3088 [astro-ph.CO]. [Erratum: Phys. Rev. Lett.110,249901(2013)].

[7] **CRESST-II** Collaboration, G. Angloher *et al.*, "Results on low mass WIMPs using an upgraded CRESST-II detector," *Eur. Phys. J.* **C74** no. 12, (2014) 3184, arXiv:1407.3146 [astro-ph.CO].

[8] **CRESST** Collaboration, G. Angloher *et al.*, "Results on light dark matter particles with a low-threshold CRESST-II detector," *Eur. Phys. J.* **C76** no. 1, (2016) 25, arXiv:1509.01515 [astro-ph.CO].

[9] **DAMIC** Collaboration, J. Barreto *et al.*, "Direct Search for Low Mass Dark Matter Particles with CCDs," *Phys. Lett.* **B711** (2012) 264–269, arXiv:1105.5191 [astro-ph.IM].

[10] **SuperCDMS** Collaboration, R. Agnese *et al.*, "Search for Low-Mass Weakly Interacting Massive Particles with SuperCDMS," *Phys. Rev. Lett.* **112** no. 24, (2014) 241302, arXiv:1402.7137 [hep-ex].

[11] **SuperCDMS** Collaboration, R. Agnese *et al.*, "New Results from the Search for Low-Mass Weakly Interacting Massive Particles with the CDMS Low Ionization Threshold Experiment," *Phys. Rev. Lett.* **116** no. 7, (2016) 071301, arXiv:1509.02448 [astro-ph.CO].

[12] **LUX** Collaboration, D. S. Akerib *et al.*, "Improved WIMP scattering limits from the LUX experiment," arXiv:1512.03506 [astro-ph.CO].

[13] P. Jean, J. Knodlseder, W. Gillard, N. Guessoum, K. Ferriere, A. Marcowith, V. Lonjou, and J. P. Roques, "Spectral analysis of the galactic e+ e- annihilation emission," *Astron. Astrophys.* **445** (2006) 579–589, arXiv:astro-ph/0509298 [astro-ph].

[14] **MiniBooNE** Collaboration, R. Dharmapalan *et al.*, "Low Mass WIMP Searches with a Neutrino Experiment: A Proposal for Further MiniBooNE Running," arXiv:1211.2258 [hep-ex].

[15] B. Batell, P. deNiverville, D. McKeen, M. Pospelov, and A. Ritz, "Leptophobic Dark Matter at Neutrino Factories," *Phys. Rev.* **D90** no. 11, (2014) 115014, arXiv:1405.7049 [hep-ph].

[16] R. Essig *et al.*, "Working Group Report: New Light Weakly Coupled Particles," in *Community Summer Study 2013: Snowmass on the Mississippi (CSS2013) Minneapolis, MN, USA, July 29-August 6, 2013*. 2013. arXiv:1311.0029 [hep-ph]. http://inspirehep.net/record/1263039/files/arXiv:1311.0029.pdf.

[17] A. Faessler, M. I. Krivoruchenko, and B. V. Martemyanov, "Once more on electromagnetic form factors of nucleons in extended vector meson dominance model," *Phys. Rev.* **C82** (2010) 038201, arXiv:0910.5589 [hep-ph].

[18] **MiniBooNE** Collaboration, A. A. Aguilar-Arevalo *et al.*, "Measurement of nu(mu) and anti-nu(mu) induced neutral current single pi0 production cross sections on mineral oil at E(nu) O(1- GeV)," *Phys. Rev.* **D81** (2010) 013005, arXiv:0911.2063 [hep-ex].

[19] **T2K** Collaboration, K. Abe *et al.*, "The T2K Experiment," *Nucl. Instrum. Meth.* **A659** (2011) 106–135, arXiv:1106.1238 [physics.ins-det].

[20] J. I. Collar, N. E. Fields, M. Hai, T. W. Hossbach, J. L. Orrell, C. T. Overman, G. Perumpilly, and B. Scholz, "Coherent neutrino-nucleus scattering detection with a CsI[Na] scintillator at the SNS spallation source," *Nucl. Instrum. Meth.* **A773** (2015) 56–65, arXiv:1407.7524 [physics.ins-det].

[21] S. J. Brice *et al.*, "A method for measuring coherent elastic neutrino-nucleus scattering at a far off-axis high-energy neutrino beam target," *Phys. Rev.* **D89** no. 7, (2014) 072004, arXiv:1311.5958 [physics.ins-det].

[22] P. deNiverville, M. Pospelov, and A. Ritz, "Light new physics in coherent neutrino-nucleus scattering experiments," *Phys. Rev.* **D92** no. 9, (2015) 095005, arXiv:1505.07805 [hep-ph].

[23] G. Weidenspointner *et al.*, "An asymmetric distribution of positrons in the Galactic disk revealed by gamma-rays," *Nature* **451** (2008) 159–162.

[24] N. Prantzos, C. Boehm, A. Bykov, R. Diehl, K. Ferriere, *et al.*, "The 511 keV emission from positron annihilation in the Galaxy," arXiv:1009.4620 [astro-ph.HE]. arXiv:1009.4620 [astro-ph.HE].

[25] G. B. Gelmini, "TASI 2014 Lectures: The Hunt for Dark Matter," in *Theoretical Advanced Study Institute in Elementary Particle Physics: Journeys Through the Precision Frontier: Amplitudes for Colliders (TASI 2014) Boulder, Colorado, June 2-27, 2014*. 2015. arXiv:1502.01320 [hep-ph].
http://inspirehep.net/record/1342951/files/arXiv:1502.01320.pdf.

[26] B. W. Lee and S. Weinberg, "Cosmological Lower Bound on Heavy Neutrino Masses," *Phys. Rev. Lett.* **39** (1977) 165–168.

[27] C. Boehm and P. Fayet, "Scalar Dark Matter candidates," *Nucl.Phys.* **B683** (2004) 219–263, arXiv:hep-ph/0305261 [hep-ph].

[28] P. Fayet, "Light spin-$\frac{1}{2}$ or spin-0 Dark Matter particles," *Phys. Rev.* **D70** (2004) 023514, arXiv:hep-ph/0403226.

[29] P. Fayet, "Constraints on Light Dark Matter and U bosons, from ψ, Υ, K^+, π^0, η and η' decays," *Phys. Rev.* **D74** (2006) 054034, arXiv:hep-ph/0607318.

[30] P. Fayet, "U-boson production in e^+ e^- annihilations, ψ and Υ decays, and Light Dark Matter," *Phys.Rev.* **D75** (2007) 115017, arXiv:hep-ph/0702176 [HEP-PH].

[31] M. Pospelov, A. Ritz, and M. B. Voloshin, "Secluded WIMP Dark Matter," *Phys.Lett.* **B662** (2008) 53–61, arXiv:0711.4866 [hep-ph].

[32] D. Hooper and K. M. Zurek, "A Natural Supersymmetric Model with MeV Dark Matter," *Phys.Rev.* **D77** (2008) 087302, arXiv:0801.3686 [hep-ph].

[33] B. Batell, M. Pospelov, and A. Ritz, "Exploring Portals to a Hidden Sector Through Fixed Targets," *Phys.Rev.* **D80** (2009) 095024, arXiv:0906.5614 [hep-ph].

[34] N. Borodatchenkova, D. Choudhury, and M. Drees, "Probing MeV Dark Matter at Low-Energy e^+ e^- Colliders," *Phys. Rev. Lett.* **96** (2006) 141802, arXiv:hep-ph/0510147.

[35] R. Essig, P. Schuster, and N. Toro, "Probing Dark Forces and Light Hidden Sectors at Low-Energy e^+e^- Colliders," *Phys.Rev.* **D80** (2009) 015003, arXiv:0903.3941 [hep-ph].

[36] M. Reece and L.-T. Wang, "Searching for the light dark gauge boson in GeV-scale experiments," *JHEP* **0907** (2009) 051, arXiv:0904.1743 [hep-ph].

[37] J. D. Bjorken, R. Essig, P. Schuster, and N. Toro, "New Fixed-Target Experiments to Search for Dark Gauge Forces," *Phys.Rev.* **D80** (2009) 075018, arXiv:0906.0580 [hep-ph].

[38] M. D. Diamond and P. Schuster, "Searching for Light Dark Matter with the SLAC Millicharge Experiment," *Phys. Rev. Lett.* **111** no. 22, (2013) 221803, arXiv:1307.6861 [hep-ph].

[39] E. Izaguirre, G. Krnjaic, P. Schuster, and N. Toro, "Physics motivation for a pilot dark matter search at Jefferson Laboratory," *Phys. Rev.* **D90** no. 1, (2014) 014052, arXiv:1403.6826 [hep-ph].

[40] B. Batell, R. Essig, and Z. Surujon, "Strong Constraints on Sub-GeV Dark Sectors from SLAC Beam Dump E137," *Phys. Rev. Lett.* **113** no. 17, (2014) 171802, arXiv:1406.2698 [hep-ph].

[41] Y. Kahn, G. Krnjaic, J. Thaler, and M. Toups, "DAEdALUS and dark matter detection," *Phys. Rev.* **D91** no. 5, (2015) 055006, arXiv:1411.1055 [hep-ph].

[42] **DUNE** Collaboration, R. Acciarri *et al.*, "Long-Baseline Neutrino Facility (LBNF) and Deep Underground Neutrino Experiment (DUNE)," arXiv:1601.05471 [physics.ins-det].

[43] J. Hewett, H. Weerts, R. Brock, J. Butler, B. Casey, *et al.*, "Fundamental Physics at the Intensity Frontier," arXiv:1205.2671 [hep-ex].

[44] A. S. Kronfeld, R. S. Tschirhart, U. Al-Binni, W. Altmannshofer, C. Ankenbrandt, *et al.*, "Project X: Physics Opportunities," arXiv:1306.5009 [hep-ex].

[45] M. Pospelov, "Secluded U(1) below the weak scale," *Phys. Rev.* **D80** (2009) 095002, arXiv:0811.1030 [hep-ph].

[46] B. Batell, M. Pospelov, and A. Ritz, "Probing a Secluded U(1) at B-factories," *Phys. Rev.* **D79** (2009) 115008, arXiv:0903.0363 [hep-ph].

[47] M. Freytsis, G. Ovanesyan, and J. Thaler, "Dark Force Detection in Low Energy e-p Collisions," *JHEP* **1001** (2010) 111, arXiv:0909.2862 [hep-ph].

[48] B. Batell, M. Pospelov, and A. Ritz, "Multi-lepton Signatures of a Hidden Sector in Rare B Decays," *Phys.Rev.* **D83** (2011) 054005, arXiv:0911.4938 [hep-ph].

[49] M. Freytsis, Z. Ligeti, and J. Thaler, "Constraining the Axion Portal with $B \to K l^+ l^-$," *Phys. Rev.* **D81** (2010) 034001, arXiv:0911.5355 [hep-ph].

[50] R. Essig, P. Schuster, N. Toro, and B. Wojtsekhowski, "An Electron Fixed Target Experiment to Search for a New Vector Boson A' Decaying to e+e-," *JHEP* **1102** (2011) 009, arXiv:1001.2557 [hep-ph].

[51] R. Essig, R. Harnik, J. Kaplan, and N. Toro, "Discovering New Light States at Neutrino Experiments," *Phys.Rev.* **D82** (2010) 113008, arXiv:1008.0636 [hep-ph].

[52] K. L. McDonald and D. E. Morrissey, "Low-Energy Signals from Kinetic Mixing with a Warped Abelian Hidden Sector," *JHEP* **1102** (2011) 087, arXiv:1010.5999 [hep-ph].

[53] M. Williams, C. Burgess, A. Maharana, and F. Quevedo, "New Constraints (and Motivations) for Abelian Gauge Bosons in the MeV-TeV Mass Range," *JHEP* **1108** (2011) 106, arXiv:1103.4556 [hep-ph].

[54] **APEX Collaboration** Collaboration, S. Abrahamyan *et al.*, "Search for a New Gauge Boson in Electron-Nucleus Fixed-Target Scattering by the APEX Experiment," *Phys.Rev.Lett.* **107** (2011) 191804, arXiv:1108.2750 [hep-ex].

[55] F. Archilli, D. Babusci, D. Badoni, I. Balwierz, G. Bencivenni, *et al.*, "Search for a vector gauge boson in phi meson decays with the KLOE detector," *Phys.Lett.* **B706** (2012) 251–255, arXiv:1110.0411 [hep-ex].

[56] **BaBar Collaboration** Collaboration, J. Lees *et al.*, "Search for Low-Mass Dark-Sector Higgs Bosons," *Phys.Rev.Lett.* **108** (2012) 211801, arXiv:1202.1313 [hep-ex].

[57] H. Davoudiasl, H.-S. Lee, and W. J. Marciano, "'Dark' Z implications for Parity Violation, Rare Meson Decays, and Higgs Physics," *Phys.Rev.* **D85** (2012) 115019, arXiv:1203.2947 [hep-ph].

[58] Y. Kahn and J. Thaler, "Searching for an invisible A' vector boson with DarkLight," *Phys.Rev.* **D86** (2012) 115012, arXiv:1209.0777 [hep-ph].

[59] S. Andreas, C. Niebuhr, and A. Ringwald, "New Limits on Hidden Photons from Past Electron Beam Dumps," *Phys.Rev.* **D86** (2012) 095019, arXiv:1209.6083 [hep-ph].

[60] R. Essig, J. Mardon, M. Papucci, T. Volansky, and Y.-M. Zhong, "Constraining Light Dark Matter with Low-Energy e^+e^- Colliders," *JHEP* **11** (2013) 167, arXiv:1309.5084 [hep-ph].

[61] H. Davoudiasl and I. M. Lewis, "Dark Matter from Hidden Forces," *Phys.Rev.* **D89** (2014) 055026, arXiv:1309.6640 [hep-ph].

[62] D. E. Morrissey and A. P. Spray, "New Limits on Light Hidden Sectors from Fixed-Target Experiments," arXiv:1402.4817 [hep-ph].

[63] **KLOE-2 Collaboration** Collaboration, D. Babusci *et al.*, "Limit on light gauge boson production in $e^+e^- \to \mu^+\mu^-\gamma$ interactions with the KLOE experiment," arXiv:1404.7772 [hep-ex].

[64] P. Coloma, B. A. Dobrescu, C. Frugiuele, and R. Harnik, "Dark matter beams at LBNF," *JHEP* **04** (2016) 047, arXiv:1512.03852 [hep-ph].

[65] P. deNiverville, M. Pospelov, and A. Ritz, "Observing a light dark matter beam with neutrino experiments," *Phys. Rev.* **D84** (2011) 075020, arXiv:1107.4580 [hep-ph].

[66] P. deNiverville, D. McKeen, and A. Ritz, "Signatures of sub-GeV dark matter beams at neutrino experiments," *Phys. Rev.* **D86** (2012) 035022, arXiv:1205.3499 [hep-ph].

[67] S. Alekhin *et al.*, "A facility to Search for Hidden Particles at the CERN SPS: the SHiP physics case," arXiv:1504.04855 [hep-ph].

[68] **Particle Data Group** Collaboration, K. A. Olive *et al.*, "Review of Particle Physics," *Chin. Phys.* **C38** (2014) 090001.

[69] G. Bertone, D. Hooper, and J. Silk, "Particle Dark Matter: Evidence, Candidates and Constraints," *Phys.Rept.* **405** (2005) 279–390, arXiv:hep-ph/0404175 [hep-ph].

[70] M. Lisanti, "Lectures on Dark Matter Physics," in *Theoretical Advanced Study Institute in Elementary Particle Physics: New Frontiers in Fields and Strings (TASI 2015) Boulder, CO, USA, June 1-26, 2015*. 2016. arXiv:1603.03797 [hep-ph].
http://inspirehep.net/record/1427360/files/arXiv:1603.03797.pdf.

[71] P. Gorenstein and W. Tucker, "Astronomical Signatures of Dark Matter," *Adv. High Energy Phys.* **2014** (2014) 878203.

[72] T. Marrodán Undagoitia and L. Rauch, "Dark matter direct-detection experiments," *J. Phys.* **G43** no. 1, (2016) 013001, arXiv:1509.08767 [physics.ins-det].

[73] F. Zwicky, "Spectral displacement of extra galactic nebulae," *Helv.Phys.Acta* **6** (1933) 110–127.

[74] F. Zwicky, "On the Masses of Nebulae and of Clusters of Nebulae," *Astrophys. J.* **86** (Oct., 1937) 217.

[75] V. C. Rubin and W. K. Ford, Jr., "Rotation of the Andromeda Nebula from a Spectroscopic Survey of Emission Regions," *Astrophys. J.* **159** (1970) 379–403.

[76] D. Zaritsky, R. Smith, C. Frenk, and S. D. M. White, "Satellites of spiral galaxies," *Astrophys. J.* **405** (Mar., 1993) 464–478.

[77] D. Zaritsky, R. Smith, C. Frenk, and S. D. M. White, "More satellites of spiral galaxies," *Astrophys. J.* **478** (1997) 39–48, arXiv:astro-ph/9611199 [astro-ph].

[78] M. Azzaro, F. Prada, and C. M. Gutierrez, "Motion properties of satellites around external spiral galaxies," *ASP Conf. Ser.* **327** (2004) 268, arXiv:astro-ph/0310487 [astro-ph].

[79] E. Olszewski, M. Mateo, S. Vogt, and M. Keane, "The internal kinematics of the leo ii dwarf spheroidal galaxy," in *Bulletin of the American Astronomical Society*, vol. 26, p. 1395. 1994.

[80] H. Hoekstra, H. Yee, and M. Gladders, "Current status of weak gravitational lensing," *New Astron. Rev.* **46** (2002) 767–781, arXiv:astro-ph/0205205 [astro-ph].

[81] M. Mateo, "Dwarf galaxies of the Local Group," *Ann. Rev. Astron. Astrophys.* **36** (1998) 435–506, arXiv:astro-ph/9810070 [astro-ph].

[82] R. B. Metcalf, L. A. Moustakas, A. J. Bunker, and I. R. Parry, "Spectroscopic gravitational lensing and limits on the dark matter substructure in

Q2237+0305," *Astrophys. J.* **607** (2004) 43–59, arXiv:astro-ph/0309738 [astro-ph].

[83] L. A. Moustakas and R. B. Metcalf, "Detecting dark matter substructure spectroscopically in strong gravitational lenses," *Mon. Not. Roy. Astron. Soc.* **339** (2003) 607, arXiv:astro-ph/0206176 [astro-ph].

[84] M. Milgrom, "A modification of the Newtonian dynamics as a possible alternative to the hidden mass hypothesis," *Astrophys. J.* **270** (July, 1983) 365–370.

[85] J. D. Bekenstein, "The Modified Newtonian Dynamics: MOND and its implications for new physics," *Contemp. Phys.* **47** (2006) 387, arXiv:astro-ph/0701848 [ASTRO-PH].

[86] M. Markevitch, "Chandra observation of the most interesting cluster in the universe," arXiv:astro-ph/0511345 [astro-ph]. [ESA Spec. Publ.604,723(2006)].

[87] D. Clowe, M. Bradac, A. H. Gonzalez, M. Markevitch, S. W. Randall, C. Jones, and D. Zaritsky, "A direct empirical proof of the existence of dark matter," *Astrophys. J.* **648** (2006) L109–L113, arXiv:astro-ph/0608407 [astro-ph].

[88] **Planck** Collaboration, R. Adam *et al.*, "Planck 2015 results. I. Overview of products and scientific results," arXiv:1502.01582 [astro-ph.CO].

[89] **WMAP Collaboration** Collaboration, E. Komatsu *et al.*, "Five-Year Wilkinson Microwave Anisotropy Probe (WMAP) Observations: Cosmological Interpretation," *Astrophys.J.Suppl.* **180** (2009) 330–376, arXiv:0803.0547 [astro-ph].

[90] **WMAP** Collaboration, J. Dunkley *et al.*, "Five-Year Wilkinson Microwave Anisotropy Probe (WMAP) Observations: Likelihoods and Parameters from the WMAP data," *Astrophys. J. Suppl.* **180** (2009) 306–329, arXiv:0803.0586 [astro-ph].

[91] G. F. Smoot *et al.*, "Structure in the COBE differential microwave radiometer first year maps," *Astrophys. J.* **396** (1992) L1–L5.

[92] G. Steigman, "Primordial Nucleosynthesis in the Precision Cosmology Era," *Ann. Rev. Nucl. Part. Sci.* **57** (2007) 463–491, arXiv:0712.1100 [astro-ph].

[93] R. A. C. Croft, D. H. Weinberg, M. Bolte, S. Burles, L. Hernquist, N. Katz, D. Kirkman, and D. Tytler, "Towards a precise measurement of matter clustering: Lyman alpha forest data at redshifts 2-4," *Astrophys. J.* **581** (2002) 20–52, arXiv:astro-ph/0012324 [astro-ph].

[94] D. H. Weinberg, R. Dave, N. Katz, and J. A. Kollmeier, "The Lyman - alpha forest as a cosmological tool," *AIP Conf. Proc.* **666** (2003) 157–169, arXiv:astro-ph/0301186 [astro-ph]. [,157(2003)].

[95] J. L. Feng, "Non-WIMP Candidates," arXiv:1002.3828 [hep-ph].

[96] G. Gelmini and P. Gondolo, "DM Production Mechanisms," arXiv:1009.3690 [astro-ph.CO].

[97] S. Archambault *et al.*, "Dark Matter Spin-Dependent Limits for WIMP Interactions on F-19 by PICASSO," *Phys. Lett.* **B682** (2009) 185–192, arXiv:0907.0307 [hep-ex].

[98] M. Felizardo, T. A. Girard, T. Morlat, A. C. Fernandes, A. R. Ramos, J. G. Marques, A. Kling, J. Puibasset, M. Auguste, D. Boyer, A. Cavaillou, J. Poupeney, C. Sudre, F. P. Carvalho, M. I. Prudêncio, and R. Marques, "The simple phase ii dark matter search," *Phys. Rev. D* **89** (Apr, 2014) 072013. http://link.aps.org/doi/10.1103/PhysRevD.89.072013.

[99] **COUPP** Collaboration, E. Behnke *et al.*, "Improved Spin-Dependent WIMP Limits from a Bubble Chamber," *Science* **319** (2008) 933–936, arXiv:0804.2886 [astro-ph].

[100] R. Bernabei *et al.*, "Final model independent result of DAMA/LIBRA-phase1," *Eur. Phys. J.* **C73** (2013) 2648, arXiv:1308.5109 [astro-ph.GA].

[101] C. E. Aalseth *et al.*, "Maximum Likelihood Signal Extraction Method Applied to 3.4 years of CoGeNT Data," arXiv:1401.6234 [astro-ph.CO].

[102] J. Battat, J. Brack, E. Daw, A. Dorofeev, A. Ezeribe, J. Fox, J.-L. Gauvreau, M. Gold, L. Harmon, J. Harton, J. Landers, E. Lee, D. Loomba, J. Matthews,

E. Miller, A. Monte, A. Murphy, S. Paling, N. Phan, M. Pipe, M. Robinson, S. Sadler, A. Scarff, D. Snowden-Ifft, N. Spooner, S. Telfer, D. Walker, D. Warner, and L. Yuriev, "Radon in the drift-ii directional dark matter tpc: emanation, detection and mitigation," *Journal of Instrumentation* **9** no. 11, (2014) P11004. http://stacks.iop.org/1748-0221/9/i=11/a=P11004.

[103] **IceCube** Collaboration, M. G. Aartsen *et al.*, "Search for dark matter annihilations in the Sun with the 79-string IceCube detector," *Phys. Rev. Lett.* **110** no. 13, (2013) 131302, arXiv:1212.4097 [astro-ph.HE].

[104] **Fermi-LAT** Collaboration, W. B. Atwood *et al.*, "The Large Area Telescope on the Fermi Gamma-ray Space Telescope Mission," *Astrophys. J.* **697** (2009) 1071–1102, arXiv:0902.1089 [astro-ph.IM].

[105] A. Kohnle, J. Mattes, G. Hermann, W. Hofmann, and M. Panter, "Photodetectors for {HESS}," *Nuclear Instruments and Methods in Physics Research Section A: Accelerators, Spectrometers, Detectors and Associated Equipment* **442** no. 1–3, (2000) 322 – 326. http://www.sciencedirect.com/science/article/pii/S0168900299012437.

[106] **MAGIC** Collaboration, H. Anderhub *et al.*, "SEARCH FOR VERY HIGH ENERGY GAMMA-RAY EMISSION FROM PULSAR-PULSAR WIND NEBULA SYSTEMS WITH THE MAGIC TELESCOPE," *Astrophys. J.* **710** no. 1, (2010) 828–835.

[107] **Whipple, VERITAS** Collaboration, R. W. Lessard, "TeV gamma-ray astronomy at the Whipple observatory," in *High-energy physics. Proceedings, 29th International Conference, ICHEP'98, Vancouver, Canada, July 23-29, 1998. Vol. 1, 2.* 1998.

[108] **Fermi-LAT** Collaboration, M. Ackermann *et al.*, "Measurement of separate cosmic-ray electron and positron spectra with the Fermi Large Area Telescope," *Phys. Rev. Lett.* **108** (2012) 011103, arXiv:1109.0521 [astro-ph.HE].

[109] **AMS** Collaboration, M. Aguilar *et al.*, "First Result from the Alpha Magnetic Spectrometer on the International Space Station: Precision Measurement of the Positron Fraction in Primary Cosmic Rays of 0.5–350 GeV," *Phys. Rev. Lett.* **110** (2013) 141102.

[110] J. Abdallah *et al.*, "Simplified Models for Dark Matter Searches at the LHC," *Phys. Dark Univ.* **9-10** (2015) 8–23, arXiv:1506.03116 [hep-ph].

[111] C. Boehm, T. A. Ensslin, and J. Silk, "Can Annihilating dark matter be lighter than a few GeVs?," *J. Phys.* **G30** (2004) 279–286, arXiv:astro-ph/0208458 [astro-ph].

[112] B. Patt and F. Wilczek, "Higgs-field portal into hidden sectors," arXiv:hep-ph/0605188. arXiv:hep-ph/0605188.

[113] R. Foot and X.-G. He, "Comment on Z-Z′ mixing in extended gauge theories," *Phys.Lett.* **B267** (1991) 509–512.

[114] D. Cerdeno, A. Dedes, and T. Underwood, "The Minimal Phantom Sector of the Standard Model: Higgs Phenomenology and Dirac Leptogenesis," *JHEP* **0609** (2006) 067, arXiv:hep-ph/0607157 [hep-ph].

[115] M. Ahlers, J. Jaeckel, J. Redondo, and A. Ringwald, "Probing Hidden Sector Photons through the Higgs Window," *Phys.Rev.* **D78** (2008) 075005, arXiv:0807.4143 [hep-ph].

[116] J. L. Feng, H. Tu, and H.-B. Yu, "Thermal Relics in Hidden Sectors," *JCAP* **0810** (2008) 043, arXiv:0808.2318 [hep-ph].

[117] P. Fayet, D. Hooper, and G. Sigl, "Constraints on Light Dark Matter From Core-Collapse Supernovae," *Phys.Rev.Lett.* **96** (2006) 211302, arXiv:hep-ph/0602169 [hep-ph].

[118] N. Padmanabhan and D. P. Finkbeiner, "Detecting dark matter annihilation with CMB polarization: Signatures and experimental prospects," *Phys. Rev.* **D72** (2005) 023508, arXiv:astro-ph/0503486 [astro-ph].

[119] L. Lopez-Honorez, O. Mena, S. Palomares-Ruiz, and A. C. Vincent, "Constraints on dark matter annihilation from CMB observationsbefore Planck," *JCAP* **1307** (2013) 046, arXiv:1303.5094 [astro-ph.CO].

[120] S. Galli, T. R. Slatyer, M. Valdes, and F. Iocco, "Systematic Uncertainties In Constraining Dark Matter Annihilation From The Cosmic Microwave Background," *Phys. Rev.* **D88** (2013) 063502, arXiv:1306.0563 [astro-ph.CO].

[121] K. Petraki and R. R. Volkas, "Review of asymmetric dark matter," *Int. J. Mod. Phys.* **A28** (2013) 1330028, arXiv:1305.4939 [hep-ph].

[122] J. D. Bjorken, S. Ecklund, W. R. Nelson, A. Abashian, C. Church, B. Lu, L. W. Mo, T. A. Nunamaker, and P. Rassmann, "Search for Neutral Metastable Penetrating Particles Produced in the SLAC Beam Dump," *Phys. Rev.* **D38** (1988) 3375.

[123] E. Izaguirre, G. Krnjaic, P. Schuster, and N. Toro, "New Electron Beam-Dump Experiments to Search for MeV to few-GeV Dark Matter," *Phys. Rev.* **D88** (2013) 114015, arXiv:1307.6554 [hep-ph].

[124] **LSND** Collaboration, L. B. Auerbach *et al.*, "Measurement of electron - neutrino - electron elastic scattering," *Phys. Rev.* **D63** (2001) 112001, arXiv:hep-ex/0101039 [hep-ex].

[125] **BaBar** Collaboration, B. Aubert *et al.*, "Search for Invisible Decays of a Light Scalar in Radiative Transitions $\upsilon_{3S} \to \gamma$ A0," in *Proceedings, 34th International Conference on High Energy Physics (ICHEP 2008)*. 2008. arXiv:0808.0017 [hep-ex]. http://www-public.slac.stanford.edu/sciDoc/docMeta.aspx?slacPubNumber=slac-pub-13328.

[126] **BNL-E949** Collaboration, A. V. Artamonov *et al.*, "Study of the decay $K^+ \to \pi^+ \nu\bar{\nu}$ in the momentum region $140 < P_\pi < 199$ MeV/c," *Phys. Rev.* **D79** (2009) 092004, arXiv:0903.0030 [hep-ex].

[127] **BES** Collaboration, M. Ablikim *et al.*, "Search for the invisible decay of J / psi in psi(2S) — pi+ pi- J / psi," *Phys. Rev. Lett.* **100** (2008) 192001, arXiv:0710.0039 [hep-ex].

[128] M. S. Atiya, I.-H. Chiang, J. S. Frank, J. S. Haggerty, M. M. Ito, T. F. Kycia, K. K. Li, L. S. Littenberg, A. J. Stevens, A. Sambamurti, R. C. Strand, W. C. Louis, D. S. Akerib, D. R. Marlow, P. D. Meyers, M. A. Selen, F. C. Shoemaker, A. J. S. Smith, E. W. Blackmore, D. A. Bryman, L. Felawka, P. Kitching, A. Konaka, Y. Kuno, J. A. Macdonald, T. Numao, P. Padley, J.-M. Poutissou, R. Poutissou, J. Roy, and A. S. Turcot, "Search for the decay $\pi^0 \to \gamma +$ *X*," *Phys. Rev. Lett.* **69** (Aug, 1992) 733–736. http://link.aps.org/doi/10.1103/PhysRevLett.69.733.

[129] A. Hook, E. Izaguirre, and J. G. Wacker, "Model Independent Bounds on Kinetic Mixing," *Adv. High Energy Phys.* **2011** (2011) 859762, arXiv:1006.0973 [hep-ph].

[130] I. M. Shoemaker and L. Vecchi, "Unitarity and Monojet Bounds on Models for DAMA, CoGeNT, and CRESST-II," *Phys. Rev.* **D86** (2012) 015023, arXiv:1112.5457 [hep-ph].

[131] H. An, X. Ji, and L.-T. Wang, "Light Dark Matter and Z' Dark Force at Colliders," *JHEP* **07** (2012) 182, arXiv:1202.2894 [hep-ph].

[132] **Muon g-2** Collaboration, G. W. Bennett *et al.*, "Final Report of the Muon E821 Anomalous Magnetic Moment Measurement at BNL," *Phys. Rev.* **D73** (2006) 072003, arXiv:hep-ex/0602035 [hep-ex].

[133] M. Passera, W. J. Marciano, and A. Sirlin, "The muon g-2 discrepancy: Errors or new physics?," *AIP Conf. Proc.* **1078** (2009) 378–381, arXiv:0809.4062 [hep-ph].

[134] R. Bouchendira, P. Clade, S. Guellati-Khelifa, F. Nez, and F. Biraben, "New determination of the fine structure constant and test of the quantum electrodynamics," *Phys. Rev. Lett.* **106** (2011) 080801, arXiv:1012.3627 [physics.atom-ph].

[135] T. Aoyama, M. Hayakawa, T. Kinoshita, and M. Nio, "Tenth-Order QED Contribution to the Electron g-2 and an Improved Value of the Fine Structure Constant," *Phys. Rev. Lett.* **109** (2012) 111807, arXiv:1205.5368 [hep-ph].

[136] D. Hanneke, S. F. Hoogerheide, and G. Gabrielse, "Cavity Control of a Single-Electron Quantum Cyclotron: Measuring the Electron Magnetic Moment," *Phys. Rev.* **A83** (2011) 052122, arXiv:1009.4831 [physics.atom-ph].

[137] R. Essig, J. Mardon, and T. Volansky, "Direct Detection of Sub-GeV Dark Matter," *Phys. Rev.* **D85** (2012) 076007, arXiv:1108.5383 [hep-ph].

[138] R. Essig, A. Manalaysay, J. Mardon, P. Sorensen, and T. Volansky, "First Direct Detection Limits on sub-GeV Dark Matter from XENON10," *Phys. Rev. Lett.* **109** (2012) 021301, arXiv:1206.2644 [astro-ph.CO].

[139] A. E. Nelson and N. Tetradis, "CONSTRAINTS ON A NEW VECTOR BOSON COUPLED TO BARYONS," *Phys.Lett.* **B221** (1989) 80.

[140] S. Rajpoot, "Electroweak Interactions With Gauged Baryon and Lepton Numbers," *Phys.Rev.* **D40** (1989) 2421.

[141] R. Foot, G. C. Joshi, and H. Lew, "Gauged Baryon and Lepton Numbers," *Phys.Rev.* **D40** (1989) 2487–2489.

[142] X.-G. He and S. Rajpoot, "Anomaly Free Left-right Symmetric Models With Gauged Baryon and Lepton Numbers," *Phys.Rev.* **D41** (1990) 1636.

[143] C. D. Carone and H. Murayama, "Possible light U(1) gauge boson coupled to baryon number," *Phys.Rev.Lett.* **74** (1995) 3122–3125, arXiv:hep-ph/9411256 [hep-ph].

[144] C. D. Carone and H. Murayama, "Realistic models with a light U(1) gauge boson coupled to baryon number," *Phys.Rev.* **D52** (1995) 484–493, arXiv:hep-ph/9501220 [hep-ph].

[145] D. C. Bailey and S. Davidson, "Is there a vector boson coupling to baryon number?," *Phys.Lett.* **B348** (1995) 185–189, arXiv:hep-ph/9411355 [hep-ph].

[146] P. Fileviez Perez and M. B. Wise, "Baryon and lepton number as local gauge symmetries," *Phys.Rev.* **D82** (2010) 011901, arXiv:1002.1754 [hep-ph].

[147] M. L. Graesser, I. M. Shoemaker, and L. Vecchi, "A Dark Force for Baryons," arXiv:1107.2666 [hep-ph].

[148] P. Fileviez Perez and M. B. Wise, "Breaking Local Baryon and Lepton Number at the TeV Scale," *JHEP* **1108** (2011) 068, arXiv:1106.0343 [hep-ph].

[149] M. Duerr, P. Fileviez Perez, and M. B. Wise, "Gauge Theory for Baryon and Lepton Numbers with Leptoquarks," *Phys.Rev.Lett.* **110** (2013) 231801, arXiv:1304.0576 [hep-ph].

[150] B. A. Dobrescu and C. Frugiuele, "Hidden GeV-scale interactions of quarks," *Phys. Rev. Lett.* **113** (2014) 061801, arXiv:1404.3947 [hep-ph].

[151] S. Tulin, "New weakly-coupled forces hidden in low-energy QCD," *Phys. Rev.* **D89** no. 11, (2014) 114008, arXiv:1404.4370 [hep-ph].

[152] J. Preskill, "Gauge anomalies in an effective field theory," *Annals Phys.* **210** (1991) 323–379.

[153] R. Barbieri and T. E. O. Ericson, "Evidence Against the Existence of a Low Mass Scalar Boson from Neutron-Nucleus Scattering," *Phys. Lett.* **B57** (1975) 270–272.

[154] G. Busoni, A. De Simone, and W.-C. Huang, "On the Minimum Dark Matter Mass Testable by Neutrinos from the Sun," *JCAP* **1307** (2013) 010, arXiv:1305.1817 [hep-ph].

[155] N. Bernal, J. Martín-Albo, and S. Palomares-Ruiz, "A novel way of constraining WIMPs annihilations in the Sun: MeV neutrinos," *JCAP* **1308** (2013) 011, arXiv:1208.0834 [hep-ph].

[156] A. Gould, "Resonant Enhancements in WIMP Capture by the Earth," *Astrophys.J.* **321** (1987) 571.

[157] A. Gould, "WIMP Distribution in and Evaporation From the Sun," *Astrophys.J.* **321** (1987) 560.

[158] A. Gould, "Direct and Indirect Capture of Wimps by the Earth," *Astrophys.J.* **328** (1988) 919–939.

[159] A. Serenelli, S. Basu, J. W. Ferguson, and M. Asplund, "New Solar Composition: The Problem With Solar Models Revisited," *Astrophys.J.* **705** (2009) L123–L127, arXiv:0909.2668 [astro-ph.SR].

[160] S. Teis, W. Cassing, M. Effenberger, A. Hombach, U. Mosel, and G. Wolf, "Pion production in heavy ion collisions at SIS energies," *Z. Phys.* **A356** (1997) 421–435, arXiv:nucl-th/9609009 [nucl-th].

[161] E. Amaldi, M. Beneventano, B. Borgia, A. Capone, F. De Notaristefani, *et al.*, "INCLUSIVE ETA PRODUCTION IN P P COLLISION AT ISR ENERGIES," *Nucl.Phys.* **B158** (1979) 1–10.

[162] K. Jaeger, J. Campbell, G. Charlton, D. Swanson, C. Fu, *et al.*, "Inclusive Gamma, pi0, K0 and Lambda Production in 12.4-GeV/c p p Interactions," *Phys.Rev.* **D11** (1975) 1756.

[163] R. L. Burman and E. S. Smith, "Parameterization of Pion Production and Reaction Cross Sections at LAMPF Energies," Tech. Rep. LA-11502-MS. DE-98-011120. UC-414, Los Alamos Nat. Lab., Los Alamos, NM, 1989.

[164] **MiniBooNE Collaboration** Collaboration, A. Aguilar-Arevalo *et al.*, "The Neutrino Flux prediction at MiniBooNE," *Phys.Rev.* **D79** (2009) 072002, arXiv:0806.1449 [hep-ex].

[165] M. Bonesini, A. Marchionni, F. Pietropaolo, and T. Tabarelli de Fatis, "On Particle production for high-energy neutrino beams," *Eur. Phys. J.* **C20** (2001) 13–27, arXiv:hep-ph/0101163 [hep-ph].

[166] R. MacDonald *et al.*, "Charge Exchange of Stopped pi- in Deuterium: Experiment and Theory," *Phys. Rev. Lett.* **38** (1977) 746.

[167] D. Gorbunov, A. Makarov, and I. Timiryasov, "Decaying light particles in the SHiP experiment: Signal rate estimates for hidden photons," *Phys. Rev.* **D91** no. 3, (2015) 035027, arXiv:1411.4007 [hep-ph].

[168] J. Blümlein and J. Brunner, "New Exclusion Limits on Dark Gauge Forces from Proton Bremsstrahlung in Beam-Dump Data," *Phys. Lett.* **B731** (2014) 320–326, arXiv:1311.3870 [hep-ph].

[169] E. Fermi, "On the Theory of the impact between atoms and electrically charged particles," *Z. Phys.* **29** (1924) 315–327.

[170] E. J. Williams, "Nature of the high-energy particles of penetrating radiation and status of ionization and radiation formulae," *Phys. Rev.* **45** (1934) 729–730.

[171] C. F. von Weizsacker, "Radiation emitted in collisions of very fast electrons," *Z. Phys.* **88** (1934) 612–625.

[172] K. J. Kim and Y.-S. Tsai, "IMPROVED WEIZSACKER-WILLIAMS METHOD AND ITS APPLICATION TO LEPTON AND W BOSON PAIR PRODUCTION," *Phys. Rev.* **D8** (1973) 3109.

[173] P. M. Nadolsky, H.-L. Lai, Q.-H. Cao, J. Huston, J. Pumplin, *et al.*, "Implications of CTEQ global analysis for collider observables," *Phys. Rev. D* **78** (2008) 013004, arXiv:0802.0007 [hep-ph].

[174] H. S. Budd, A. Bodek, and J. Arrington, "Modeling quasielastic form-factors for electron and neutrino scattering," in *2nd International Workshop on Neutrino-Nucleus Interactions in the Few GeV Region (NuInt 02) Irvine, California, December 12-15, 2002*. 2003. arXiv:hep-ex/0308005 [hep-ex].

[175] T. Leitner, "Neutrino interactions with nucleons and nuclei," Master's thesis, Institut fur Theoretische Physik Justus-Liebig-Universitat Gießen, September, 2005.

[176] G. Duda, A. Kemper, and P. Gondolo, "Model Independent Form Factors for Spin Independent Neutralino-Nucleon Scattering from Elastic Electron Scattering Data," *JCAP* **0704** (2007) 012, arXiv:hep-ph/0608035 [hep-ph].

[177] W. Rarita and J. Schwinger, "On a theory of particles with half integral spin," *Phys. Rev.* **60** (1941) 61.

[178] H. F. Jones and M. D. Scadron, "Multipole gamma N Delta form-factors and resonant photoproduction and electroproduction," *Annals Phys.* **81** (1973) 1–14.

[179] G. Ramalho, M. T. Pena, and F. Gross, "A Covariant model for the nucleon and the Delta," *Eur. Phys. J.* **A36** (2008) 329–348, arXiv:0803.3034 [hep-ph].

[180] F. Gross, G. Ramalho, and M. T. Pena, "A Pure S-wave covariant model for the nucleon," *Phys. Rev.* **C77** (2008) 015202, arXiv:nucl-th/0606029 [nucl-th].

[181] G. Ramalho, M. T. Pena, J. Weil, H. van Hees, and U. Mosel, "Role of the pion electromagnetic form factor in the $\Delta(1232) \to \gamma^* N$ timelike transition," *Phys. Rev.* **D93** no. 3, (2016) 033004, arXiv:1512.03764 [hep-ph].

[182] M. I. Krivoruchenko and A. Faessler, "Comment on delta radiative and Dalitz decays," *Phys. Rev.* **D65** (2002) 017502, arXiv:nucl-th/0104045 [nucl-th].

[183] T. M. Aliev and A. Ozpineci, "Radiative decays of decuplet to octet baryons in light cone QCD," *Nucl. Phys.* **B732** (2006) 291–320, arXiv:hep-ph/0406331 [hep-ph].

[184] S. K. Karlheinz Langanke, J.A. Maruhn, ed., *Computational Nuclear Physics 2*. Springer-Verlag New York, 1993.

[185] **MiniBooNE** Collaboration, A. A. Aguilar-Arevalo *et al.*, "The Neutrino Flux prediction at MiniBooNE," *Phys. Rev.* **D79** (2009) 072002, arXiv:0806.1449 [hep-ex].

[186] G. Casella, C. P. Robert, and M. T. Wells, *Generalized Accept-Reject sampling schemes*, vol. Volume 45 of *Lecture Notes–Monograph Series*, pp. 342–347. Institute of Mathematical Statistics, Beachwood, Ohio, USA, 2004. http://dx.doi.org/10.1214/lnms/1196285403.

[187] W. H. Press, B. P. Flannery, S. A. Teukolsky, and W. T. Vetterling, *Numerical Recipes in FORTRAN 77: The Art of Scientific Computing*. Cambridge University Press, 2 ed., Sept., 1992. http://www.worldcat.org/isbn/052143064X.

[188] D. H. Bailey, J. M. Borwein, D. Broadhurst, and W. Zudilin, "Experimental Mathematics and Mathematical Physics," *Contemp. Math.* **517** (2010) 41–58, arXiv:1005.0414 [math-ph].

[189] G. Engeln-Müllges and F. Uhlig, *Numerical Algorithms with C*. Springer-Verlag New York, Inc., New York, NY, USA, 1996.

[190] **LSND** Collaboration, C. Athanassopoulos *et al.*, "The Liquid scintillator neutrino detector and LAMPF neutrino source," *Nucl. Instrum. Meth.* **A388** (1997) 149–172, arXiv:nucl-ex/9605002 [nucl-ex].

[191] **LSND** Collaboration, A. Aguilar-Arevalo *et al.*, "Evidence for neutrino oscillations from the observation of anti-neutrino(electron) appearance in a anti-neutrino(muon) beam," *Phys. Rev.* **D64** (2001) 112007, arXiv:hep-ex/0104049 [hep-ex].

[192] **MiniBooNE** Collaboration, A. A. Aguilar-Arevalo *et al.*, "Improved Search for $\bar{\nu}_\mu \to \bar{\nu}_e$ Oscillations in the MiniBooNE Experiment," *Phys. Rev. Lett.* **110** (2013) 161801, arXiv:1207.4809 [hep-ex].

[193] **MiniBooNE** Collaboration, A. A. Aguilar-Arevalo *et al.*, "Measurement of the Antineutrino Neutral-Current Elastic Differential Cross Section," *Phys. Rev.* **D91** no. 1, (2015) 012004, arXiv:1309.7257 [hep-ex].

[194] **Super-Kamiokande** Collaboration, Y. Fukuda *et al.*, "The Super-Kamiokande detector," *Nucl. Instrum. Meth.* **A501** (2003) 418–462.

[195] **T2K** Collaboration, T. Le, "Overview of the T2K long baseline neutrino oscillation experiment," in *Particles and fields. Proceedings, Meeting of the Division of the American Physical Society, DPF 2009, Detroit, USA, July 26-31, 2009*. 2009. arXiv:0910.4211 [hep-ex]. https://inspirehep.net/record/834842/files/arXiv:0910.4211.pdf.

[196] S. Assylbekov *et al.*, "The T2K ND280 Off-Axis Pi-Zero Detector," *Nucl. Instrum. Meth.* **A686** (2012) 48–63, arXiv:1111.5030 [physics.ins-det].

[197] **CSI** Collaboration, D. Akimov *et al.*, "Coherent Scattering Investigations at the Spallation Neutron Source: a Snowmass White Paper," in *Community Summer Study 2013: Snowmass on the Mississippi (CSS2013) Minneapolis, MN, USA, July 29-August 6, 2013*. 2013. arXiv:1310.0125 [hep-ex]. https://inspirehep.net/record/1256325/files/arXiv:1310.0125.pdf.

[198] **SHiP** Collaboration, M. Anelli *et al.*, "A facility to Search for Hidden Particles (SHiP) at the CERN SPS," arXiv:1504.04956 [physics.ins-det].